CONTENTS

LIST OF FIGURES

LIST OF TABLES

CHAPTER ONE

GENERAL INTRODUCTION

1.1 Properties of diamond

Diamond is one of the few materials that are supreme in two very different ways. It is the most beautiful of all gems stones and the most powerful of all cutting materials due to its extreme hardness. Diamond has the greatest resistance to plastic flow of any material. Its exceptional yield strength arises essentially from two considerations. The first is that the theoretical strength is high owing to the high density of strong atomic bonds. The second is due to the strongly directional nature of the bonding that allows only the presence of narrow dislocations that are difficult to move (Field, 1994).

The gem qualities of diamond are due to its high refractive index (2.417 at 589 nm) and high dispersive power. A high refractive index leads to a low angle of total internal reflection (only 24^{o}) so that light is internally reflected many times in a cut gem, giving it the well known dazzling brilliance. Diamond's high dispersive power causes light to be dispersed into its component colours and hence give rise to the quality called fire. Other minerals such as zircon, topaz, and rutile also show remarkable brilliance but can easily be scratched hence failing as industrial stones (Berman, 1965).

Ancient records abound attesting to the hardness of diamond and are documented in the Bible; similar information is also found in records of ancient blacksmiths. Modern uses that exploit the extreme hardness of diamond include attachment of fine powder to cutting tools using special binders.

Diamond is chemically inert and has a very high thermal conductivity of 25 $W.cm^{-1}.K^{-1}$ which is five times that of copper at 300 K. Consequently, diamond is in much demand in the electronics industry where it is used as heat sinks. CVD (Chemical Vapour Deposited) diamond is now produced fast and cheaply. It enables the exploitation of e other unique properties of diamond including optical transparency, resistance to corrosion, large

bandgap, high electron and hole mobility. CVD diamond is also used as detectors in high radiation zones where silicon would quickly disintegrate.

1.2 Crystal structure

Each carbon atom in the diamond lattice is surrounded by four atoms that occupy the apices of a tetrahedron. They are all connected to one another by sp^3 covalent bonds. The cubic diamond structure may be described by a face centred cubic (fcc) point lattice in which each lattice point corresponds to two atoms, one located at $(0,0,0)$ and another at $(\frac{1}{4},\frac{1}{4},\frac{1}{4})$. The lattice parameter a (the edge of the fcc lattice) is $0.3561\,\text{nm}$. The lattice structure is shown in Figure 1.1

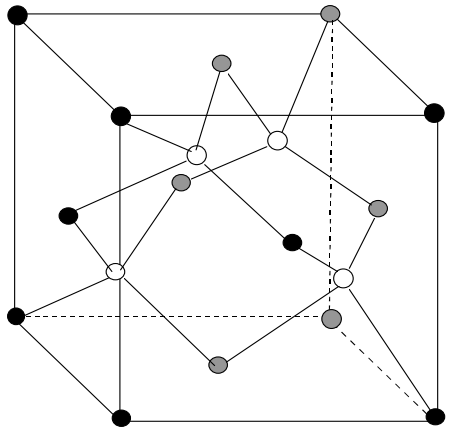

Figure 1.1: Diamond structure. The sites corresponding to one of the two interpenetrating face-centred cubic lattices are unshaded. The four nearest neighbours of each point form the vertices of a regular tetrahedron**.**

Diamond crystallizes in either octahedra with faces being (111) planes, dodecahedra with faces being (110) planes or, occasionally, in simple cubes with (100) faces. The shear strength of diamond depends on the number of covalent bonds that must be broken during shear. This number is smallest along (111) planes. For this reason diamonds can be cleaved along (111) planes and this is used in dividing large stones and in shaping

processes. The hardness also varies greatly with direction and must be taken into account when mounting cutting tools.

1.3 Classification of diamonds

The colour of native diamonds is determined mainly by mineral inclusions, plastic deformation, defects formed during irradiation and subsequent heating of the diamond and substitutional impurities. In most cases the price of the diamond is affected adversely by the presence of the defects. Nitrogen, present in more than $90\,\%$ of all diamonds, is spectroscopically by far the most important substitutional impurity; it may be present in concentrations of up to 500 atomic parts per million (ppm). Boron is the dominant impurity in a much smaller fraction of diamonds. Although many other impurity elements can be detected by nuclear techniques, only a few other than nitrogen and boron appear to be spectroscopically important. Even in the best natural diamonds a few parts per million (ppm) of impurities may be present.

In most diamonds only a small fraction of the nitrogen is present at single isolated substitutional sites (P1 centres). Most of the nitrogen is present in small clusters, consisting of two (A centres), three (P2 centres) or four (B centres) substitutional atoms. Simplistic models for these nitrogen centres are given in Figure 1.2. In all diamonds absorption due to two phonon processes is observed at infrared energies between about 0.2 and 0.6 eV. Single photon absorptions due to nitrogen and other impurities are observed at energies below 0.2 eV. A perfect diamond will not absorb visible or ultraviolet radiation of frequency ν unless it has energy of amount $h\nu = 5.5$ eV, the band gap energy for diamond, where h is Planck's constant.

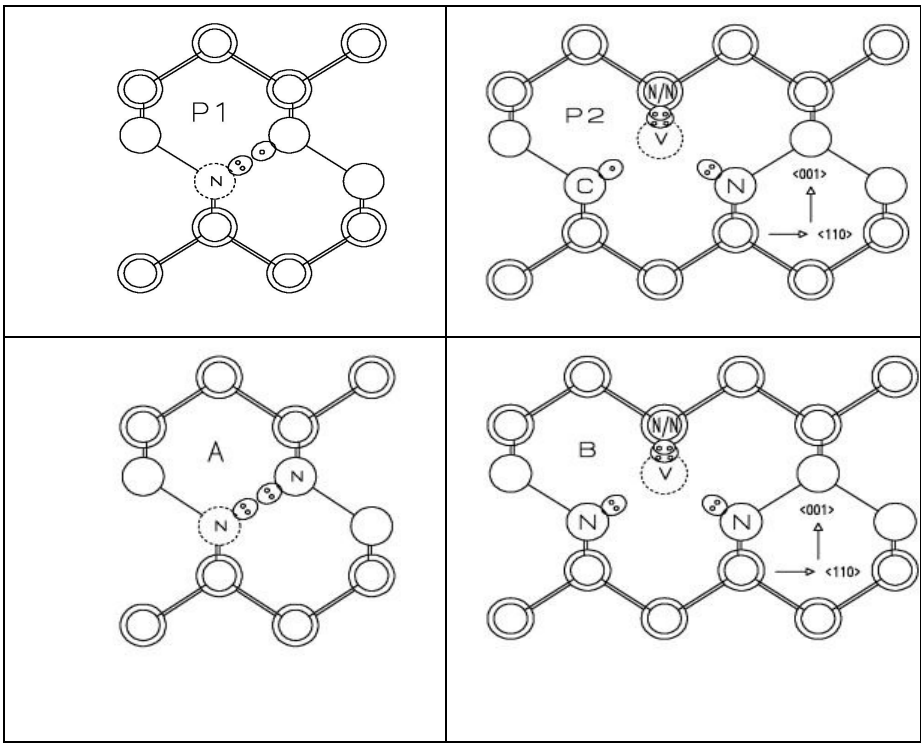

Figure 1.2: Projection of the models for the P1, P2, A and B centres on a (110) plane. The P1 centre has two electros in one of its bonds with carbon. The P2 centre consists of a vacancy surrounded by 3 atoms of N and one of carbon. The A centre consists of 2 nearest neighbour N atoms whereas the B centre has 4 N atoms surrounding a vacancy.

Diamond has been classified as type I or type II using Infrared (IR) spectroscopic methods at energies below 0.2 eV and UV-visible energies below 5.5 eV $(220$ nm$)$. Diamonds of type II transmit well in the UV at wavelengths down to the absorption edge at 220 nm whereas those of type I show absorption starting at 330 nm and increasing fairly rapidly at short wavelengths.

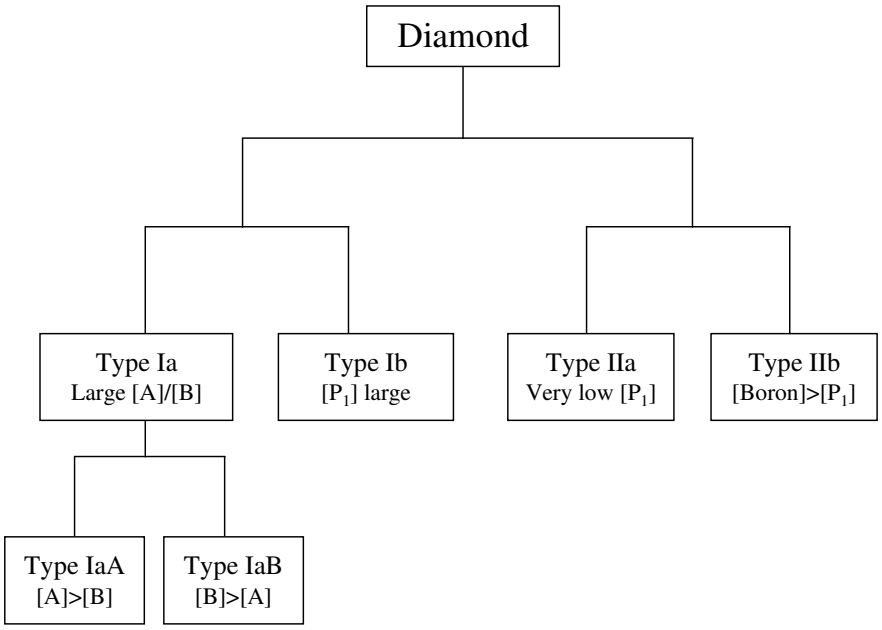

Figure 1.3: Block diagram of diamond types. The A centres are aggregates that consist of two nearest neighbour nitrogen atoms whereas B centres consist of nitrogen atoms and a vacancy. The symbols [A], [B], etc denote concentrations of A, B, etc centres, respectively**.**

Type II diamonds are nearly perfect crystals in that they have practically no impurities or defects. However, in many stones of this type, there is a weak continuous absorption that is probably due to minute amounts of graphite or amorphous carbon. A small proportion of type II diamonds are semiconducting and are classified as type IIb with resistivity in the region of 1×10^{2} Ω.cm in sharp contrast to the insulating type IIa with a typical value of 5×10^{14} Ω.cm (Custers, 1955). It was found that type IIb diamonds contain mostly boron acceptor centres with energy of about 0.35 eV above the valence band.

The classification may be given in terms of the nitrogen content as indicated in Figure 1.3. Type I diamond contains significant amounts of nitrogen while type II diamonds are almost nitrogen free. Type I may be further subdivided to reflect aggregated and isolated nitrogen giving type Ia and type Ib, respectively. The most common form of aggregates in Ia diamond are the A centres (2 nearest neighbour N atoms) and B centres (4 N atoms surrounding a vacancy).

Strong absorption with lines appearing in the visible region and a continuous absorption starting at 1.7 eV is found in type I diamonds. The absorption is mainly due to nitrogen impurities. The clarity and colour of diamond is controlled by defects and impurities. Inclusions in diamond act as sinks for the light within the crystal leading to diminished transparency and brilliance.

The energy band picture of an insulator shows that impurity levels may occur at all points in the forbidden energy gap. However, depending on the position of the Fermi energy level, only certain traps will contain any charge (Townsend and Kelly, 1973).

For a long time, defect studies emphasized optical rather than electrical properties; consequently, the theoretical studies have been concerned with excited states in diamond to a larger extent than in other semiconductor work (Berman, 1965). The low concentrations of defects are a major limiting factor in such studies making it necessary to use highly sensitive methods.

1.4 Growth of synthetic diamond

Diamond may be synthesised at high pressure in the region of the carbon phase diagram where the diamond is stable and at low pressure in the region of the diagram where the graphite stable using various techniques (Burns and Davies, 1992). Of the 100 tonnes of diamond now produced annually, around 80% is manufactured by the high pressure, high temperature method. The high-pressure techniques may be classified into static pressure generation methods and the dynamic shock wave methods.

The synthesis is accomplished using either of two paths: carbon to diamond or by reconstitution of diamond powders to obtain large diamond crystals. Fine diamond can be produced by subjecting organic compounds such as anthracene, camphene, fluorene and paraffin wax to pressures in the range of 9.5-15 GPa and temperatures of 1300-3000 °C for $0.2-0.5$ minutes (Wentorf, 1965). The direct conversion methods, however, produce extremely fine polycrystalline aggregates of usually high defective diamond.

It has been shown that non-metallic compounds: sodium sulphate, magnesium sulphate, magnesium hydroxide and calcium hydroxide can act as catalysts for diamond synthesis from graphite under an estimated pressure of 7.7 GPa and a temperature of 2150 °C (Burns and Davies, 1992).

Effective solvent/catalysts for diamond synthesis from carbons are molten metals from group VIII of the periodic table. Others include manganese, chromium, tantalum and niobium. Further, alloys of the transition metals are normally used for the production of diamond because of the generally lower melting points of alloys and therefore the generally lower pressures required. Major companies that produce commercial synthetic diamond usually favour binary combinations such as iron-nickel (General Electric), manganese-nickel (companies of the former USSR), and cobalt-iron (De Beers). Other impurities include nitrogen or other lattice defects.

The synthesis of diamond using the carbon-to-diamond methods enables the production of diamonds of approximately 1mm in size. To grow large diamonds, the reconstitution technique is used. Here, diamond is used as a source of carbon. The driving force for reconstitution under diamond stable conditions is provided by the higher solubility of diamond in a hot zone of the solvent/catalyst and the subsequent crystallization of diamond in a cooler zone (Burns and Davies, 1992).

Synthetic diamond has all the desirable mechanical properties of diamond making it very suitable for industrial applications. However, the optical properties are quite different from those of the majority of natural diamonds.

1.5 Morphology of synthetic diamond

There are major differences between the morphology of natural diamond and synthetic diamond. The morphology and growth zone patterns determine the crystal shapes; they provide major clues to the thermodynamic and chemical conditions and the changes these variables experienced during the growth of diamond. For instance, it has been reported (Kanda *et al.,* 1989) that synthetic diamonds grown in pure nickel have habit and that $\{110\}$ and $\{113\}$ faces occur when nickel alloys, cobalt and iron are used.

The appearance of these faces is associated with the affinity of the metal solvent/catalyst with nitrogen.

1.6 The scope of this thesis

The main goal of this thesis is to report on the Electron Paramagnetic Resonance (EPR) studies on paramagnetic irradiation damage centres in synthetic type Ib diamonds. Most of the measurements were made on a neutron-irradiated diamond whereas some were made on three electron-irradiated stones.

The thesis is presented in 12 chapters as follows:

- In chapter 1 the general background theory to the diamond crystalline material including classification and synthesis is presented.
- A brief outline of the theory of both electron and neutron irradiation will be presented in chapter 2.
- The theory of EPR as used in the study of defects in diamond is given in chapter 3. It will be shown that the magnetic field at which an EPR transition is observed is determined by a parameter known as the g-value. For a free electron, and most centres in diamond, g is close to 2. The central region of the EPR spectrum is therefore often referred to as the $g = 2$ region.
- Experimental methods used to obtain the results reported in this thesis form the subject of chapter 4.
- An introductory overview of defects relevant to this thesis will be given in chapter 5.
- In chapter 6, the annealing curves obtained in this work will be presented. Subsequently, discussions of the annealing behaviour for selected centres will be made in the relevant chapters.
- The most prominent part of the EPR spectra is contained in a single line, referred to as the a-line, in the central region. Attempts will be made to analyse the structure of this line and the sources which contribute to it in chapter 7.
- A few EPR centres involving nitrogen and a vacancy will be analysed and discussed in chapter 8.

- A brief review as well as some new work on four previously studied centres (W11, W12, W13 and W14), which are observed only in irradiated type Ib diamonds, will be presented in chapter 9.
- W29 is an EPR centre that becomes observable in irradiated type Ib diamond after annealing at temperatures above about 400 ^{o}C. It intensity gradually increases and peaks at about 700 ^{o}C and then anneals out at about 850 ^{o}C. Work on this centre will be presented in chapter 10 where it will be shown to have many similarities with R4/W6, the neutral divacancy centre in diamond.
- Results on measurements of relaxation times for R4/W6 and W29 centres in neutron-irradiated type Ib diamond are presented in chapter 11.
- In chapter 12 a conclusion and a summary of important results is presented. This is then followed by the references.

CHAPTER TWO

RADIATION DAMAGE AND ANNEALING

2.1 Introduction

Diamond physics has been spurred recently by the advent of Chemical Vapour Deposition (CVD) diamond which is used, for example, in radiation detection under harsh conditions. For such detection, a full understanding of radiation process is required. Detectors are known to benefit from priming action which involves either the creation of damage centres or the ionisation of existing centres (Davies *et al.*., 2001). The way forward requires a quantitative knowledge of the production and evolution of damage centres. Hence the importance of radiation damage in diamond.

High energy radiation utilized in the irradiation of materials may be classified into four groups: photons, light-charged particles, heavy atoms or ions and neutrons. The interaction of high energy photons with matter may lead to photo-electric absorption, Compton scattering or pair-production. High energy electrons usually cause primary displacements (single displaced atoms), whereas fast neutrons have large amounts of energy such that a displacement atom, in the interstitial position, is likely to be well separated from the vacancy from which it originated.

The collision between charged irradiation particles such as electrons and the lattice atoms can be represented by a Coulomb potential (Rutherford scattering) whereas the interaction between the atoms and neutral particles such as neutrons can be described using hard-sphere collision model (Bourgoin and Lannoo, 1983).

In this thesis, the only relevant irradiation particles are electrons and neutrons; they are discussed in the next two sections. More work was recorded using neutron-irradiated diamond and so a relatively longer discussion will be made on irradiation with neutrons. Only a brief introduction to electron irradiation will be covered.

2.2 Electron irradiation

Fast electrons with energy in the range of 1 MeV are able to displace atoms from crystal sites if the collisions are near head-on and if E_d, the threshold energy for displacement is of the order of 25 eV. The use of relativistic mechanics for electrons with energies near 1 MeV is necessary as $m_e c^2 = 0.511\,\text{MeV}$ where m_e is the electron rest mass and c the speed of light in vacuum. A detailed discussion of irradiation with fast electrons and the similarity of their effects with those of massive particles have been made by Seitz and Koehler (1956).

An electron passing through a region of neutral atoms interacts mainly by means of the coulomb forces with the electrons in the atoms. Though in each encounter the electron loses on the average not more than a few electron volts of its kinetic energy, ionization and excitation of atoms gives the greatest energy loss per unit path length of the particle. The electron loses only a tiny fraction of its energy through displacement collisions. Losses in energy would be much higher if the electron interacts with the nucleus; however, such collisions are extremely rare and hence do no contribute appreciably to the overall energy loss (Meyerhof, 1967; Kelly, 1966; Dienes and Vineyard, 1957; Iwata and Nihira, 1971). Another important loss of electron energy is due to bremsstrahlung radiation.

Nuclear masses are large in comparison with the electron masses and therefore the collision essentially changes only the electron momentum. If the electron is deflected through an angle θ in the centre of mass system by interaction with the nucleus of the target atom, the energy T transferred to the nucleus is (Seitz and Koehler, 1956)

$$T = T_m \sin^2 \frac{\theta}{2} \tag{2.1}$$

where T_m is the maximum possible energy which could be transferred to the nucleus by an electron of energy E.

To calculate the number of atoms displaced by the electron of energy E as given above, the scattering cross section of the nucleus for electron is required. The electron-nucleus interaction is through the Coulomb potential and the atom electrons are neglected when electron energies are large. Mckinley and Feshbach (1948) have given the differential cross section for Rutherford scattering of relativistic electrons as

$$d\sigma(\theta) = \left(1 - \beta^2\right)\left[1 - \beta^2 \sin^2\frac{\theta}{2} + \pi\alpha\beta \sin\frac{\theta}{2}\left(1 - \sin\frac{\theta}{2}\right)\right] \times \frac{\pi b 2}{4}\cos\frac{\theta}{2}.\mathrm{cosec}^3\frac{\theta}{2}.d\theta \quad (2.2)$$

where $\alpha=Z/137$, $\beta=v/c$ and $b=2Ze^2/m_e v^2$. Z is the atomic number of the target whereas v is the speed of the electron.

The determination of total cross sections enables the calculation of the number of displaced atoms.

2.3 Neutron irradiation

2.3.1 Sources of neutrons

Important categories of neutron sources for irradiation of solids include the nuclear reactor, particle accelerators and spallation sources. Of these, the reactor produces continuous fluxes of neutrons while the last yields only pulse fluxes which can be used to obtain neutron intensity that is 50 to 100 times higher than the best continuous source.

In a nuclear reactor very high fluxes of thermal neutrons are available, often of the order of 10^{12} to 10^{14} $n.cm^{-2}s^{-1}$ (I.A.E.A, 1966; Watterson, 1975). These fluxes are four to seven orders of magnitude higher than those obtained with accelerator or isotopic sources. The neutron flux is produced by the moderation of fission spectrum neutrons; these are mainly degraded by elastic collisions with the moderator to give a complex neutron spectrum.

Different neutron energies occurring in a reactor are usually classified in three groups with increasing energies as thermal, epithermal and fast. Thermal neutrons are those that have reached a thermal equilibrium with the ambient medium as a result of being slowed down by a moderator. Most of these neutrons have energies lower than 1 eV. The fast neutrons can be considered as those with energies larger than 100 keV whereas epithermal neutrons have energy between 1 eV and 100 keV.

Spallation is a nuclear reaction that takes place when a fast particle, such as a high-energy proton, bombards a heavy atomic nucleus; some neutrons are "spalled," or knocked out.

Other neutrons are "boiled off" as the bombarded nucleus heats up. For every proton striking the nucleus, 20 to 30 neutrons are expelled (SNS Website, 2004).

2.3.2 Neutron interactions with matter

Neutron scattering mechanisms

Due to charge neutrality, the interaction of fast neutrons with an atom is simpler than the interaction between an ion and an atom. The neutron thus interacts essentially with the nucleus only without influencing the atomic electrons (Walt and Barschall, 1954). This may lead to either elastic collision or nuclear reactions whose end products may have sufficient energy to cause further atomic displacements.

The fact that neutron-electron interactions are unimportant may be understood as follows. The coulomb interaction in this case is close to the ionization potential of the atoms - being about 10 eV at a distance r of 10^{-11} cm. However, the effective cross section for such collisions is very small in comparison with ionizing collision of charged particles. The result is that ionizing collisions with atoms are relatively unimportant for the description of the interactions of neutrons with matter. Instead, the interaction of neutrons with atomic nuclei is considerably stronger since it is determined by nuclear forces which are not of electromagnetic origin (Budylin and Vorobev, 1964).

Neutrons used for irradiation interact with atomic nuclei through several mechanisms such as elastic scattering, inelastic scattering, non-elastic scattering, neutron capture and spallation. However the last mechanism is definitely unimportant in most cases as neutron energies of order of 100 MeV are required; these are outside the scope of nuclear reactors used for irradiation.

Elastic scattering is the most important process for irradiation damage. The total kinetic energy is conserved so that the energy lost by the neutron is transferred to the recoiling nucleus. The cross section for this scattering depends on the neutron energy and the target nuclei. In the case of the inelastic scattering, the neutron is absorbed and then re-emitted. The nucleus absorbs some energy internally and is left in an excited state. On de-excitation, a gamma ray is emitted and the nucleus recoils.

Nonelastic scattering of neutrons differs from the inelastic scattering in that it leads to another kind of secondary particle, such as the alpha particle, being emitted. At low neutron energies the mechanism leads to the capture and disappearance of the neutron. This is termed the neutron capture.

Interaction cross sections

The probability of interaction between a neutron and a nucleus is measured numerically by the microscopic cross section σ which can be considered as the effective area of the target presented to the neutron by the nucleus. The macroscopic cross section, Σ, is equal to $N\sigma$ where N is the number of nuclei in 1 cm^3 of material. Each of the processes of interaction between a neutron and a material will be characterised by a particular cross section. The various cross sections will be different for different nuclei and will also be functions of the speed or energy of the neutron. The inverse of the microscopic cross-section, $\lambda=1/\sigma$ called the neutron mean free path, indicates the distance the neutron moves between two events of a particular process in a given material (Motte and Debrue, 1963).

Many nuclei present a sudden increase in the absorption cross section for neutrons with low energies i.e. slow neutrons. This is termed resonance capture and is usually followed by gamma ray emission due to transition from one compound nucleus energy level to another. The target atom subsequently recoils to give rise to lattice damage.

However, the cross section for thermal neutrons for carbon (^{12}C) is very small being only 0.0035 barns (SNS Website, 2004). Consequently, it is unlikely that slow or thermal neutrons would be important in our case. Hence, we shall not involve neutron capture any further in our discussions of neutron irradiation damage.

2.3.3 The knock-on atoms and the cascade process

The secondary displacements due to moving knock-on atoms colliding with the stationary lattice may be discussed by neglecting the screening effect of the atomic electrons. Such encounters usually involve small interaction distances. This is because a knock-on atom

colliding with a stationary atom will be deflected from its original course by an amount depending on its energy and its distance of approach or impact parameter. Deflections are greater for smaller projectile energies and closer approaches. Whenever the nuclei of the two atoms approach to a distance much less than the screening radius, the nuclear Coulomb repulsion produces most of the deflection and the collision can be calculated by ignoring the screening altogether (Dienes and Vineyard, 1957). In this case the Rutherford scattering is applicable.

The total number of primary displacements produced by one electron is given by

$$n_p = \phi t n_0 \sigma_d \tag{2.3}$$

where ϕ is the number of bombarding particles traversing unit area per unit time within the specimen, t is the duration of the bombardment, $n_{0,}$ is the number of atoms per unit volume of the specimen, and σ_d is the cross section per atom for collisions which produce displacements. About 100 displaced carbon atoms result from each primary collision (Keating, 1963). Consequently, there is an extensive damage in the crystal and a production of a large concentration of spins.

The cascade process induced by the primary knock-ons may be discussed using many different models (Dienes and Vineyard, 1957). The main assumptions are the following. Firstly, all collisions will be assumed to be binary; that is, the moving atoms always will be assumed to interact with one target atom at a time. Secondly, all collisions take place between a moving atom and a stationary lattice atom. Thirdly, all the atoms are assumed to be randomly located and hence overlooking the regular lattice arrangement.

The model of Kinchin and Pease (1955) which is usually favoured due to simpler mathematics makes the following additional specific assumptions. Firstly, the main cause of energy loss for a knock-on atom with a large energy is by interaction with electrons and subsequent ionization. Secondly, all the knock-ons with energies below this limiting energy lose their energy only by elastic hard-sphere-like collisions, i.e. interatomic collisions with the target atom. Thirdly, an atom will invariably be displaced from its lattice site if by collision it receives energy greater than the threshold energy E_d. Finally, the

striking atom will remain behind at the collision site if the struck atom receives energy greater than E_d and the incoming atom is left with energy less than E_d. The result is that there is a net increase in the number of displaced atoms if both atoms have kinetic energies greater than E_d. This is so if atoms are assumed to be alike, that is, for a monatomic substance.

Irradiation neutron fluxes with energies of up to about 15 MeV are able to cause atomic displacements. In this range elastic scattering is the most important mechanism and may be considered using classical mechanics with a neutron and the target nucleus as hard spheres in the centre of mass coordinate system. Such scattering can be taken as isotropic or S wave scattering (Leibfried, 1963; Kelly, 1966; Dienes and Vineyard, 1957). However, deviations occur and the energy given to a nucleus is less than expected on the basis of pure elastic scattering.

In pure elastic scattering, the maximum energy T_m transferred by a neutron of energy E to a nucleus of atomic weight A is given by (Dienes and Vineyard, 1957)

$$T_m = 4AE/(A+1)^2 = \alpha E \tag{2.4}$$

where $\alpha=4A/(A+1)^2$.

In the case of isotropic scattering, the struck nucleus has an equal probability of receiving energy between $T=0$ and $T=T_m$. The average energy transferred is then $T_m/2$.

The number of collisions C occurring in unit time between mono-energetic neutrons of energy E and having a flux of ϕ and nucleus of atomic weight A is given by

$$C = N_0 \phi \sigma (E) \tag{2.5}$$

where N_0 is the number atoms per unit volume and $\sigma(E)$ is the atomic cross section for elastic scattering of the neutron.

Therefore if a mono-energetic neutron beam of energy E has a flux ϕ, the number of displacements produced in unit time and unit volume is given by

$$\frac{\mathrm{d}n}{\mathrm{d}t} = N_0 \phi \sigma (E) \overline{\eta}(E) \tag{2.6}$$

where $\overline{\eta}$ is the average number of displacements per collision. Kinchin and Pease (1955) have determined $\eta(T)$, as a function of energy T for various energies of the bombarding neutron.

2.4 Radiation damage in diamond

Diamonds are coloured green by neutron irradiation, blue-green by γ-rays from a ^{60}Co source and blue by electrons of energy in the range of 0.5 to 1.0 MeV. However, X-rays produce no colour changes. Clark *et al.* (1955) found that there was a similarity of absorption lines induced by various forms of radiation. They also observed that X-rays failed to produce the lines; ordinary optical bleaching of the lines had not been detected. Consequently, they concluded that the induced absorption was produced by electronic transitions in carbon atoms ejected from their normal sites, or in the atoms surrounding the vacant site.

The rate of production of optical absorption bands and the rate of increase in electrical resistivity in type IIb diamonds due to electron irradiation with energies in the range 0.3 to 2.0 MeV were first investigated by Clark *et al.* (1961). They assumed isotropic displacement energy $E_d = 80$ eV and obtained results that fitted theoretical predictions in the range 0.3 to 1.0 MeV (Glendenin, 1948). Other researchers that have carried out similar diamond studies include Bibby and Duncan (1975); they utilized the data for the cross sections for silicon collected by Fisher and Banbury (1970) which they scaled appropriately. They also studied the production of the GR1 band and the background absorption at 2.696 eV and obtained the best fit for minimum displacement energy of 60 eV. They showed that the GR1 fitted the single vacancy curve whereas the 2.696 eV absorption line fitted the divacancy production rate curve. Lea-Wilson (1988) adapted the model to explain his experimental results for electron-irradiated diamond. He estimated that each 2 MeV electron will have a range of about 1.5 mm and will create on average 0.06 vacancies and 0.004 divacancies in a diamond of thickness 0.5 mm or more. However, earlier studies by Clark *et al.* (1955) suggested that for 1 MeV electrons, 0.1 and 0.05 displacements were produced assuming E_d of 40 and 60 eV, respectively. The number of secondary defects produced was a small fraction of the number of primary defects (<10%).

Bourgoin and Massarani (1976) determined defect introduction rate from conductivity measurements at about 12 K on boron-doped diamonds that were electron-irradiated at 15 K. They deduced a threshold energy for atomic displacement of T_d =35±5 eV.

Relatively recent studies of irradiation in diamond have been reviewed (Davies, 1994) following mounting technological interest that has been stimulated by the advent of Chemical Vapour Deposition (CVD) diamond. There is presently more need for improved understanding of defects and impurities in diamond.

2.5 Annealing

2.5.1 Isochronal and isothermal annealing

Defects that are present in a solid at concentrations in excess of the thermal equilibrium level tend to react to reduce the free energy of the solid. Controlled annealing of defects therefore forms an important tool for studying radiation damage. Low temperature irradiation has shown that some defects are mobile at very low temperatures pointing to partial annealing is taking place during irradiation (Dienes and Vineyard, 1957).

Table 2.1: Fate of the irradiation damage defects

Process	Example
Annihilation	Vacancies and interstitials annihilate each other by combining.
Absorption	Absorption of vacancies and interstitials at surfaces, grain boundaries or dislocations
Trapping	Trapping of vacancies and interstitials by substitutional impurities due to local stress fields
Replacement	An interstitial replaces a substitutional impurity atom that in turn becomes an interstitial.
Aggregation	Uniting of vacancies with vacancies and interstitials with interstitials.

The change of a given property of a solid with defects is a function of time and occurs more rapidly at higher temperatures. If the temperature is raised sufficiently enough, all trace of the property due to defects disappears. Here the annealing can be viewed as

describing the processes of defect decay induced by temperature. Equations similar to those for chemical kinetics are used to describe the processes (Kelly, 1966). The defect is assumed to require some energy E in order to undergo some reaction that modifies its contribution to the measured property like optical absorption, electrical conductivity etc. The fraction of the defects that have this energy is given by the Boltzmann factor $\exp(-E/kT)$. According to Kelly (1966), the annealing rate of a property *P*, say concentration, is described by

$$dP(t)/dt = -AP(t)^{\gamma} \exp\left[-E/kT\right] \tag{2.7}$$

where $P(t)$ is the property remaining after time t at absolute temperature T, k is Boltzmann's constant, γ is a constant called the order of reaction whereas A is a constant which is a frequency factor for the case of $\gamma = 1$. E is the activation energy for the process.

Disappearance of the excess defects occurs in a number of ways. The defects become mobile and then migrate to sinks, recombine with their counterpart or form new defects by association between themselves or with other types of defects or impurities. They may dissociate if they are complexes. Each of these processes: migration, recombination, complex formation and dissociation is characterized by an activation energy.

Isochronal annealing procedure may be carried out in the following way. The temperature of the crystal is raised from some reference temperature to T_0 for an anneal step where it is held constant for a fixed time Δt. Following this, the crystal is cooled down to the reference temperature at which the measurement of a property proportional to the concentration of defects is made. A series of such Δt-steps at successively higher temperatures constitutes an isochronal anneal. In isothermal annealing, the sample is heated at the same fixed temperature but for different increasing time intervals at a time before cooling and making measurements.

Precautionary measures are needed when annealing diamond. When it is heated in pure oxygen or air (which comprises 20.8 % oxygen and 78.1% nitrogen) to about 700 ^{o}C or higher it will graphitize or oxidize wholly or partially to CO or CO_2. However, diamond

can be heated to temperatures up of 1500 ^{o}C provided this is done in the absence of O_2, and preferably in vacuum.

Isochronal annealing was used to study defects reported in this thesis as discussed in later chapters.

2.5.2 Annealing of defects through diffusion

Vacancy diffusion

One way in which annealing proceeds is through diffusion. Any atom in the lattice next to a vacancy is separated from the vacancy by a potential barrier, due to bonding to its neighbours. It must overcome this barrier, say E_m, in order to jump into the vacancy (Fletcher and Brown, 1953). The average time for it to make such a jump due to thermal excitation is given by (Mott and Gurney, 1940).

$$\tau = \nu_0^{-1} e^{E/kT} \tag{2.8}$$

where ν_0 is the average lattice frequency $\approx 10^{13}$ Hz, T is the absolute temperature and k is Boltzmann's constant. When an atom jumps into a neighbouring vacancy, another vacancy takes its place. In this way, the vacancy is considered to have diffused with an average jump time given by τ.

Fletcher and Brown (1953) have discussed three possible ways by which vacancies disappear in an irradiated sample corresponding to three stages of annealing which occur at different times. These stages are:

1. jumping of an atom into a vacancy that is close to a deformed region of the lattice towards the interstitial and hence leading to recombination in a time shorter than the average jump time in an undistorted lattice.
2. wandering of the vacancy outside the deformed region according to random-walk process. Some of these wandering vacancies find themselves within the deformed region where they are captured.
3. wandering of vacancies away from deformed region and getting liberated.

The time dependence of the annealing in or growth for the ith site in stage 1 is given by $\frac{dN_i}{dt} = -\frac{N_i}{\tau_i}$ where N_i is the number of vacancies originally in the ith site and τ_i is the average jump time for the site towards the interstitial leading to a recombination law that has an exponential dependence on time.

Interstitial diffusion

An interstitial atom is assumed to diffuse by hopping with frequency ν from one interstitial site to another in response to thermal fluctuations. The atom undergoes a Brownian motion with a constant jump distance *d* and a diffusion coefficient $D = \frac{1}{6}\nu d^2$. The jump frequency may be considered as the frequency of jumping a potential barrier E_m. However, during a fraction of time equal to the Boltzmann factor $exp(-E_m/kT)$, the atom has energy equal to the barrier potential and so is able to make the transition. Thus the frequency becomes

$$\nu = \nu_0 e^{-E_m / kT} \tag{2.9}$$

where ν_0 is the mean frequency for the moving atom alone in the potential of the mean force due to other atoms of the solid (Wert, 1950).

2.5.3 Activation energy from isochronal annealing data

Annealing measurements are useful in the identification of defects and reactions involved in the decay of the property changes due to the defects. This entails the determination of the order of the reaction γ (see Equation 2.7) and the activation energy for migration E_m. The concentration N of a particular kind of defect present at time t obeys a differential equation of the form (Bourgoin and Lannoo, 1983)

$$dN/dt = -Kf(N) \tag{2.10}$$

where $f(N)$ is a monotonically increasing function independent of temperature. The rate constant K has the form

$$K = K_0 \exp\left(-E_m/kT\right) \tag{2.11}$$

and is a thermally activated physical quantity. The annealing temperature has the importance of allowing the correlation of observations made on the same defect but with different techniques.

A fairly accurate determination of the activation energy is then straightforward when assumptions are made about the magnitude of K_0 and the form of $f(N)$. For isochronal annealing, it is assumed that the temperature varies linearly with time from T_0 at $t = 0$ so that

$$T = at + T_0 \tag{2.12}$$

It is then possible to write

$$\frac{dN}{dt} = -K_0 \exp\left(-E/kT\right) f(N) \tag{2.13}$$

as

$$dN/f(N) = -K_0 \exp\left(-E/kT\right) dT \tag{2.14}$$

Thus in isochronal annealing, knowledge of $f(N)$ is required in order to obtain the activation energy E. If we consider first-order reaction, $f(N) = N$ so that integration of the above equation gives

$$\ln\left(\frac{N}{N_0}\right) = \frac{E}{k}\frac{K_0}{a}\int_{\infty}^{E/kT} \frac{\exp\left(-x^2\right)}{x^2} dx \tag{2.15}$$

If T_0 and T are small enough so that $E/kT_0 \sim \infty$ and $E/kT >> 1$ then we can write the equation as

$$\ln\left(\frac{N}{N_0}\right) = -\frac{E}{k}\frac{K_0}{a}\int_{\infty}^{E/kT} \frac{\exp\left(-x^2\right)}{x^2} dx \tag{2.16}$$

where $x = E/kT$. On integrating this equation by parts and retaining the first term, the resulting relation between temperature T and N/N_0 is given by

$$\ln\frac{N}{N_0} = -\frac{K_0}{a}\frac{k}{E}T^2 \exp\left(-\frac{E}{kT}\right) \tag{2.17}$$

Curve fitting techniques can be used to estimate the values of E_{m} from the measurements of N/N_0. The experimental procedure is to measure the concentration at a reference temperature T_f, say room temperature. Next, the sample is heated at the temperature $T_f + \Delta T$ for a given amount of time Δt so that $a = \Delta T/\Delta t$. After this, it is cooled down to T_f for measurements. The next anneal step consists of heating the sample at temperature $T_f + 2\Delta T$ for the same amount of time Δt. The main constraint to the use of the technique is the requirement that the time of temperature rise should be short enough in order to minimize the amount of annealing which occurs during the heating and cooling as compared to the amount that takes place at the anneal temperature T_a

CHAPTER THREE

ELECTRON PARAMAGNETIC RESONANCE THEORY

3.1 Introduction

A paramagnetic material is one whose atoms have permanent magnetic dipole moments. If a magnetic field is applied to such a material, the dipole moments try to line up with the magnetic field, but are prevented from becoming perfectly aligned by their random thermal motion. Defects in materials can also lead to unpaired electrons and hence a permanent dipole.

Electron Paramagnetic Resonance (EPR) is a spectroscopic technique for probing paramagnetic defects in materials. It has a high sensitivity for unpaired spin detection in the region of 10^{11} cm^{-3}. EPR gives information that includes the symmetry of the defect and the wave function amplitudes at the various defect nuclei. The concentration measurement of paramagnetic species is also one of the important applications of EPR.

Unpaired electrons in a solid are subjected to many electrostatic and magnetic interactions making a theoretical description of a paramagnetic entity intractable. The interactions that are typically required to describe the EPR spectra in diamond are the following:

1. Zeeman interaction which acts between the magnetic field and the magnetic moment due to the spin of the electron
2. magnetic interactions between the electron spins
3. magnetic interactions between electron spins and nuclear spins
4. nuclear Zeeman interaction
5. interaction between nuclear spins.

Due to the many interactions a complete solution of electron wave function and energy levels is not possible. Abragam and Pryce (1951) have shown that an effective Hamiltonian

may describe the behaviour of a spin system. This is called the spin Hamiltonian and it can be used to calculate most of the features of EPR spectra. A number of treatises (Abragam and Bleaney (1970); Stoneham (1975); Pake and Estle (1973)) provide detailed discussions of the spin Hamiltonian. Other useful references include the papers by Pryce (1950) and Stevens (1963).

For the defect centres discussed in this work, only the first three of these interactions are relevant.

3.2 Terms of the spin Hamiltonian

3.2.1 Zeeman interaction and the g-factor

Consider the interaction of a system with effective spin S and orbital angular momentum L in the LS coupling scheme. The spin Hamiltonian can be expressed as

$$H = \mu_B B.\left(\hat{L} + g_e \hat{S}\right) + \xi \hat{L}.\hat{S} \tag{3.1}$$

where ξ is an effective spin-orbit interaction constant, derived from the potential in which the electrons move. The $B.\hat{L}$ factor is included in the Zeeman interaction term of the Hamiltonian because it is *only* in a pure ground state that the angular momentum is zero to first order and terms involving $\hat{L}$ will vanish. In fact such states do not exist because the components of the excited states are mixed into the ground state. Details of the mixing are given in the treatise by Abragam and Bleaney (1970) and that by Stoneham (1975).

In the case of diamond, the lattice quenches the angular momentum because of the high directionality of the associated covalent bonding. However, the spin-orbit interaction, which varies as the inverse of the energy gap, is not as effective in diamond as it is in silicon due to the wide band gap in the former. In the spin Hamiltonian formalism, the above equation is replaced by

$$H = \mu_B \hat{S}.g.\hat{B} \tag{3.2}$$

where the isotropic free spin g-value is replaced by the tensor (Gordy, 1980)

$$g_{ij} = g_e \delta_{ij} - 2\lambda \Lambda_{ij}$$

where δ_{ij} is the Kronecker delta and the orbital terms Λ_{ij} can written as

$$\Lambda_{ij} = -\sum_{n \neq 0} \frac{\langle 0|L_i|n\rangle\langle n|L_j|0\rangle}{E_n - E_0} \tag{3.3}$$

The position of the excited states, relative to the ground state, depends on the angles at which the magnetic field is applied relative to the symmetry axis of the defect. Some of the structural details of the defect are therefore built into the g-tensor, so that the g-values act as probes for studying the local field symmetry. Such symmetry plays an important part in the EPR spectroscopy of crystals.

3.2.2 Zero-field splitting

A much stronger angular dependence of the EPR spectra is observed for defects which involve more than one unpaired electron, and for which the total spin $S \geq 1$. This is due to the fact that certain interactions cause the energies of spin states with different m_S states to be different even when no Zeeman magnetic field is applied. This splitting of the $|m_S|$ states is referred to as the *zero-field* splitting. Without the zero-field splitting all the $2s$ transitions will be superimposed, whereas with the zero-field splitting the EPR spectrum will consist of $2s$ fine lines. One interaction which causes zero-field splitting is the dipole-dipole interaction between the electron spins. Classically, such an interaction for two dipoles labelled 1 and 2 at distance r_{12} apart is denoted by

$$H = \frac{\mu_0}{4\pi}\left[\frac{\mu_{e1}.\mu_{e2}}{r_{12}^3} - \frac{3(\mu_{e1}.r_{12})(\mu_{e2}.r_{12})}{r_{12}^5}\right] \tag{3.4}$$

On replacing magnetic moment operators by the corresponding spin operators and simplifying we get the standard result

$$H_{SS} = \frac{1}{2} g^2 \mu_B^2 \frac{\mu_0}{4\pi} \left[\hat{S}_x, \hat{S}_y, \hat{S}_z \right] \begin{vmatrix} \left\langle \frac{r^2 - 3x^2}{r^5} \right\rangle & \left\langle \frac{-3xy}{r^5} \right\rangle & \left\langle \frac{-3xz}{r^5} \right\rangle \\ \left\langle \frac{-3xy}{r^5} \right\rangle & \left\langle \frac{r^2 - 3y^2}{r^5} \right\rangle & \left\langle \frac{-3yz}{r^5} \right\rangle \\ \left\langle \frac{-3xz}{r^5} \right\rangle & \left\langle \frac{-3zy}{r^5} \right\rangle & \left\langle \frac{r^2 - 3z^2}{r^5} \right\rangle \end{vmatrix} \begin{bmatrix} \hat{S}_x \\ \hat{S}_y \\ \hat{S}_z \end{bmatrix} \tag{3.5}$$

This therefore gives rise to a term in the spin-Hamiltonian of the form

$$H_{SS} = \hat{S}.\underline{D}.\hat{S} \tag{3.6}$$

where $\underline{D}$ is a traceless tensor. Relative to the principal axis

$$H_{SS} = D_X S_X^2 + D_Y S_Y^2 + D_Z S_Z^2 = D\left\{S_Z^2 - \tfrac{1}{3} S(S+1)\right\} + E\left(S_X^2 - S_Y^2\right) \tag{3.7}$$

where D_X, D_Y and D_Z are the principal values, $D = \frac{3}{2} D_Z$ and $E = \frac{1}{2}\left(D_X - D_Y\right)$. For the point dipoles given above, we find that

$$\begin{aligned} D_Z &= -\frac{3}{4} g^2 \mu_B^2 \frac{\mu_0}{4\pi^2} \frac{1}{r^3}, \\ D_X &= D_Y = -\frac{1}{2} D_Z \\ D &= -\frac{3}{2} g^2 \mu_B^2 \frac{\mu_0}{4\pi^2} \frac{1}{r^3} \\ E &= 0 \end{aligned} \tag{3.8}$$

If the dipole is not localised at a point then

$$D = \frac{3}{4} \frac{\mu_0}{4\pi} g^2 \mu_B^2 \left\langle \frac{r^2 - 3z^2}{r^5} \right\rangle \tag{3.9}$$

and

$$E = \frac{3}{4} \frac{\mu_0}{4\pi} g^2 \mu_B^2 \left\langle \frac{y^2 - x^2}{r^5} \right\rangle \tag{3.10}$$

where the angular brackets imply an average over the electronic wave function and the Zeeman field is taken to be along the principal direction of the $\underline{D}$-tensor. The above equations show that if the symmetry of the defect is axial the term in E vanishes whereas D vanishes in cubic symmetry; the parameters therefore provide a measure of the

deviation of the symmetry of the environment from cubic. However, if the dipole-dipole term dominates in D, then the magnitude of the zero-field splitting gives a measure of the spatial dimensions of the defect involved.

The total Hamiltonian may then be written as

$$H = \mu_B \hat{S}.\underline{g}.\hat{B} + \hat{S}.\underline{D}.\hat{S} \tag{3.11}$$

Other interactions which can give rise to the zero-field splitting are the spin-orbit coupling as discussed under in the previous subsection, Stark effect of asymmetrical crystal fields and exchange interaction.

Spin-orbit contribution to the zero-field splitting

Spin-orbit interaction can indirectly lead to coupling of the spin states and hence to a term of the form $\hat{S} \cdot \underline{D} \cdot \hat{S}$ in the spin Hamiltonian. It may be shown (Weltner, 1983; Gordy, 1980) that $D_{SO} = \xi^2 \Lambda$ where ξ is the spin-orbit coupling constant. In this relation Λ involves matrix elements connecting the ground and excited states and has been defined in Equation (3.3). D_{SO} is sensitive to the magnitude of ξ and so the spin-orbit contributions to D can be expected to be important if paramagnetic species involve heavy elements where ξ is large. Also, low-lying electronic states coupled through the matrix Λ can enhance the importance of D_{SO}.

The magnitude and sign of D depend on the spin species, the host crystal and the temperature. The values range from 0.002 to $4\ cm^{-1}$ with the majority of cases giving less than $1\ cm^{-1}$. EPR measurements at elevated temperatures cannot give the sign of D as either positive or negative. However, the study of the populations of the various absorption lines at low temperatures can enable the determination of the sign. This is because significant differences exist between more populated M_S^- and less populated M_S^+ levels at low temperatures (Low, 1960)

For systems that exhibit a E term, the values are generally an order of magnitude smaller than D. The effect of the E term is to split the pair of converging lines at the zero field ordinate; the lines become non-linear and exhibit a separation equal to $2E$. Hence two

absorption lines would occur at zero field separated by a frequency corresponding to $2E$. When B_0 is parallel to the axis of symmetry, the splitting between the lines reduces to $\Delta B = 2D / g\mu_B$ but when B is parallel to x or y, $\Delta B = \left(\left|D\right| \pm \left|3E\right|\right) / g\mu_B$ (Morton, 1964).

Electronic exchange interaction

For two interacting electrons, labelled 1 and 2, with spins S_1 and S_2 , respectively, a singlet state and a triplet state are produced. The splitting in their energies - a result of exchange interaction – is equivalent to the splitting produced by the Heisenberg Hamiltonian:

$$H_{12} = -2JS_1 \cdot S_2 \tag{3.12}$$

where J is the exchange constant. This equation can be reduced to

$$H_{12} = -J\left(S^2 - S_1^2 - S_2^2\right) \tag{3.13}$$

where a negative J means a singlet (antiferromagnet) state has the lowest energy whereas a positive J indicates that a high spin state (ferromagnetic) has lowest energy. If the interaction is isotropic then

$$\begin{aligned} -JS_1 \cdot S_2 &= -\tfrac{1}{4}J \text{ for } S = 1 \\ -JS_1 \cdot S_2 &= +\tfrac{3}{4}J \text{ for } S = 0 \end{aligned} \tag{3.14}$$

Accordingly, $J = -\left(E_{triplet} - E_{\sin glet}\right)$.

The isotropic exchange interaction has no effect upon the positions of the transitions within the triplet manifold and the interaction is generally ignored when discussing EPR spectra. The anisotropic part of the exchange interaction lifts the zero field degeneracy within the triplet state in a similar manner to the fine structure splitting (Weltner, 1983).

3.2.3 Hyperfine interaction

Hyperfine splitting of EPR lines are observed if the unpaired electron interacts with a nucleus with non-zero nuclear spin. If the nuclear spin is I then each fine structure line of

the EPR spectra will be split into $2I+1$ hyperfine lines since the selection rule for the hyperfine transitions is $\Delta m_I = 0$.

Two interactions contribute to the hyperfine splitting. These are electron-nucleus dipole-dipole interaction and a Fermi contact interaction. The former is the anisotropic part of the hyperfine structure Hamiltonian with the form

$$H_{HF} = \left(\frac{\mu_1 . \mu_2}{r_{12}^3} - \frac{3(\mu_1 \cdot r_{12})(\mu_2 \cdot r_{12})}{r_{12}^5} \right) \tag{3.15}$$

whereas the latter, called the isotropic term, is given by

$$H_C = -\frac{8\pi}{3} \mu_e \cdot \mu_n \delta(r) \tag{3.16}$$

and depends on the unpaired electron probability density at the nucleus. The symbols have been explained earlier in Equation 3.4.

Hence as for the zero-field splitting interaction discussed in the previous section and with the substitution of $\mu_e = -g\mu_B S$ and $\mu_n = +g\mu_n I$ in Equation 3.17, a term of the form $S \cdot \underline{A} \cdot I$ is obtained in the spin Hamiltonian, where the tensor components of $\underline{A}$ are given by

$$A_{ij} = g g_n \left[\left\langle \frac{3x_i x_j}{r^5} - \delta_{ij} \frac{1}{r^3} \right\rangle + \frac{8\pi}{3} |\psi(0)|^2 \delta_{ij} \right] \tag{3.17}$$

For an atomic s function, the interaction with the central nucleus comes only from $|\psi(0)|^2$, the remaining terms averaging to zero over the spherically symmetric $s-$state with the result that A is isotropic and given by

$$A_{xx}^s = A_{yy}^s = A_{zz}^s = a = \frac{8\pi}{3} |\psi(0)|^2 \tag{3.18}$$

$|\psi(0)|^2 = 0$ for an atomic $p-$function and only the dipole-dipole term gives a contribution to the hyperfine splitting. If the lobe of the $p-$function is directed along the z-axis, the hyperfine structure (hfs) tensor $\underline{A}$ will be axially symmetric around the z-axis with

$$A_{zz}^p = -2A_{xx}^p = A_{yy}^p = -2b = \frac{4}{3} g g_n \beta \beta_n \langle r^{-3} \rangle_p \tag{3.19}$$

which can be evaluated for the orbital of interest using tabulated Hartree-Fock wavefunctions. Accurate experimental estimates of $\left\langle r^{-3} \right\rangle$ can be obtained from atomic fine structure splittings (Watkins, 1975). In the cases in which the electronic wavefunction overlaps many atom sites, a linear combination of atomic orbitals centred on each of the sites involved is constructed for the unpaired electron wavefunction giving

$$\Psi = \sum_j \eta_j^2 \psi_j \tag{3.20}$$

where η_j^2 represents the fraction of the total wavefunction that is localised in the atomic orbital ψ_j centred on atomic site j. This equation represents the total wave function as a weighted sum of orbital wave functions ψ_j. Each ψ_j may be expressed as a linear combination of the s, p,… atomic orbitals on that site

$$\Psi_j = \alpha_j \left(\psi_{ns}\right)_j + \beta_j \left(\psi_{np}\right) + \cdots \tag{3.21}$$

Because the inner core shells are filled, the number n refers to the valence shell for the atom. Now $\left|\psi(0)\right|^2$ and $\left\langle r^{-3} \right\rangle_p$ strongly weights only those parts of the wavefunction very close to the nucleus. Hence the hyperfine interaction at site j results mainly from ψ_j the part of the total wave function that is atomic-like around the site j. The isotropic contribution a and the anisotropic contribution b in Equations 3.19 and 3.20, respectively, can be determined from the measured hyperfine splittings. By comparing these to the free atom values, a direct α_j^2 and β_j^2 become possible.

3.2.4 Nuclear quadrupole and Zeeman interactions

For nuclei with $I \geq 1$ dipole-dipole interaction between the nuclear spins will give a nuclear quadrupole term of the form $I \cdot \underline{P} \cdot I$ in the spin Hamiltonian. In this case the terms given by

$$\sum_j \left(S \cdot \underline{A}_j \cdot I_j - \mu_n g_{nj} I_j \cdot B + I_j \cdot \underline{P}_j \cdot I_j \right) \tag{3.22}$$

must then be added to the spin Hamiltonian of Equation 3.11.

3.3 Unpaired electron spin in a magnetic field

A free electron in a magnetic field B has two spin states with energies given by

$$E = \pm \tfrac{1}{2} g \beta B \tag{3.23}$$

where $g = 2.0023$ and β is the Bohr magneton. Transitions can be induced electromagnetically between the two spin states if the spins are subjected to an oscillating (microwave) magnetic field H_1 applied at right angles and with frequency ν to the Zeeman magnetic field B, such that

$$h\nu = g \beta B \tag{3.24}$$

Working with a frequency of $9\,\text{GHz}$ in the microwave region, one would require a magnetic field of $0.32\ \text{T}$ to achieve resonance. The spin Hamiltonian describing this system assuming effective spin S is

$$H = g \beta B S_Z + g \beta H_1 S_X = g \beta B S_Z + \frac{1}{2} \beta H_1 \left(S_+ + S_- \right) \tag{3.25}$$

where the Zeeman magnetic field B is applied along the z-axis and the microwave field H_1 along the x-axis. The selection rule $\Delta m_S = \pm 1$ follows from this equation and we note that the transition probability is proportional to H_1 and to the square of the matrix element

$$\left\langle m_S \left| S_\pm \right| m_s - 1 \right\rangle = \sqrt{S\left(S+1\right) - \left(m_S - 1\right)\left(\left(m_S - 1\right) \pm 1\right)} \tag{3.26}$$

A graph of the magnetic energy against the magnetic field B consists of two straight lines one for each of the two allowed energy states as shown in Figure 3.1 where μ is the spin magnetic moment.

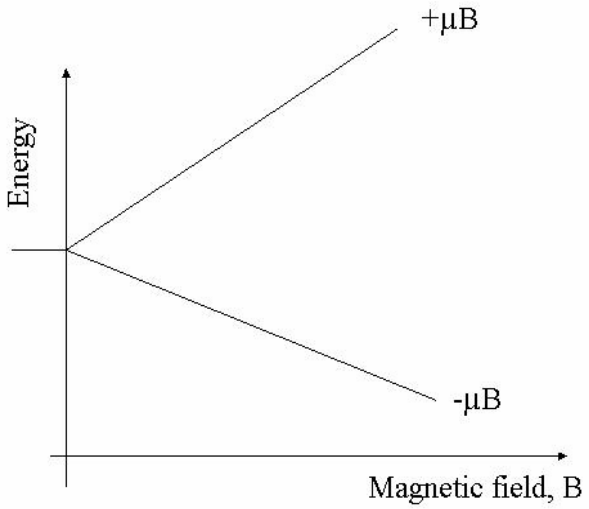

Figure 3.1: Energy levels of an electron (S=½) in a magnetic field, B.

3.4 Determination of the spin Hamiltonian parameters

Paramagnetic centres can arise from electrons that are coupled together so that $S > 1/2$. If there are no interactions with nuclear spins, the spin Hamiltonian for such systems is given by

$$H = \beta \hat{S}.\underline{g}.\hat{B} + \hat{S}.\underline{D}.\hat{S} \tag{3.27}$$

where $\underline{g}$ and $\underline{D}$ are expressed as tensors because they usually produce anisotropic effects. If the site symmetry of a defect is trigonal or tetragonal, i.e. axial, the zero-field term may be rewritten as $D\left\{S_Z^2 - \frac{1}{3}S(S+1)\right\}$ so that for $S = 3/2$, the splitting between adjacent levels is $2D$ (Orton, 1968). On the other hand, rhombic site symmetry would give rise to an extra term of the form $E\left(S_X^2 - S_Y^2\right)$. This E-term is called an orthorhombic component of the zero field splitting tensor and is usually one order of magnitude smaller than D.

The magnitude and sign of D depends on the spin species, the host crystal and the temperature. The usual experiments used to determine the sign of D are the study of the populations of the various absorption lines at low temperatures. This is because there is a

significant difference between the more populated m_S^- and less populated m_S^+ levels. Both D and E can be expressed in terms of the separation between the electrons with parallel spins if the interaction is predominantly dipolar in nature. However, if there is a significant contribution to the zero-field tensor from spin-orbit coupling, such estimates of the separation of electron spins are not feasible.

The tensors in the spin Hamiltonian are symmetric, and therefore six parameters must be determined to fully specify the tensor. Normally the three principal values and three angles, from which the principal axes can be calculated, are determined. A complication is that the principal axes of the different tensors are not necessarily parallel to each other and therefore all tensors must be transformed to a common set of axes -usually those for g -tensor.

For the diamond lattice it is convenient to measure EPR spectra in (110) planes. This is because the principal axes often lie in or close to this plane. For purposes of discussion, it will be assumed that the defect is located in or near a particular (110) plane and that all defects are covered (observable) when the magnetic field is applied at an angle $0 \le \theta_B \le 180^\circ$ relative to a $\langle 100 \rangle$ axis in each of the six (110) planes. Depending on the symmetry of the defect we may observe up to twelve sets of EPR spectra (two defects in each of the (110) planes). The angular dependencies of the zero-field splitting, hyperfine interaction and g -values are approximately as tabled below.

Table 3.1: Angular dependence for zero-field splitting, hyperfine constant and g-value.

zero-field splitting	$\frac{1}{2}D\left(3m^2-1\right)+\frac{3}{2}\left(k^2-l^2\right)$ or $\frac{1}{2}D\left(3\cos^2\theta-1\right)+\frac{3}{2}\sin^2\theta\sin^2\phi$
hyperfine interaction	$A=\frac{1}{g}\sqrt{\left(kA_1\right)^2+\left(lA_2\right)^2+\left(mA_3\right)^2}$
g-value	$g=\sqrt{\left(kg_1\right)^2+\left(\lg_2\right)^2+\left(mg_3\right)^2}$

In Table 3.1 k, l and m are the direction cosines of the magnetic field relative to the

principal axes; θ and ϕ are the polar angles. Inspection of the experimental angular plots, while keeping the characteristics of the angular variations above in mind, usually allows one to establish the electron spin, the nuclear spin and the symmetry of the defect. Subsequently, one can estimate the principal values and the directions of the principal axes. More accurate spin Hamiltonian parameters can be determined using least squares fitting of the experimental data.

For a defect with electron spin S and nuclear spin I, the EPR transitions take place between the levels of a (2S+1)×(2I+1) spin manifold. If the probability for a transition between levels j and i is non-zero, the transition will take place if

$$E_j - E_i = h\nu \tag{3.28}$$

where ν is the transition frequency.

To perform a least squares fit, it is necessary to know the direction cosines of the magnetic field for each line and the labels i and j of the levels involved in this transition. Using these direction cosines, the fields at which the transitions occur and standard eigenvalue subroutines, one can solve the secular equations for the defect, and hence calculate the residual $\left(E_j - E_i\right) - h\nu$ for each transition. The parameters for all the relevant tensors are then varied until the sum of the residuals is a minimum. Difficulties are often encountered while seeking to produce a reliable least-squares fit and reliable parameters for some tensors. One of these arises from the fact that the angle of the magnetic field with the $\langle 100 \rangle$ axis is not known to sufficient accuracy. Usually, the spectra for several centres are observed simultaneously. This makes the identification of a specific transition for a given defect difficult. If the parameters for one defect centre are known reasonably accurately, one can use its measurement to obtain a better orientation by varying it or that particular defect for a least squares fit. This angle can then be used for the other defects.

In diamond a very intense line is often observed at the centre of the spectra. This makes it difficult to know whether weaker spectra have components in this region, and hence to determine the electron spin of the defect. For example, the only difference

between $S=1$ and $S=3/2$ defect is that the latter has a line at the centre. One option to get around this problem is to look for the $\Delta m_S = 2$ transitions at half field, or $\Delta m_S = 3$ transitions at one-third field. The first will be observed if $S \geq 1$ whereas the second will be observed if $S \geq 3/2$. The variation in g-values for most centres in diamond is quite small i.e. 1 in 10^4 or less and ideally one would like to measure the g-values reliably to 1 in 10^5. From the resonance condition one gets

$$\frac{\Delta g}{g} = \frac{\Delta \nu}{\nu} - \frac{\Delta B}{B} \tag{3.29}$$

and for $B = 3200$ G and $\nu = 9$ GHz accuracies better than 0.03 G. It is hardly possible to achieve these accuracies with the equipment being used. The difference between the magnetic field at the point where the sample is situated and that at the point where it is measured (position of Hall probe), for example, is likely to be outside this limit. The best that can be done is to compare g-values of centres occurring in the same sample.

Once the parameters are known, one can use the eigenfunction for the levels and calculate the transition probabilities. The EPR spectra can then be simulated for a particular angle by superimposing all the transitions for all six (110) planes.

3.5 Simulation of EPR spectra

It is usually necessary to simulate EPR spectra so as to compare with the experimental spectra, as this would be a check on the precision of the parameters of the particular spin Hamiltonian used. Simulation of magnetic field-swept EPR spectra entails the construction of an effective spin Hamiltonian consistent with lattice symmetry, the solving of each spin Hamiltonian for transition fields, the calculation of the transition probabilities as well as the corresponding energy levels. It is equally necessary to weight each transition probability by the spin populations in the energy levels involved. In order to carry out simulation of EPR spectra for diamond, the interaction tensors of the effective spin Hamiltonian are rotated using the 3D rotation matrix of the T_d point-group (Tucker, 1995). The rotation reflects symmetry of the defect; for instance, if the effective spin Hamiltonian is given by

$$H = \mu \hat{S} . \underline{g} . \hat{B} + \hat{S} . \underline{A} . \hat{I} \quad (3.30)$$

then $\underline{A}$ will be transformed as

$$A' = R^{-1} \underline{A} R \quad (3.31)$$

for all R in the representation producing a set of twenty-four Hamiltonians. Here g is not rotated as it is isotropic. Each spin Hamiltonian is then diagonalized for a particular Zeeman field direction and microwave frequency.

Simulated spectra have been used in the work reported here to determine $\Delta m_s=2$ and $\Delta m_s=3$ spectra which do help to identify centres with S>1.

CHAPTER FOUR

EXPERIMENTAL METHODS

4.1 Introduction

The EPR spectra in this work were recorded using either the continuous wave (CW) Varian E-Line X-band spectrometer with standard TE_{102} cavity or the Bruker ESP 380 pulsed EPR spectrometer. Using the former, the data was collected using a PC with an Eagle Technology's A/D converter.

Variable temperature experiments from 6 to 300 K were obtained using a continuous flow cryostat and nitrogen flow heat exchanger.

4.2 X-band EPR spectrometer

We used a homodyne X-band Varian EPR spectrometer that was operating in the absorption mode at a nominal 9.5 GHz and for which a block diagram is given in Figure 4.1. The following is a brief description of operating the procedures. Detailed description of the various components of the spectrometer may be obtained from the classic treatise by Poole (1983).

The microwave power is provided by a Varian water-cooled klystron whose output power is in excess of 200 mW and a power stabilizer placed immediately after the klystron reduces this to exactly 200 mW. The frequency stabilization is achieved by means of the automatic frequency control (AFC) unit of the EPR microwave bridge since regulated power supplies alone do not afford the required stability. The bridge uses a three-port microwave circulator.

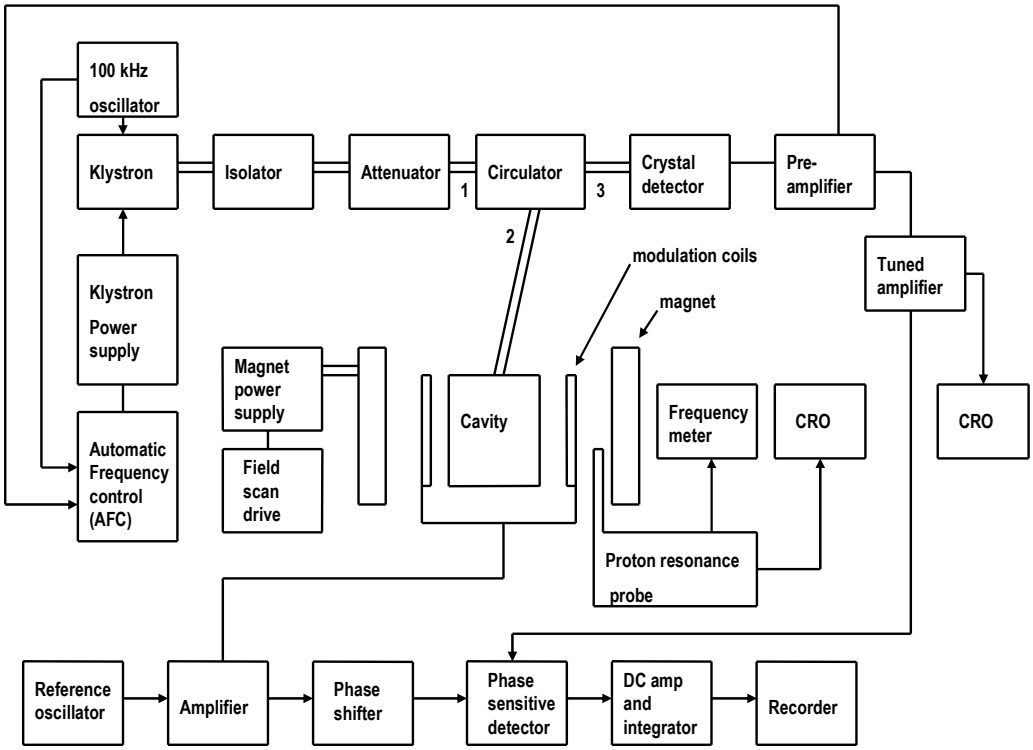

Figure 4.1: Block diagram of the Varian E-Line Century Series EPR spectrometer**.**

4.3 Concentration measurements

Absolute concentration of these centres depends on factors like the area under the absorption curve, the modulation amplitude at the sample, the magnitude of the microwave magnetic field H_1, the overall spectrometer gain, the sample temperature, the effective spin S of the paramagnetic species, the g-factor, the microwave frequency and the filling factor (Weil *et al.*, 1994). In practice concentration measurements are obtained by relative methods. The unknown concentration $[X]$ is related to the known standard concentration $[std]$ according to the following equation (Weil *et al.*, 1994):

$$[\mathrm{X}]=\frac{[std]\,A_x R_x \left(scan_x\right)^2 G_{std} M_{std} \left(g_{std}\right)^2 \left\{S\left(S+1\right)\right\}_{std}}{A_{std} R_{std} \left(scan_{std}\right)^2 G_x M_x \left(g_x\right)^2 \left\{S\left(S+1\right)\right\}_x} \tag{4.1}$$

where A= area under the absorption curve obtained by double integration or first moment; S= effective spin; $scan$ = horizontal scan in gauss per length; G = relative gain of the signal amplifier; M = modulation amplitude in gauss; $R=\frac{\sum D_j}{D_k}$ with D_k denoting the degeneracy of the most intense line of a set of hyperfine lines, and $\sum D_j$ is the sum of the degeneracies of all the lines in the spectrum.

This relative method was used in this work to make measurements with a type Ib diamond standard containing 7.1×10^{18} spins which was calibrated in the 200 G scan range. The cavity quality factor Q was determined using the relation $Q=\frac{\omega_0}{\Delta\omega}$ where $\Delta\omega$ is the frequency difference between the half power points of the tuned cavity.

4.4 Frequency and magnetic field measurements

Though either the microwave frequency or the magnetic field can be varied in EPR experiments for resonance condition to be attained, it is more practical to vary the magnetic field since the tuning of frequency sensitive cannot be easily automated.

The resonance frequency of the Varian CW TE_{102} rectangular cavity was measured using a 5255A HP frequency converter working in the range of 3 to 12.4 GHz and which takes its input from the microwave bridge. Once the resonance is found, the gaussmeter locks onto it and then measures the frequency, converts it to gauss and then displays. The accuracy of the gaussmeter was about 1×10^{-6} T.

4.5 The Bruker ESP 380 EPR X-band spectrometer

The spectrometer operates both in continuous and pulsed EPR modes. In the continuous mode, the spectrometer was used to carry out saturation measurements for EPR centres in type Ib diamond. This was necessary in order to check on similar measurements on the

Varian CW EPR spectrometer. The two sets of measurements could then be used to make a calculation of the spin-lattice relaxation time T_1 and the spin-spin relaxation time T_2.

Direct measurements of T_1 and T_2 for vacancy related centres may be determined using the Bruker pulsed EPR spectrometer. In the pulsed saturation method of measuring the relaxation times, the spin system is saturated with a high power pulse of microwave energy following which the amplitude of the EPR signal is measured at various times to monitor the rate at which the magnetization returns to its equilibrium value. However, due to very small T_1 for centres studied in this work, the CW method was used instead.

4.6 Mounting and orienting the sample in the cavity

For most spectra in diamond, accurate orientation of the crystals with the magnetic field is extremely important. This is facilitated by cutting and polishing the crystals with faces having known Miller-indices *viz* $\{111\}$, $\{110\}$ or $\{100\}$ which have been determined by X-ray diffraction or Laue back-reflection techniques. This applied to all the crystals that we used for this thesis.

To obtain the symmetry of defects that are found in diamond, angular variation experiments are carried out. The specimen is rotated about either a $[100]$ axis or more commonly, a $[110]$ axis while mounted on a quartz rod, which is then held by a goniometer and rotated about its axis. Therefore the axis of the rod must be parallel to $[110]$ or $[100]$-axis.

In our experiments, if the specimen had a $\{110\}$ face, then it could be glued with the face flush with the end of the flat-end cylindrical quartz rod. If the faces were $\{100\}$-planes, as in samples J1 and J2, then to obtain all the three crystallographic directions in subsequent angular variation measurements, the sample had to be glued to a stepped-end cylindrical quartz rod. The glues we used, invariably Bostik glue, were capable of setting quickly as well as retaining consistency from room temperature to cryogenic temperatures. The quartz sample rods were usually 5 mm in diameter.

It is generally easier to do an EPR angular variation measurements if the crystal is inserted into the cavity with some crystallographic direction very nearly parallel to the magnetic field B. With polished crystals this can be estimated by visual inspection after which an orientation can be obtained by rotation of the goniometer and the magnet until known spectral patterns overlap appropriately for a given crystallographic axis. If an appropriate axis is very close, the lines that will eventually superimpose are shown to be very close to one another. In this case a slight orientation of the goniometer or the magnet should give well-superimposed lines.

In the general case, it is not clear which lines belong to which centre. Normally the outermost line is followed as the orientation is varied in such a way that the line moves towards the centre of the spectrum until it crosses another line. This procedure works unless the centre in question has a $\langle 110 \rangle$ or $\langle 100 \rangle$ symmetry in which case the outermost line will be at $90°$ limit or $0°$ limit, respectively (Lea-Wilson, 1988). It is easy to detect when a $[100]$-crystallographic direction has been obtained because a large number of lines are then superimposed throughout the spectrum. A fine adjustment is accomplished by the rotation of the goniometer and the magnet to obtain a superposition as accurately as possible. This adjustment is best done by using a line that is relatively very sensitive to orientation as indicated by the ease with which it splits with orientation. The line can be picked out from theoretical angular variation curves or from trial and error.

For instance in the work reported here, the electron-irradiated type Ib diamond samples contained P1 (single substitutional nitrogen) centers, which aided in the orientation. However, this was not available in the neutron-irradiated type Ib crystal for which R1 (di-$\langle 100 \rangle$-split interstitial) centre was used instead. Hence knowledge of the spectral pattern for the P1 or R1 in the crystallographic directions was necessary (Lea-Wilson, 1988; Smith *et al.*, 1959; Loubser and van Wyk, 1978). After finding one crystallographic direction, the other two were easier to obtain. The goniometer setting would be almost correct if it was rotated by $54.7°$ to get $[111]$ or $90°$ to get $[011]$ if one started from $[100]$. All that usually remained at that stage was the adjustment of the magnet and a small adjustment of the goniometer. A full angular variation experiment could be done by first aligning the $[100]$-

crystallographic axis parallel to the magnetic field B and then rotating the goniometer in steps of, say $2°$, all the way to the $[110]$ direction. To ensure that the plane of rotation was always $\{110\}$ at each $2°$ step, the magnet was adjusted to bring the magnetic field B into the $(01\bar{1})$ plane. The result was that some pairs of lines remained superposed and these were continually tracked.

4.7 Low temperature measurements

Low temperature measurements were carried out using the Varian liquid nitrogen accessories (V-4546) in conjunction with the variable temperature accessories (V-4547) and the Oxford Instruments continuous flow cryostat (CFC).

4.8 Continuous wave (CW) saturation measurements

The CW saturation method is employed mostly with standard spectrometers and is based on the assumption that the spin system obeys the Bloch equations (Poole, 1983).

The CW method involves the recording of spectra at various power levels near the onset of saturation. The changes that occur in the widths and amplitudes of the EPR lines are used in the determination of the relaxation times. T_2 can be determined from the width of the spectra before saturation if no broadening mechanisms are causing the experimental linewidth.

The experimental procedure is as follows. EPR spectra at different power levels are recorded. H_1 may be calculated if the calibration of the incident power has been done, for example, by means of a Hewlett-Packard power meter. Based on the power incident on the cavity one calculates this quantity from the equation (Poole, 1983)

$$H_1^{\,2} = KP_w \tag{4.2}$$

where H_1 is in gauss, P_w in watts and K is typically of the order of unity.

A saturation method due to Castner (1959) is adopted in chapter 11 of this work in the discussion of the relaxation times based on saturation measurements. The method enables independent determination of the spin-packet width $1/T_2$, as well as T_1 and the product T_1T_2. Castner showed that the spin-packet width is not limited by T_1.

CHAPTER FIVE

OVERVIEW OF IMPORTANT CENTRES IN TYPE Ib DIAMOND

5.1 The neutral vacancy (V^0) and the negative vacancy (V^-) centres in diamond

5.1.1 The neutral vacancy

Room temperature irradiation with $1-2$ MeV electrons is sufficient to create isolated lattice vacancies in diamond. The vacancy and the interstitial are the primary defects created by irradiation.

Clark *et al.*(1961) provided the first estimates of the threshold energy for the creation of a vacancy-interstitial pair (or Frenkel pair) in diamond using high-energy electron scattering measurements. Theoretical work based on considerations of bond and crystal strain energies led to a value of $20-30$ eV (Bourgoin and Massarani, 1976). However, estimates based on ion bombardment studies by Prins *et al.*(1986) gave a much higher value of 55 eV. A theoretical modelling of single atom radiation damage by Wu *et al.* (1994) indicated the dependence of threshold energy for dislodging a lattice atom on the initial direction of displacement. This latter group of researchers found that for initial displacement along the directions <100>, <110> and <111> the required threshold energies were 47, 50 and 54 eV, respectively. In diamond, the interstitials are thought to migrate during the irradiation and (most probably) produce interstitial-related centres (Kim and Watkins, 1971).

Depending on the charge equilibrium within the diamond, the vacancy can exist in the neutral charge state or in the negative charge state (Davies *et al.*, 1992). The defect has a major role in defining the intrinsic and extrinsic electronic and optical properties of diamond. In addition, the vacancy plays a dominant role in self-diffusion in this material. By contrast, theoretical studies of Bernholc *et al.* (1988) suggested that the self-diffusion in

silicon and germanium proceeds in such a manner that the vacancy, the interstitial and direct exchange mechanisms all play comparable roles. This difference was attributed to the stiffness of diamond bonds which hinder twisting and large relaxations.

The neutral vacancy V^0 gives rise to the GR1 optical absorption centre which has a zero-phonon line (ZPL) at 1.673 eV and phonon assisted peaks at higher energies centred at about 2.0 eV according to extensive experimental and theoretical studies (Davies, 1974, 1981). It is a transition between an E ground state and a T_1 or T_2 state (Davies, 1994). Signals have been observed from an excited pentad (S=2) of the vacancy in electron-irradiated very high quality natural type Ia diamond (van Wyk *et al.*, 1995). The GR1 signals have been used extensively to estimate vacancy concentrations (Davies *et al.*, 1992; Lawson *et al.* 1998; Twitchen, *et al.* 1999; Iakoubovskii and Andrienssens; 2003). The GR1 centre remains constant in concentration following irradiation and annealing of diamond until about 600 ^{o}C when it starts to disappear. The annealing out is complete at about 800 ^{o}C (Lea-Wilson *et al.*, 1995).

Davies *et al.* (1992) have carried out measurements suggesting that the single negatively charged vacancy V^- undergoes a reversible charge transfer process to the neutral charge state which in turn migrates with activation energy of 2.3 eV. The negative vacancy is prominent in type Ib diamond due to the availability of donor electrons from the substitutional nitrogen.

5.1.2 The negative vacancy (V^-)

Baldwin (1963) observed an EPR spectrum, referred to as S1, which consists of a strong central peak and some weaker peaks in its vicinity. Isoya *et al.* (1992) verified that the spectrum is due to negative vacancies and determined the spin state using the nearest neighbour ^{13}C ENDOR frequencies as these depend on the value of m_S, the magnetic electron spin quantum number. Now, to determine effective spin S in EPR, one must observe fine structure. For S1, this is not possible and hence the use of ENDOR is necessary. Calculated ENDOR frequencies are given by $h\nu = \left| m_S A_{eff} - g_n \mu_n B \right|$, where A_{eff} represent the hyperfine splitting and B is the external applied magnetic field. Isoya *et al.* (1992) measured A_{eff} from the EPR and compared the results with the values that they

obtained from the ENDOR frequencies as the m_S in the above expression was varied. This led to verification of the effective spin as $S = 3/2$.

The ND1 optical absorption system has a sharp zero-phonon line at 3.148 eV and phonon-assisted structure centred at about 3.4 eV. It is observed in irradiated diamonds containing nitrogen but anneals out when the vacancies become mobile. This centre was shown by Davies (1977) to arise from the electron capture by vacancies when the nitrogen centres act as donors; the EPR S1 spectrum is associated with the same defect.

It is presently accepted that the properties of the vacancy are determined by the electrons in the dangling bonds on the carbon neighbours surrounding the vacancy. The T_d point group requires that these orbitals transform as a_1 and t_2. In the negatively charged vacancy five electrons are accommodated in these orbitals. From the configuration $a_1^2 t_2^3$ the $^4A_2$ ground state with effective spin S=3/2 is derived and so are the excited states ^2E, $^2T_1$ and $^2T_2$. For a system with T_d symmetry, there is no zero-field splitting i.e. the term $\hat{S}.\underline{D}.\hat{S}$ in the spin Hamiltonian of Equation 3.5 vanishes.

The usual method of obtaining concentrations from the first derivative peaks could not be used for S1 due to the complex a-line that superimpose with it at the centre of the spectrum. Instead, the ^{13}C hyperfine peaks of the centre, shown in Figure 5.1, were used to determine the concentration of the S1. The ^{13}C has a natural abundance of 1.1 % and therefore the intensity of the hyperfine lines compared to the ^{12}C line at the centre is 1:45.

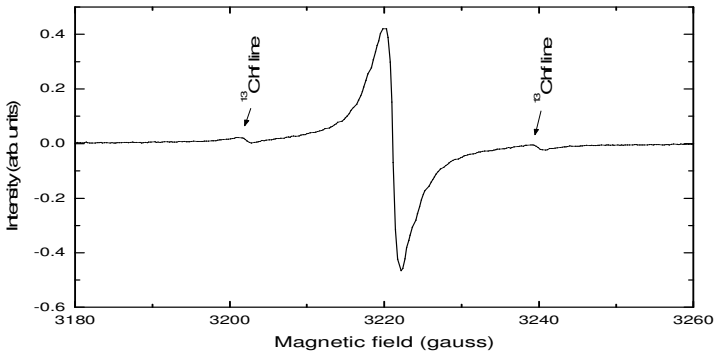

Figure 5.1: Nearest neighbour hyperfine lines of ^{13}C due to S1 with the magnetic field in the <100>-direction. This was after 500 ^oC isochronal annealing. The central peak consists of merging lines mainly S1 and a-line**.**

Another important vacancy-associated centre is the neutral divacancy, the R4/W6 (Lea-Wilson *et al*., 1995; Twitchen *et al.,* 1999) which will be introduced in chapter 9 and discussed more in chapter 11 following measurements on linewidth and spin lattice relaxation.

5.2 The self-interstitial and multi-interstitial EPR centres

5.2.1 Self-interstitial EPR centre R2

The self-interstitial together with a vacancy are always the dominant defects created in extrinsic defect free diamond, or type IIa, on room temperature irradiation with 2 MeV electrons as well as by neutron and gamma irradiation. The spectrum for this centre was first observed in electron-irradiated type IIa diamond by Faulkner and Lomer (1962) but it was also observed soon after in type Ib diamond. The centre has $S = 1$ and the principal axis of the zero-field tensor for its spectrum points along the $\langle 100 \rangle$ -direction.

Walker (1977) found a correlation between the R2 EPR centre and the optical absorption lines at 1.685 and 1.859 eV. In addition, the signals were destroyed under the same annealing conditions. The fact that the production rates for the centre and the vacancy V^o are similar suggests that it must be a primary defect with a simple structure.

Early models for the R2 centre include the highly strained vacancy due to Mainwood *et al.* (1993). These authors proposed the model consisting of a neutral vacancy displaced along the <100> from a neutral split interstitial aligned along <100> directions. According to the model, the interstitial acted to provide stress which compressed the vacancy along the <100> directions. They proposed that the EPR line observed originated from the $^3B_1$ state of the compressed vacancy derived from the $^3T_1$ state of the uncompressed vacancy. The compression lowered the energy of the $^3B_1$ to the observed 39 meV and produced a splitting of about 10 meV between the $^1A_1$ and lower $^1B_1$ component derived from the ^1E ground state of the uncompressed vacancy V^o. The 1685 meV line corresponded to the transition between $^1A_1$ and the excited $^1B_2$ state. This explained the lower state 6 meV above the ground state. The interstitial was assumed to be in its S=0 state.

Using *ab initio* techniques, Breuer and Briddon (1995) concluded that the only stable structure for an interstitial atom was the $\langle 001 \rangle$ -split interstitial. They found this to be true for the neutral, -1, +1 and +2 charge states. The tetrahedral, hexagonal, bond-centred and $\langle 110 \rangle$ -split interstitial sites were all shown to be unstable. Among other features, the symmetry of a self-interstitial thus concurs with the compressed vacancy model discussed above.

However, a major objection to the compressed vacancy model has been raised by Hunt *et al.* (2000a) as being the difficultly of creating the unique (I-V) configuration; they argued that the chance for such an event due to direct impact is very small. This group subsequently proposed a model that is currently accepted and which we now discuss.

The proposed model of Hunt *et al.*(2000a) for the R2 centre consists of a neutral $\langle 100 \rangle$ -split interstitial with electrons located in the $2p_\pi$ orbitals as shown in Figure 5.2. The EPR signal arises from a spin-triplet excited state of the self-interstitial 50 meV above the singlet ground state and cannot be observed below 120 K. Its linewidth is large varying between about 2.5 and 5.0 mT.

Hunt *et al.* (2000a) also analysed the angular variation of the ^{13}C line broadening in 50% ^{13}C enriched diamond. The enrichment allowed the determination of the localized unpaired electron probability density in the two non-bonding p_π orbitals of the <001>-split interstitial.

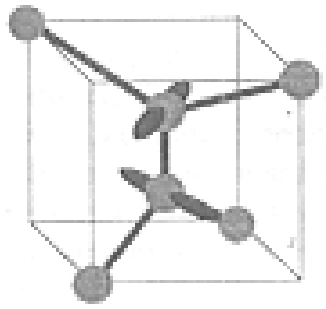

Figure 5.2: The <100>-split interstitial model for the R2 centre in diamond. The carbon atoms connected by the vertical lines are each bonded by sp2-hybrids to yield $2p_z$ orbitals shown as lobes. This diagram has been taken from Hunt *et al.* (2000a).

Hunt *et al*., (2000a) reported migration energy of the self-interstitial as 1.6 eV which is significantly lower than the 2.3 eV for the neutral vacancy.

5.2.2 Multi-interstitial EPR centres R1 and O3

The R1 EPR centre

The R1 centre is formed after room temperature irradiation in all diamond types. The centre is always observed with the R2 centre and both of them anneal out at roughly the same temperature. The EPR line for the R1, however, is much narrower but its concentration is usually much smaller. The similarity in the annealing behaviour of the two centres suggests common constituents in their structures.

A study by Twitchen *et al.* (1996) has yielded a model for the R1 EPR centre as a di-$\langle 001 \rangle$ -split interstitial depicted in Figure 5.3. The determination of the structure by these researchers was facilitated by the use of $5\,\%$ ^{13}C isotopically enriched diamond samples. An analysis of the ^{13}C hyperfine structure couplings using molecular orbital calculation enabled them to further show that the centre can be viewed as a biradical consisting of two unpaired electrons each localized primarily in a non-bonding $2p$ orbital on different carbon atoms.

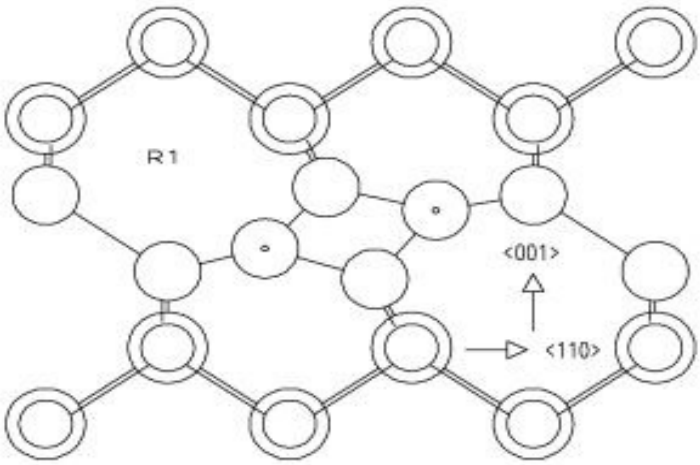

Figure 5.3: The di-<001>-split interstitial model for R1 in the diamond lattice.

Pioneering studies of the annealing behaviour of the R1 centre were carried out by Clark *et al*. (1964) who reported an annealing temperature of between 570 K and 670 K. Other workers have reported similar results (Twitchen *et al*., 2001). As for the R2 centre, Clark *et al*. (1964) found that it annealed out in the range 670K to 720 K. However, measurements by van Wyk (1999) found a slightly lower annealing temperature (620 K to 670 K).

The fact that the centres R1 and R2 anneal out at nearly the same temperature suggests that the annealing process of R1 does not entail a dissociation into constituent I^o (<001>-slit-interstitial) as that would lead to a growth of the R2 centre (Twitchen *et al*. (2001)). Thus the process may consist of the R1 constituent self-interstitials moving apart to form the defect I^o-C-I^o with parallel I^o where C is the lattice carbon atom. This structure was first proposed by Humble (1982).

Diffusion studies on the self-interstitial and the neutral vacancy in type IIa diamonds, irradiated with 2 MeV electrons at different temperatures suggest that the rates of production of these two defects were the same at low irradiation temperatures (Davies *et al.* (2001); Newton *et al.* (2002)). When the irradiation temperature exceeded about 120 K, a significant loss of the observable I^0 by a process that is not yet understood was detected. To explain this scenario, Davies *et al.* (2001) have postulated the existence of barriers to reactions between defects that give rise to various metastable configurations.

More recent measurements have been made by Iakoubovskii *et al*. (2003) in type IIa diamond irradiated at room temperature with 3 MeV electrons to a dose of 2×10^{18} e/cm^2. Their fractional concentrations relative to V^o were typically 0.1- 0.3 for R2 and 0.01- 0.03 for R1 suggesting that almost 70 % of the interstitials are not account for. Subsequently, Iakoubovskii *et al*. (2003) proposed a model which suggests that the interstitials are found in other charge states not observable by EPR. Accordingly, they suggested that the R1 does not anneal out at about 400 ^{o}C as deduced from isochronal annealing measurements. Instead the centre appears to convert to other centres from which it can be restored by illumination.

The O3 EPR centre

The O3 EPR centre has been observed in both type IIa and type Ib synthetic diamonds after electron and neutron irradiation, respectively. It has $S = 1$ and C_2 symmetry with a two-fold rotation axis about $\langle 100 \rangle$. Hunt *et al.* (2000 b) have proposed two models involving parallel $\langle 100 \rangle$ -split interstitials ; these are given in Figures 5.4 (a) and (b) and consist of two and three such interstitials, respectively, at nearest-neighbour positions. The former model gave a better fit to experimental data.

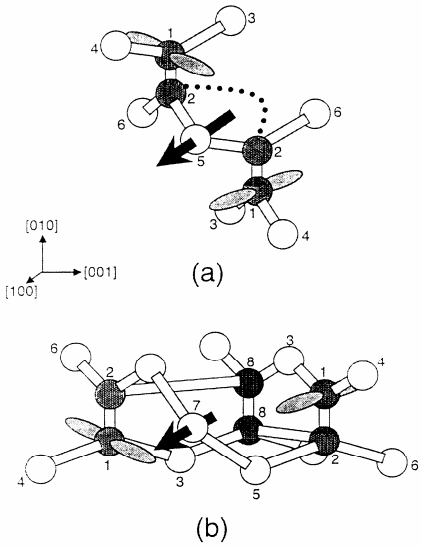

Figure 5.4 : The O3 EPR centre in diamond. (a) Two <001>-split interstitials; (b) Three <001>-split interstitials. Taken from Hunt *et al.* (2000 b).

The above interstitial-related centres *viz*, R1, R2 and O3 are observed in the same annealing temperature ranges with the W11-W14 EPR centres. This will be shown in the annealing curves of Figure 6.5 and may be taken as a suggestion that the W11-W14 centres also involve the self-interstitial or self-interstitial mobility.

5.3 The nitrogen impurity complexes in diamond

5.3.1 The W15 EPR centre

Optical absorption measurements on type Ib diamond annealed to a least 650 ^{o}C reveal a sharp zero phonon line (ZPL) at 1.945 eV which is associated with a vacancy being

trapped next to a single nitrogen atom (Davies *et al*. 1976) and which gives rise to an electron spin resonance signal called the W15 under optical illumination (Loubser and van Wyk, 1977; Loubser and van Wyk, 1978).

The W15 is one of the most studied EPR centres in electron-irradiated type Ib diamonds (du Preez, 1965; Davies and Hamer, 1976; Loubser and van Wyk, 1977; Redman *et al*., 1991; He *et al.*, 1993; Mita, 1996). Although it was observed in sample J4 after an annealing at 400 ^{o}C, its intensity initially increased slowly at annealing temperatures below 600 ^{o}C but then showed marked increases at higher annealing temperatures i.e. the temperature at which the vacancy becomes mobile. Its zero-field fine structure tensor is axially symmetric around a <111>-axis and the effective electron spin is 1. The model for W15 shown in Figure 5.5 has been verified by the hyperfine interactions of the unpaired electrons with the nitrogen and the carbon atoms A, B and C in the figure.

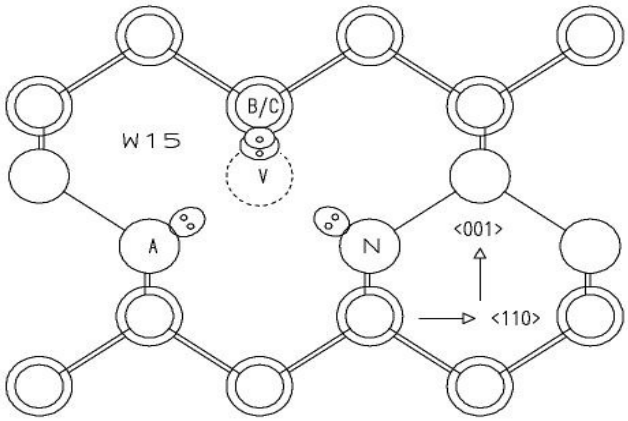

Figure 5.5: A model for W15 centre in diamond. The principal axis is in the <111> direction (NV). The small circles are shown concentric with bigger ones. These are respectively, atoms in {110}-planes below and above the (110)-plane containing the vacancy and which is coincident with the plane of the page.

The fact that the electronic spin S=1 for W15 shows that it involves an even number of electrons, whereas for a neutral N-V pair the number should be odd. It has been suggested that the W15 is negatively charged (Mita, 1996; Goss *et al.* 1997).

The spin triplet for the W15 centre was first observed by Loubser and van Wyk (1977) who subsequently showed that the centre has a near isotropic g-value of 2.0028±0.0003

and a zero-field splitting of $|D| = 2.88\,\text{GHz}$ (Loubser and van Wyk, 1977: Loubser and van Wyk, 1978). Other techniques namely holeburning (Reddy *et al*. 1987), ODMR (van Oort *et al*., 1988) and EPR (Redman *et al*., 1991) have established that the triplet state is a ground state.

Other investigations have suggested that the W15 is an important example of centres in diamond that occur in more than one charge state. For example, it occurs in the neutral charge state $[\text{N-V}]^0$ with a zero-phonon line at 575 nm (Mita, 1996) as well as in the single negative charge state $[\text{N-V}]^-$ with a zero phonon line at 637 nm (Davies and Hamer, 1976). Manson *et al*. (2006) have reported that the centre in its negative charge state is not photochemically stable such that with intense excitation, it converts to the neutral charge state.

Current renewed interest in the N-V centre

The fact that N-V centres form a very promising candidate for quantum computing has generated intense research interest recently (Hanson *et al.*, 2006; Reddy et *al.*, 1987; van Oort *et al.*1990). Accordingly, the centre is about the most studied impurity complex in diamond.

5.3.2 Other important nitrogen-vacancy centres in type Ib diamond

Besides the W15 centre, other important nitrogen-vacancy centres in diamond include the EPR centres W26 and W25 which are associated with the excited states of the H3 and H4 optical centres, respectively (van Wyk and Woods, 1995). However, these are found only in aggregated forms of diamond and will not be discussed here.

CHAPTER SIX

ANNEALING CURVES

6.1 Introduction

EPR spectra of numerous defects are observed in both electron- and neutron-irradiated diamonds. Many of these defects are observed in all diamond types but some are observed only in specific types. Some of the defects are present immediately after irradiation and will grow or anneal out at certain isochronal anneal stages. The studies in this thesis will be concerned with a small number of these defects following isochronal annealing.

6.2 The samples

Measurements on the various EPR centres were carried out using four different synthetic type Ib diamonds J1, J2, J3 and J4 with markedly different concentrations of P1. For the majority of experimental results reported in this work, we used sample J4. The identification properties for these stones are presented in Table 6.1 in which [P1] stands for concentration of P1 before irradiation.

Table 6.1: The diamond samples**.**

Sample code name	Mass (mg)	Thickness (mm)	[P1] (ppm)
J1	17.5	1.02	254
J2	14.6	0.88	386
J3	23.0	0.60	100
J4	97.0	1.44	120

The stones J1, J2 and J3 had been irradiated at room temperature with 1.08×10^{18} electrons of energy 2 MeV using a van de Graaff generator at the University of Reading, UK. The irradiation has been discussed by Lea-Wilson (1988). EPR measurements were made by

mounting the stones in such a way that they could be rotated around a <110>-axis. This would enable the orientation of the <100>, <110>, and <111> crystal axes, in turn, along the static magnetic field.

The sample J4 was neutron-irradiated at the South African Nuclear Centre at Pelindaba near Pretoria, to a dose of 5×10^{17} neutrons per cm^2. After irradiation, the sample was annealed in stages up to 850 ^oC.

6.3 P1 concentrations determined using infra-red spectroscopy

In diamond research, the GR1 (Davies, 1974, 1981, 1994), ND1 (Davies, 1977, Isoya *et al.*, 1992) and 1859 meV centre (R2) (Walker, 1977; Mainwood *et al.*, 1993; Hunt *et al.*, 2000a) have been studied mostly using optical absorption (OA). It is important to note that the OA and EPR are complimentary techniques that are commonly used in the study of defects in diamond.

Infra-red (IR) measurements were carried out using a Bruker Vector 22 infrared FT spectrometer at the Chemistry Department of the University of the Witwatersrand on J1, J2 and J3. The aim of the measurements was to determine the P1 centre (isolated nitrogen) concentration in the type Ib diamonds.

The IR absorption spectra for the samples J1 and J3 are shown in Figures 6.1 and 6.2, respectively. The broad peak at approximately 1130 cm^{-1} is characteristic of type Ib diamond (Woods, 1990). The sharp local mode peak found very close to 1344 cm^{-1} is observed in EPR as the P1 (Smith *et al.*, 1959) and has been shown to be a deep donor with ionization energy of 1.7 to 2 eV (Farrer, 1969). The P1 concentrations are given in Table 6.2.

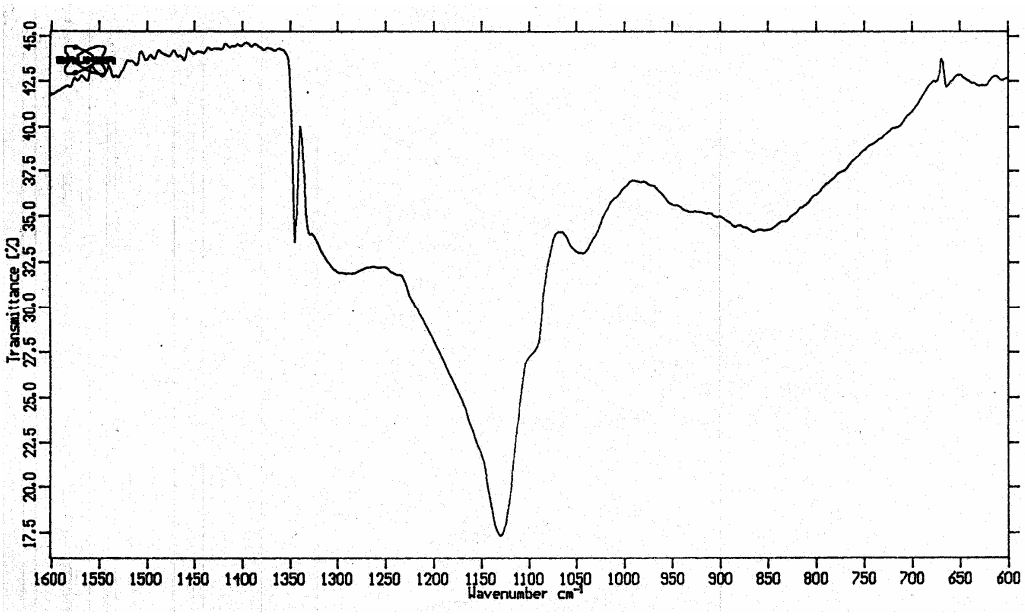

Figure 6.1: IR transmission (%) versus energy in cm^{-1} for sample J1 before annealing.

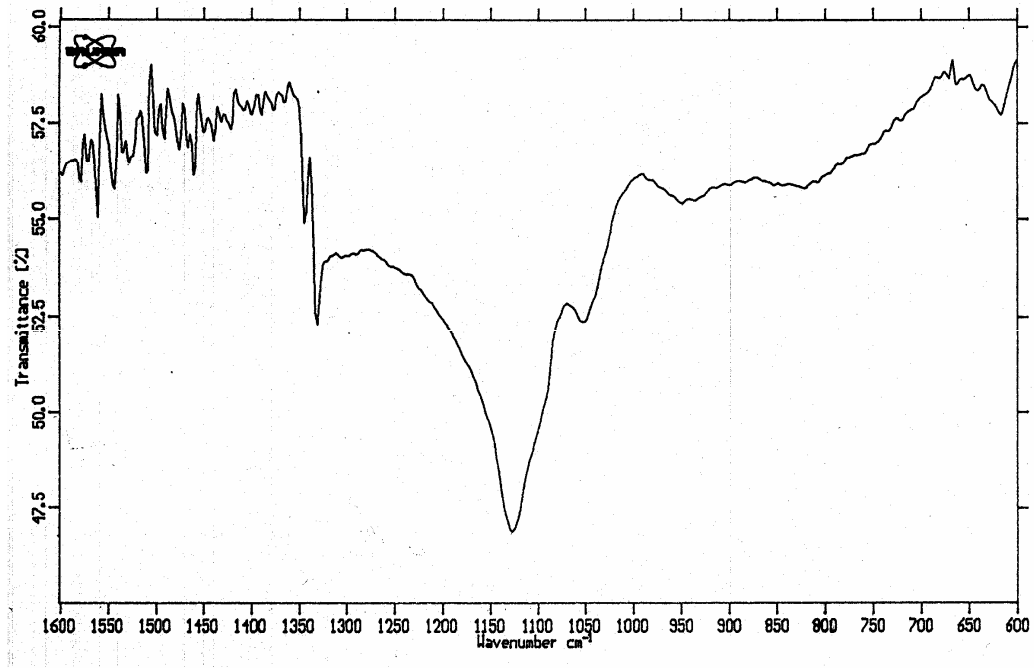

Figure 6.2: IR transmission (%) versus energy in cm^{-1} for sample J3 before annealing.

From the IR spectra, the substitutional nitrogen concentration N_s is obtained from I_b, the baseline intensity, and I, the intensity at 1130 cm^{-1}. The relation is

$$N_s = K_s \times \mu \tag{6.1}$$

where the absorption coefficient $\mu = \ln\left[\left(\frac{I_b}{I}\right)t^{-1}\right]$ with t being the thickness and proportionality constant K_s=25±2 (Kiflawi *et al.,*1994).

Table 6.2: P1 concentration in electron-irradiated diamonds obtained from IR absorption measurements**.** Though P1 was observed in J4 before irradiation, it could not be observed by EPR following the neutron-irradiation.

	Thickness (mm)	P1 concentration. by EPR (ppm)	P1 concentration by IR (ppm)
J1	1.01	254	235±18
J2	0.88	386	401±32
J3	0.60	100	92±7

Clearly, the IR absorption measurements yielded concentration values comparable to those obtained during initial characterization using EPR. Thus, these results provided a useful check on the concentration measurements.

6.4 Annealing curves for selected centres

The second derivative EPR spectra for the centres observed in sample J4 are given in Figures 6.3 and 6.4. The annealing behaviour of the relevant defects as measured in this work is shown in Figure 6.5 in which the concentrations presented have been obtained as explained in chapter 4.

It is generally accepted that interstitials, or at least some interstitials, are mobile below 450 ºC, while vacancies become mobile above 600 ºC. Where possible, models for the defects will be given or discussed later in the thesis.

The defect centres with names starting with R were first observed at the EPR laboratory of the University of Reading whereas those whose names start with W were first observed at the University of the Witwatersrand. The centres R1 and R2 are observed in all diamonds, S1 and W29 in both type Ia and type Ib diamonds, while W11, W12 , W13 and W14 only

in type Ib diamonds. The centres W33, W47, W37 and W46 are also observed only in type Ib diamonds.

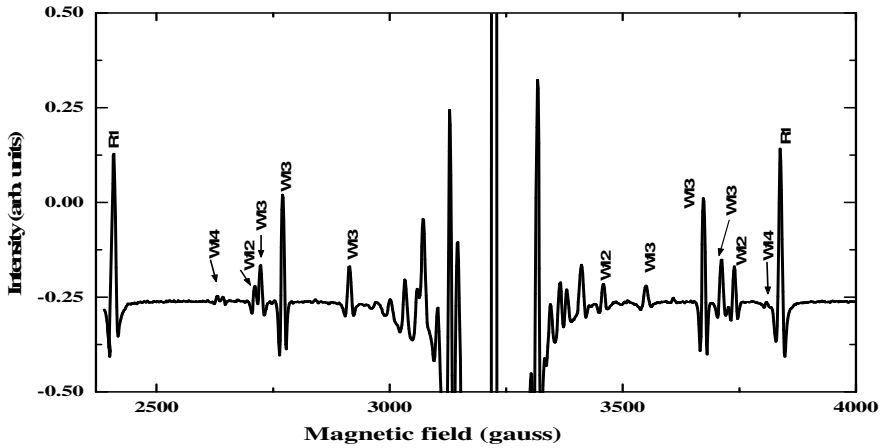

Figure 6.3: 2nd derivative EPR spectra for sample J4 before any annealing taken at room temperature. The Zeeman magnetic field is parallel to the <111>-crystal axis. In this direction, the **R2** peaks converge at the centre of the spectrum. However, most of the other centres are well resolved**.**

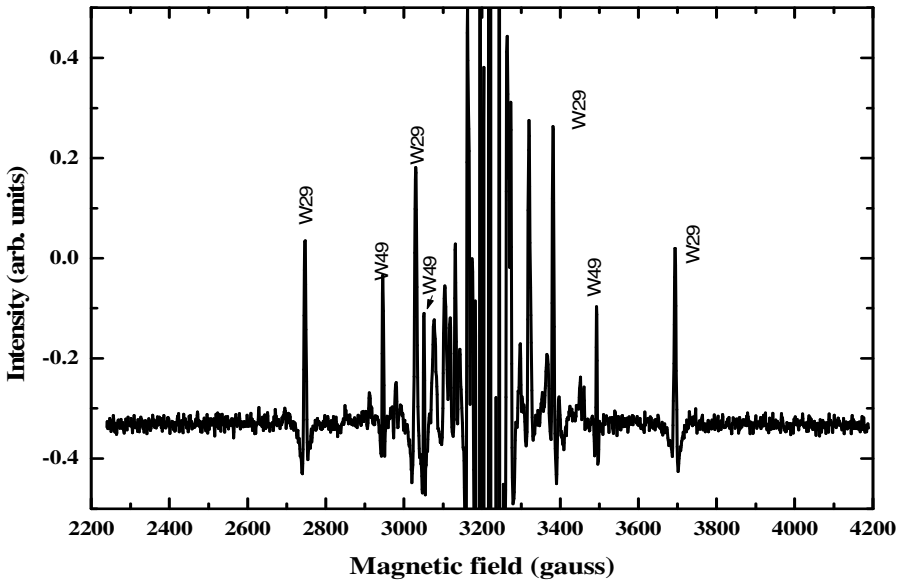

Figure 6.4: 2nd derivative EPR spectra for J4 isochronally annealed at 575 ^{o}C and measurements obtained at room temperature. The magnetic field is parallel to the <111>-crystal axis. The unlabelled lines in the centre are mainly the S1 and a-line.

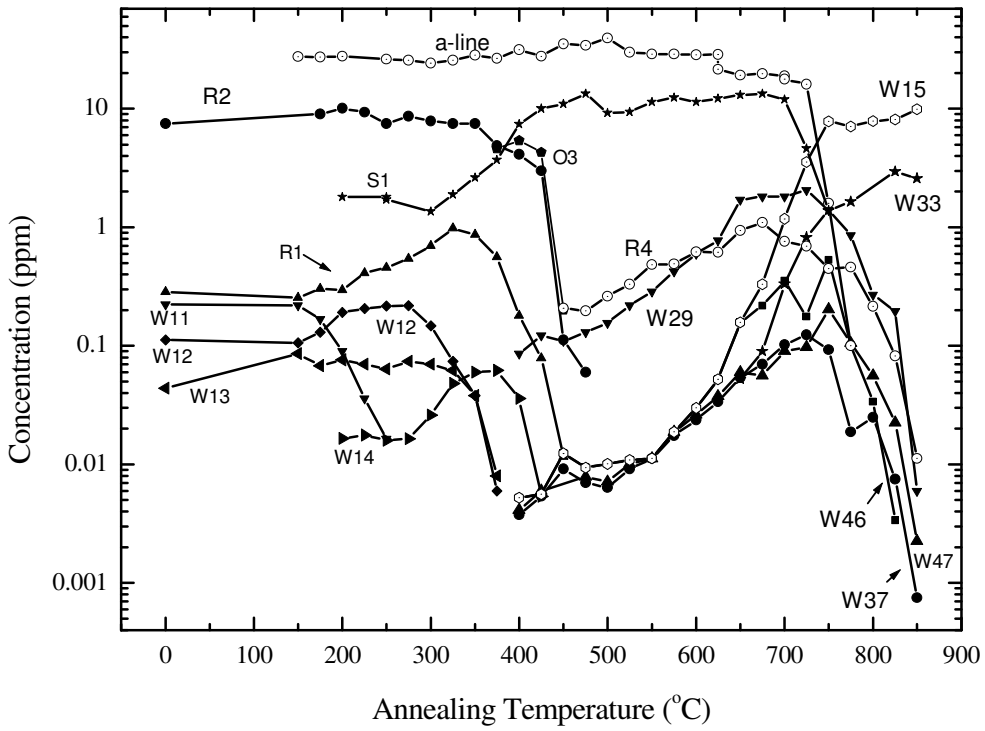

Figure 6.5: Annealing curves for a selection of defects observed in the neutron-irradiated synthetic diamond (sample J4).

The W11, W12, W13 and W14 EPR centres form a set of prominent centres that are observed after irradiation. Subsequently, W11 isochronally anneals out at around 250 °C whereas W12 and W13 do so at around 370 °C. W14 persists a little longer till 420 °C. A less studied centre named the W49 (G1d) was reasonably strong in the same temperature range and its linewidth is remarkably smaller in comparison with that of W29. All these centres will be discussed in later chapters.

In the middle of the spectra of Fig.6.4, there is a superposition of the S1 (negative vacancy) discussed in chapter 5 and the a-line discussed in chapter 7. The latter is the most dominant centre followed by the R1 and R2 centres.

The annealing curves of Figure 6.5 show that two annealing temperature ranges stand out clearly. The centres R1, R2 W11, W12, W13 and W14 fall in the lower annealing

temperature range of 0-400 ^{o}C whereas W15, W33, W37, W46 and W47 fall in the upper range starting from about 600 ^{o}C upwards. However, some centres such as R4/W6, W29, R3 and O3 are observed in a third range that straddles the other two.

CHAPTER SEVEN

THE EPR OF a-LINE IN TYPE Ib DIAMOND

7.1 Introduction

A very intense EPR line was observed at the centre of the spectrum of all our irradiated type Ib diamond samples and is referred to as the a-line. It was much stronger in the neutron-irradiated diamond sample J4, than in the 3 electron-irradiated samples (J1, J2 and J3). The study of the centre was difficult owing to the fact that it is situated in the g=2 region together with the S1 (negative vacancy) and other lines of half-integral effective spins.

Any centre with spin ½, no hyperfine splitting and little g-shift will contribute to the a-line. Furthermore, any centre with an even spin and tetrahedral, or near tetrahedral symmetry, will also give rise to lines in the central region of the spectrum. Hence the label a-line has been used to indicate any line or superposition of lines at g=2 region of the spectrum.

The a-line was first observed by Faulkner and Lomer (1962) in electron-irradiated diamonds and by Baldwin (1963) who showed that it consisted of at least three components of different linewidths and which appeared under different observation conditions. Dyer and du Preez (1965) found that the a-line in neutron-irradiated type I diamonds is stronger than the same line in type II diamonds.

It should be noted here that a line similar to the a-line is observed in some natural diamonds (particularly in plastic deformed stones) prior to irradiation. The composition of this line is not necessarily the same as in our irradiated samples.

The purpose of the present investigation of the a-line is to carry out isochronal annealing with a view to analysing the response of the centre to this treatment. The results presented

in this chapter show that the centre is extremely complex. The work is only expected to form a starting point for future investigation on the centre.

7.2 Results

7.2.1 Analysis of the a-line using Lorentzian lineshapes

In sample J4, the a-line was most prominent before annealing as shown in the second derivative EPR spectrum of Figure 6.3 of the last chapter. This is also shown as a first derivative EPR spectrum in Figure 7.2 following isochronal annealing to 150 ^{o}C. However, in samples J1, J2 and J3 (electron-irradiated type Ib set) the a-line, if present, was masked by the stronger spectra of the P1 centres.

While the lines of the spectra of most EPR centres are Lorentzian in shape, the a-line has the appearance of an exchange narrowed line. In an attempt to extract some information from this line it was fitted with a superposition of two or more Lorentzian lines of different widths and amplitudes. Before annealing, or after annealing at low temperature, the line was dominated by wide components, whereas narrower components became more important after annealing at higher temperatures. It was realized that the a-line could be 'resolved' into Lorentzian components in many different ways by changing the number of lines used in the superposition. To get a reasonable fit at least three lines were required in most cases.

One of the problems with a-line is that the effective spins of defects which contribute to it are not known. Another remark should be made at this point. First and higher derivates emphasize regions of higher slope more than regions where the slope varies more slowly. If a line has a width Δ then the amplitude of the absorption peak is Δ times larger than the amplitude of the first derivative. Therefore, components with larger linewidths will show up more prominently in lower derivate spectra. To get the best possible amplitude and width of the wider component, the first derivative experiment peaks were first integrated and fitted with three or four Lorentzian components. A fit with three components are shown in Figure 7.1.

Note that the wide line in Figure 7.1 has a slightly larger g-value than the narrower components. This shift of the wide line becomes smaller as the diamond is annealed at higher temperatures. While this technique will distinguish reliably between contributions if their linewidths are sufficiently different, it will be difficult or impossible if the linewidths are comparable, or become comparable during later annealing stages. It is evident that the a-line wings reach much farther than the range over which the first derivative was recorded. This fact is not obvious in the first derivative plot (Figure 7.2). The narrow component would be more prominent in the first derivative spectra.

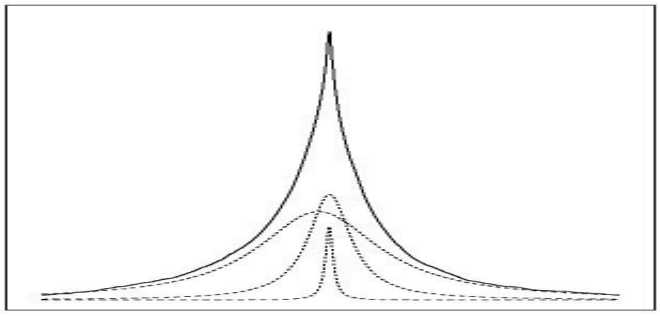

Figure 7.1: Integral of the first derivative peak (darker trace) of the a-line, after the annealing at 150 ^{o}C with B//<100>. The dotted and dashed line peaks shown are the Lorentzian components required to fit the experimental trace. The widths of the components are 53, 19 and 3 G.

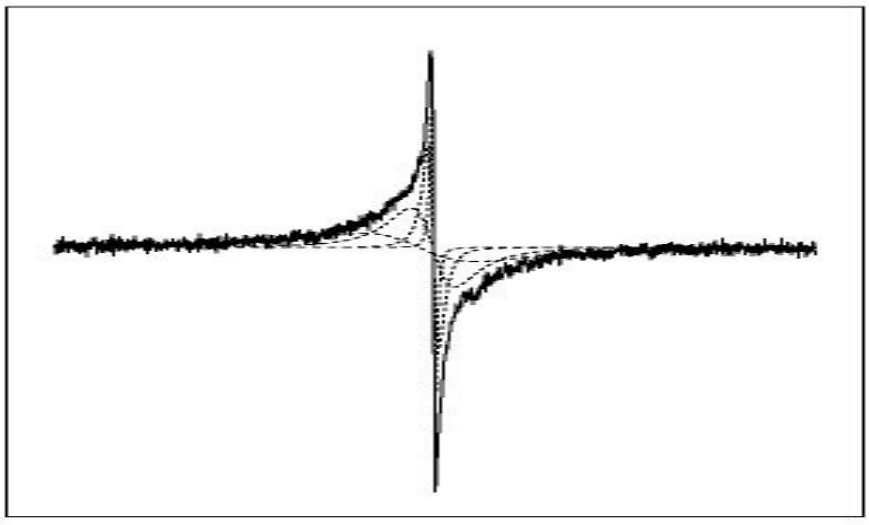

Figure 7.2: Lorentzian lines required to fit the first derivative of the a-line after isochronal annealing at 150 °C. Least squares fit produced in addition to the 53 G component 20, 4.9 and 1.6 G components.

To determine the concentration of defects which each component represents requires (i) that the integrals of the peaks in Figure 7.1, or the double integrals of the peaks in Figure 7.2 must be compared with that of a reference sample, and (ii) the effective spins of the defects. The integrals in (i) can be calculated from $A\Delta\pi$, for the absorption peaks, and $A'\Delta^2\pi$, for the first derivative peaks, where Δ and A are the half-width at half-height and amplitude, respectively, of the absorption peak, and A' is the amplitude of the first derivative. Since the spins of the defects are not known, one can at best determine a quantity C×S(S+1), where C is the concentration and S is the effective spin of the defect. The dependence of this quantity on the annealing temperature for the four components of the a-line are plotted in Figure 7.3.

7.2.2 Isochronal annealing

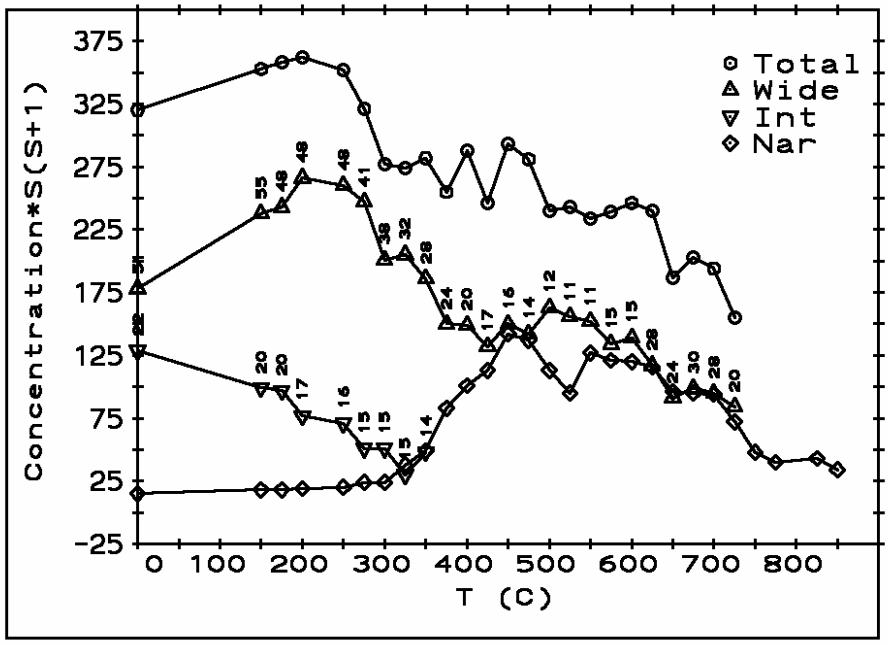

Figure 7.3: Linear plots of data derived from the a-line. Plotted is the concentration times S(S+1) for various components, and the sum of the concentration contributions. Also indicated are the widths of components with width larger than 5G. The widest component is represented by Δ, an intermediate component by ∇, and the sum of contributions with width less than 5G by the diamonds.

In Figure 7.3 we note that the contribution to C×S(S+1) for the widest component increases below 225 °C and then decreases as the anneal temperature is increased. The wider components produced during irradiation then anneals out, like R2 (and R1), around 400 °C. It looks as though another wide line makes its appearance above 400 °C. The intensity of the component of width around 5 G, stays low below 300 °C, but grows as the interstitial defects anneal out. All the contributions anneals out rapidly above 750 ºC

The annealing curves for the relatively well-documented defects R2, S1, R3, W29 and W15 are shown in Figure 7.4. If we assume that the effective spin of the a-line is one-half, then its concentration will be much greater than the concentrations of these centres.

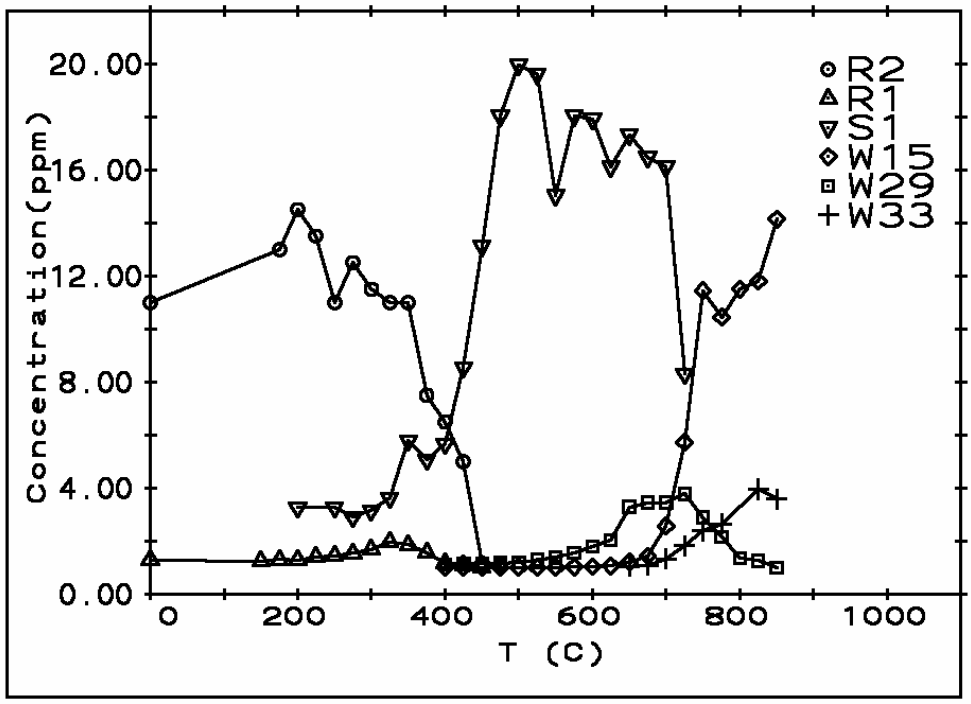

Figure 7.4: Concentration (ppm) versus annealing temperature for a few representative defects observed with a-line. The curve labelled S1 represents the concentration of the negative vacancy as determined from ^{13}C hyperfine lines.

From the annealing curves of Figures 7.3 and 7.4 it may be seen that the R2 and the broad component of the a-line exhibit a similarity in their annealing patterns. On the other hand,

the broad component of the a-line that grows above 550 ^{o}C anneals like the negative vacancy.

It should also be noted that the negative vacancy grows as the R2 anneals as shown in Figure 7.4. This agrees with the observation of Twitchen *et al.* (2001). Similarly, the vacancy associated centres like W15 and W33 grow as the negative vacancy anneals out. In Figure 7.5, a logarithmic plot is shown to emphasize the initial growth of W15 during annealing.

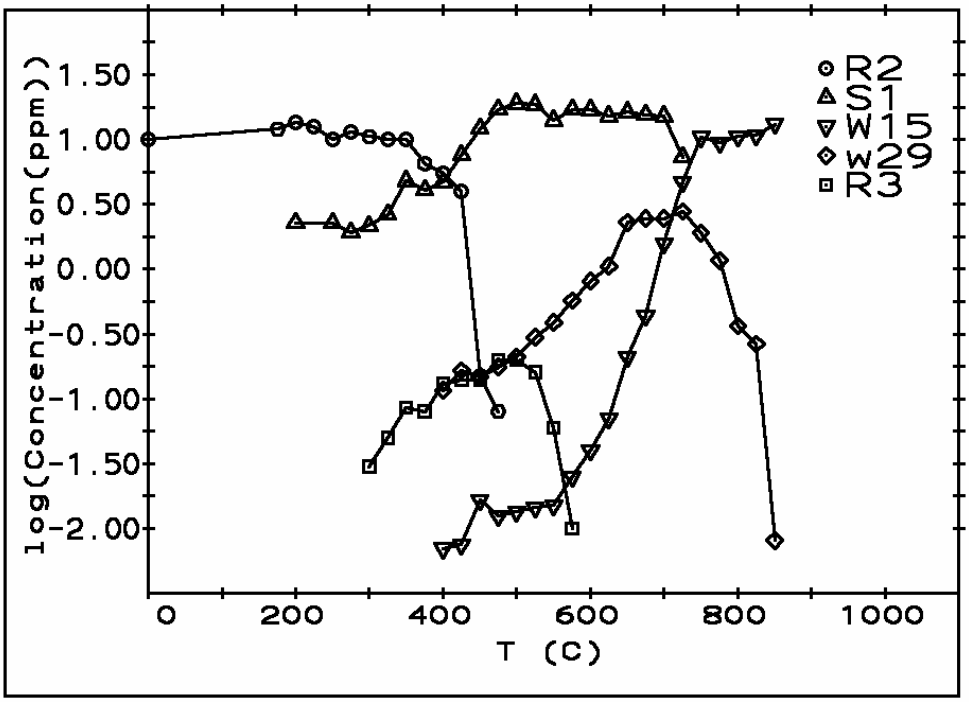

Figure 7.5: Logarithm of the concentration (ppm) versus annealing temperature (^{o}C) for a few representative defects observed with the a-line. Note that the log scale clearly shows some growth of the W15 centre in the temperature range 400- 600 ^{o}C.

7.3 Discussion

7.3.1 The nature of damage due to neutron irradiation

In an attempt to understand more about the a-line we consider the nature of neutron irradiation and assume that the damage it causes may be explained as follows. A 2 MeV

neutron imparts a maximum of about 280 keV on an atom of the diamond lattice (Budylin and Vorobev, 1964). The probability for the neutron colliding with another lattice atom may be very low. However, the dislodged carbon atom has a large kinetic energy and the cross-section of other atoms to a moving carbon atom is much larger.

The collision of the knock-on atoms and the stationary lattice atoms may be explained using the hard-sphere model (Kinchin and Pease, 1955; Bourgoin and Lannoo, 1983). Each knock-on atom shares its energy equally with the next atom that it displaces. The resulting avalanche effect continues until each moving atom has energy less than the threshold energy for atomic displacement i.e. about 35 eV (Bourgoin and Masarani, 1976).

Keating (1963) has shown that about 100 displaced carbon atoms result from each primary collision. The damaged region might be an elongated ellipsoid with the major axis along the path of the neutron. The total disorder in the damaged region is considerable as there may be interstitial atoms, vacancies, microcrystalline structure changes, free electrons, holes and several other abnormalities (Denning and Poindtexter, 1964). Other subsequent studies on radiation damage are available and some are discussed in the following paragraphs.

Biersack and Haggmark (1980) have developed a Monte Carlo computer program which simulates the slowing down and scattering of energetic ions in amorphous targets. The package was developed for determining ion range and damage contributions as well as angular and energy distributions; it is possible to assess accurately both low and high energy problems with high precision using their single simulation program. Another very well tested computer program TRIM (Transport of Ions in Matter) can predict very accurately the distribution of the knock-on atoms produced by heavy particles and the trail of damage that they leave (Ziegler, 1985).

More recent irradiation damage studies in diamond have been performed by Campbell *et al.* (2002) who investigated the mechanism for damage caused by electrons and gamma radiation. Campbell *et al.* (2002) used a combination of theoretical modelling and optical and EPR spectroscopy to study the kinetics of damage creation and the subsequent recombination of closely paired vacancies and self-interstitials. They also found that the annealing of the defects as the irradiation took place reduced the damage observed which was strongly dependent on both temperature and radiation flux.

The a-line and an extensively damaged region of the lattice

We assume that the a-line has its origins in the regions of extensive damage along the track of the neutrons causing a large density of dangling bonds that interact to give rise to systems of different spins. The systems with odd number of spins and large zero-field splitting will have a component in the g=2 region. The large density also may then be responsible for the wide components of the a-line. The narrower components, by contrast, are due to more isolated and hence less dense spin systems.

Due to spatial distribution of zero-field splitting axis, there will be an averaging effect from the fluctuating exchange interaction between the spins. This probably would help reduce the linewidths of the spectra for otherwise it would be difficult to observe. The narrow components probably arise from the regions in which the density of dangling bonds is less.

During annealing, lattice repair (or partial repair) will probably take place in the regions of extensive damage - *a local phenomenon* - and we will also expect repair in the rest of the diamond. Following the repair in the extensively damaged regions, it does not look as if a significant number of R2 centres are formed – little or no increase in R2 is observed during the entire anneal history. The increase in the number of isolated S1 (around 400 ^{o}C) is small compared to changes in the number of defects contributing to the a-line in the same temperature region -not many isolated S1's are formed during repair in extensively damaged regions. This does not mean that the extensively damaged regions are fully restored to give a perfect lattice as the wide line components are observed above 400 ^{o}C.

In an attempt to explain the results we put forward the following theory. As the annealing temperature is raised, the damage is repaired most readily in the regions with the highest density of defects. The widest component of the a-line starts to decrease in intensity and the narrow line shows a growth as may be seen in Figure 7.4. The change in linewidth as annealing temperatures are raised for the two broader lines is probably a result of damage repair in the extensively damaged regions. Assuming that this is the case, the dipole-dipole broadening begins to reduce as annealing progresses leading to the observed reduction in linewidth.

After annealing at 450 °C we observed a centre of similar linewidth to the broadest component of the a-line. Though the origin of the centre is still unknown, we suggest that it is in the repaired region of the extensively damaged part of the crystal. Most probably, there will be vacancy structures formed as the damaged regions are partially repaired. This suggestion derives some support from the fact that these structures anneal out when the vacancies become mobile.

The amplitude of an EPR line is proportional to S(S+1) and to determine the concentration of the defect we need to know its electronic spin. Since we did not know with certainty what defects give rise to the a-line, we could not really calculate its concentration. However, we could determine the relative concentrations and this was done for the a-line.

7.4 Conclusion and suggestions for further work

From the results obtained we note that the a-line consists of centres that have components in the g=2 region of the spectra. These will include the negative vacancy and other defects that have half-integral spin. Hence the strong a-line in sample J4 (neutron-irradiated diamond) suggests trapping of the electrons by the various defects in the lattice. Indeed the absence of the P1 centre in J4 is an indication that the isolated nitrogen atoms have been ionized and thus rendered non-paramagnetic. This concurs with the findings of others (Lawson *et al.*, 1998).

Owing to the complex nature of the a-line, further measurements should be made in order to obtain a better understanding of the defect. Among additional steps include:

- investigating damage centres in a suite of all types of diamonds irradiated with both electrons and neutrons with specific known doses.

- using diamonds with different but known impurity concentrations.

- determining linewidths with the external magnetic field parallel to all 3 directions, i.e <111>, <110> and <100> directions to establish whether damage is preferentially made and provide evidence for regions of extensive damage.

CHAPTER EIGHT

W33, W46, W37 AND W47 EPR CENTRES

8.1 Introduction

The annealing of irradiated type Ib diamond above 615 ^{o}C greatly enhances the intensities of a number of EPR centres *viz* W33, W46, W37 and W47. In this temperature range, the vacancies are mobile and this suggests that the centres are vacancy-related. The symmetry of the centres as deduced from the angular dependence of the spectra recorded in this work shows a close similarity to that of the W15 EPR centre (briefly discussed in chapter 5). Accordingly, nitrogen is expected to play an important role in the formation of these centres.

The aim of studying the centres in the present work has been to obtain their spin Hamiltonian parameters. Reference to some of these centres based on existing literature has been given in a review by Ammerlaan (1988). In the review, however, only the outer transition lines were used to determine the angular dependence of these centres owing to the complexity of their spectra. It was assumed that for all these centres the effective spin S=1. Accordingly only the symmetries were reported.

The present work on these centres has been carried out in order to determine their spin Hamiltonian parameters and effective spins.

8.2 Experimental results

8.2.1 The spectra and the spin Hamiltonian parameters

The W33, W46, W37 and W47 were first observed after annealing J4 to 650 ^{o}C. At this annealing temperature for example, the W15 started to be observable giving the first indication that these centres are most likely vacancy-related. However, long before we

observed them through $\Delta m_s = 1$ transitions, W37, W46 and W47 centres were detectable by means of the $\Delta m_s = 2$ transitions after isochronal annealing at 625 °C. The recording shown in Figure 8.1 was made after annealing to 675 °C following which the signals for the centres had grown significantly in strength.

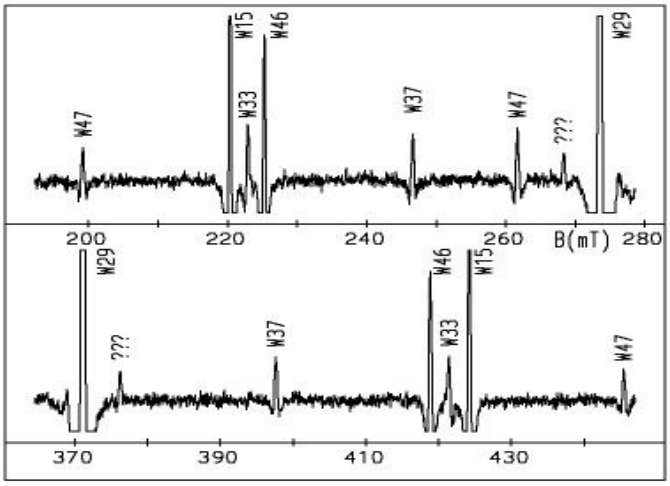

Figure 8.1: Outer regions for EPR spectra following annealing at 675 ºC. The upper spectra belong to the region for which g<2 whereas the lower belong to the region for which g>2. The central region of the spectra, i.e. g=2 region is omitted. The Zeeman magnetic field was parallel to <111>-direction**.**

All the lines in Figure 8.1, except for the inner lines of W47, are due to $\Delta m_s = \pm 1$ transitions in the three {110} planes in which the magnetic field is rotated and that make an equal angle with a common <111> axis closest to the principal axes of the defects. The rest of the transitions in these planes, if any (depending on the spin S), and all transitions due to defects in the other planes, as well as spectra due to other defects with small or no zero-field splitting occurs in the region between the two spectra in Figure 8.2. Consequently, the spectra in this region consist of many poorly resolved lines, which make identification and association of the lines with specific transitions and defects, at any one anneal stage, almost impossible. Another important set of directions consists of the <110> directions for which the situation is even worse as more lines are cramped into a smaller scan range. It required comparison of spectra and angular plots at several annealing stages to correctly identify lines with specific transitions of the defects. Although information about the symmetry of the defects can be extracted at early annealing stages from angular plots, the spin and hence the spin Hamiltonian parameters can be extracted only at later stages.

At this point, it is appropriate to emphasize the importance of the <110>-directions. In general, a measurement must be made with magnetic field parallel to the axis of symmetry of the centre, to obtain the D-value for a centre. To obtain the E-value, one needs to make at least two measurements with the magnetic field in a direction perpendicular to the symmetry axis. For the defects investigated in this chapter, one of the lesser tensor-axes, *x*-axis or axis 1, is along or close to a <110> axis. Measurements along this direction yield valuable information about the magnitudes and sign of the E-term once the observed lines are properly associated with transitions appropriate to the defects.

8.2.2 The W37 and W47 EPR centres

To determine angular dependence of the spectra for these centres, the Zeeman magnetic field and the corresponding frequency measurements for $\Delta m_s = 1$ transitions were carried out in the usual manner (Fig.8.1). The angular variation of the peaks for W37 and W47 are given in Figures 8.2 and 8.3, respectively. Least-squares-fitting to the spin Hamiltonian $H = \beta \hat{S}.\underline{g}.\hat{B} + \hat{S}.\underline{D}.\hat{S}$ first given in chapter 3 was carried out. And the resulting zero field tensor parameters are given in Table 8.1.

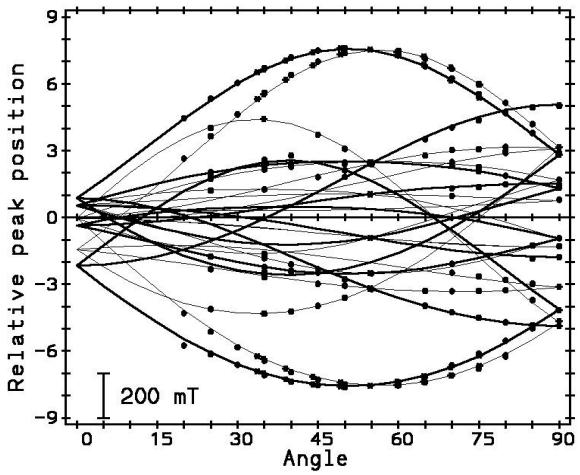

Figure 8.2: Angular variation of the spectra for the W37 as the magnetic field is rotated in a <110>-plane from [100] to [110]-crystallographic directions. The solid lies represent least squares fit to the data, the (*), accurate set of experimental data (used for fitting) and (o), a less accurate set (not suitable for fitting).

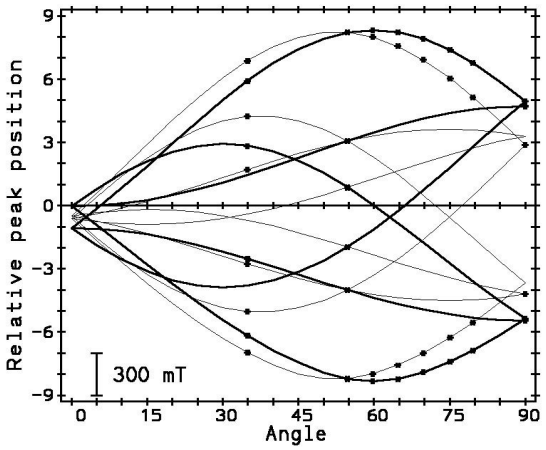

Figure 8.3: Angular variation of the spectra for the W47 as the magnetic field is rotated in the {110}-plane from <100> to <110>-crystallographic directions. The solid lines represent least squares fit to the data, the stars (*) relatively more accurate set of data (used for fitting) and circles (o) a less accurate set of data (not suitable for fitting).

Following the fitting, a value for the effective spin S =2 was found for the W37 centre. To confirm this high value of S, measurements were made for $\Delta m_s = \pm 3$ transitions. It was already known that a centre with S=3/2 had a peak in this region (the W29 centre). The observation of an additional line in the spectrum as shown in Figure 8.4 enabled conclusive identification of the W37 centre which is one of a few centres in diamond with effective spin S=2.

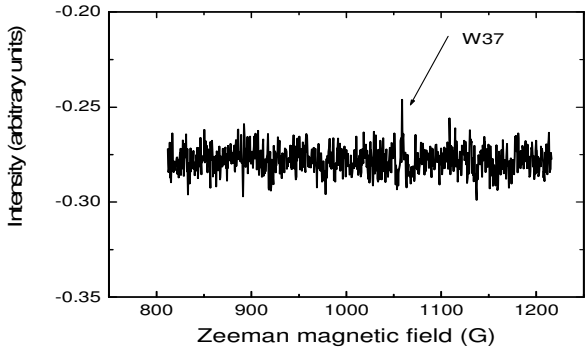

Figure 8.4: 1st derivative absorption peaks obtained in the $\Delta m_s = \pm 3$ region with magnetic field parallel to <111>-crystallographic direction. Measurements were obtained with neutron-irradiated type Ib diamond after isochronal annealing at 775 °C.

Table 8.1: The components of the zero-field splitting parameter D for W37 and W47 centres in irradiated diamond. The g-value for both centres is 2.0025(2).

□	S	D_1(MHz)	D_2(MHz)	D_3(MHz)	θ	ϕ	ψ
W37	2	-311	472	-162	39.4	0	0
W47	1	-1401	2333	-933	30.15	0	0

8.2.3 The W33 centre

Figure 8.5 shows the angular dependence of the fine structure of the W33 centre. The centre has the principal axis of its zero-field tensor 33.5º from a <110>-direction, which is close to a <111>-direction (which in turn is 35.26º from a <110> -crystallographic direction).

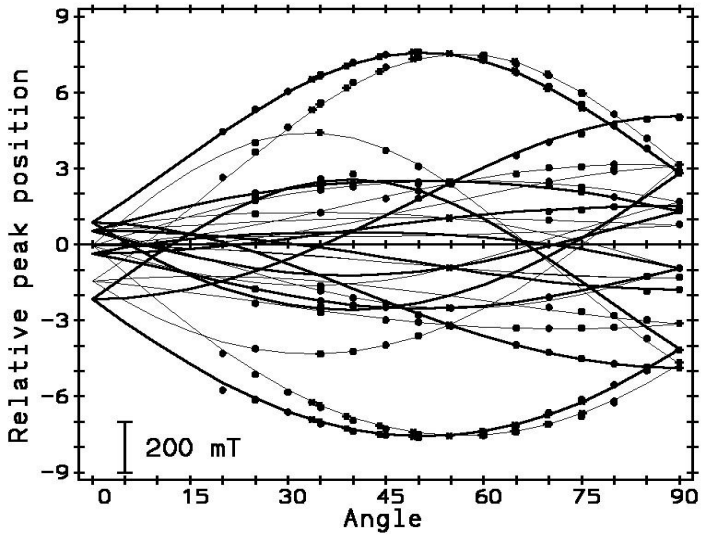

Figure 8.5: Angular variation of W33 centre EPR spectra as the magnetic field is rotated in a {110}-plane from <100>- to <110>-crystallographic directions. The stars (*) represent the experimental data whereas the solid line shows the least squares fit.

Some of the lines of W33 show a small splitting in some directions. An example of this can be seen in Figure 8.6.

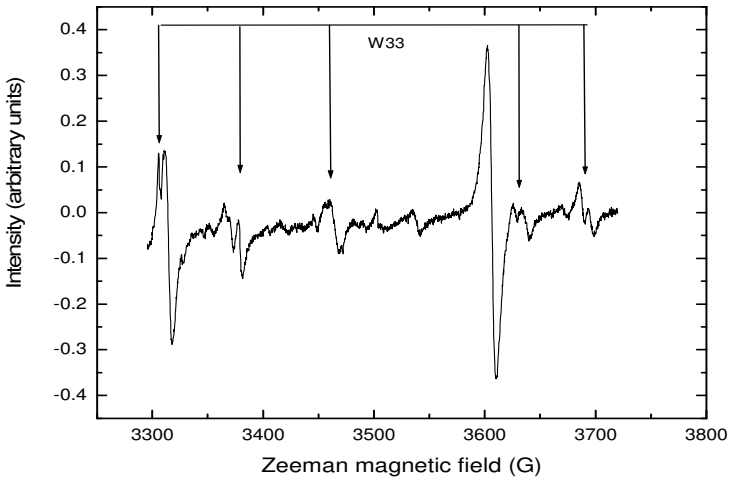

Figure 8.6: EPR spectra of the W33 centre with the Zeeman magnetic field oriented 65 ^{o} from <100> in a {110}-plane.

If the splitting is due to hyperfine interaction, some structure should be observed in the Δm_s =2 transitions because in this region the spectra are not sensitive to D-tensor changes. However, no hyperfine structure was observed. Some experimental lines do not show the calculated splitting. While the W15 centre exhibited resolved hyperfine interaction of 0.8 G, there was no resolved hyperfine structure for the W33 centre. Its linewidth of 1.5 G is considerably smaller than that of the W15 centre which is 2.5 G. We think that the splitting of the W33 spectra suggests a non-axial D-tensor for the W33 centre. It means that angle ϕ and/or ψ in Table 8.2 is not zero. These angles could not be determined. The other spin Hamiltonian parameters for the centre are given in Table 8.2

Table 8.2: The components of the zero-field splitting parameter D for W33 centre in irradiated diamond. The g-value for the centre is 2.0025(2).

S	D_1(MHz)	D_2(MHz)	D_3(MHz)	θ	ϕ	ψ
1	-1155	1866	-711	33.5	?	?

8.2.4 The W46 EPR centre

The angular dependence for the spectra for the W46 centre is shown in Fig 8.7.

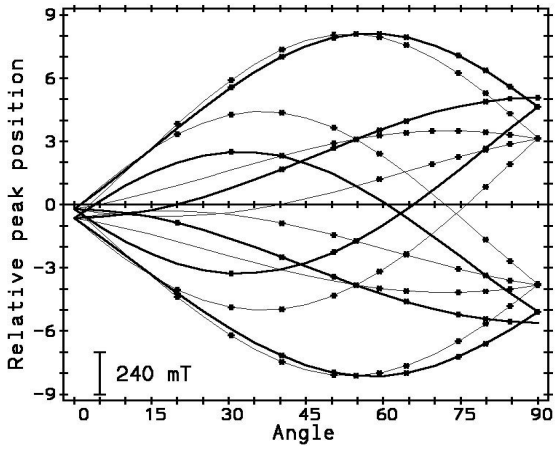

Figure 8.7: Angular variation of W46 centre EPR spectra as the magnetic field is rotated in a {110}-plane from <100>- to <110>-crystallographic directions. The stars (*) indicate experimental data values whereas the solid line is the least squares fit to the data.

The resulting spin Hamiltonian parameters are given in Table 8.3.

Table 8.3: The components of the zero-field splitting parameter D for W46 centre in irradiated diamond. The g-value for the centre is 2.0025(2)

S	D_1(MHz)	D_2(MHz)	D_3(MHz)	θ	ϕ	ψ
1	-1187	1824	-639	32.3	0	0

From Figure 8.7, it is evident that the W46 centre also has its zero-field tensor axes very close to a <111>-direction which is 32.3º from a <110> -crystallographic direction.

8.2.5 Annealing curves

The annealing curves for W15, W33, W37, W46 and W47 are given in Figure 8.8. Note that W46 is the first to anneal out. W37 and W47 then anneal out together at a slightly higher temperature. Although it is not shown in Figure 8.8, W33 will anneal out at around 1000 °C whereas W15 will persist up to much higher temperatures.

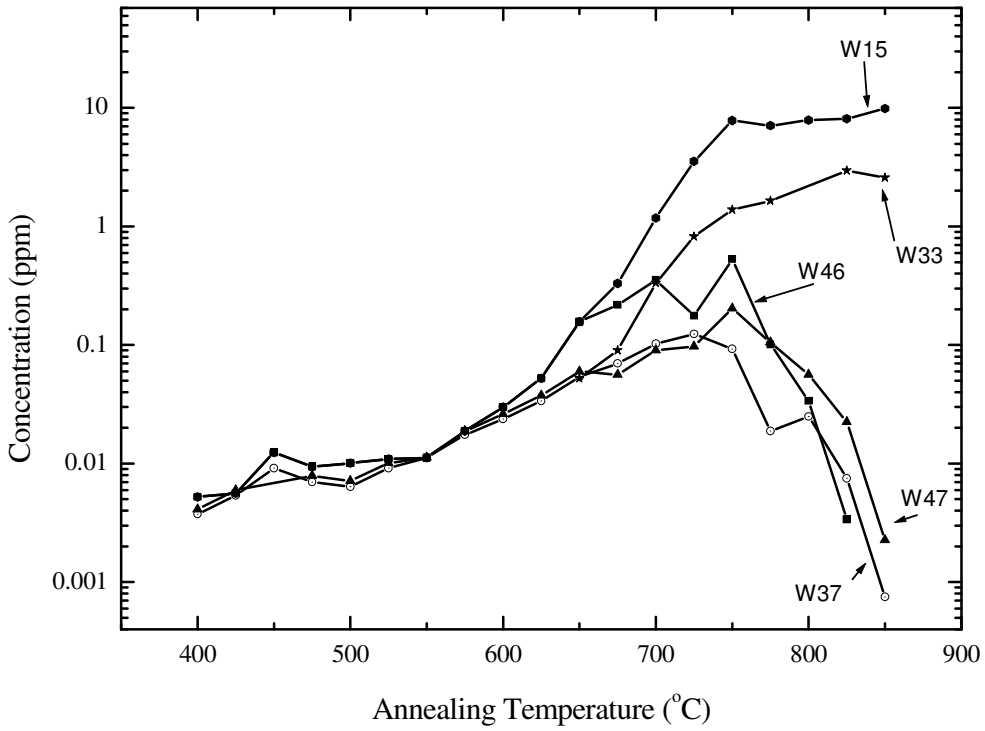

Figure 8.8: Annealing curves for W33, W37, W46 and W47 EPR centres in diamond.

8.3 Discussion

It is known that the major principle axis of W15 is exactly along <111> symmetry axes and it has $E = 0$, (Loubser and van Wyk, 1977; Loubser and van Wyk, 1978). The W33, W46, W37, and W47 centres all have their major principal axes not far from <111>-directions. The W37 and W47 centres (as well as W15) have one of their other principal axes exactly along a <110>-direction, whereas this axis appears to be tilted from the <110>-direction for the W33. We conclude from this that the W46, W37, W46, and W33 must all be centres similar to W15; they must all involve nitrogen plus a vacancy.

It should be noted in Figure 8.8 that all these centres grow slowly at roughly the same rates, and also have much the same concentrations during the initial anneal stages. This is taken to indicate that the concentrations at 400 °C is nearly the concentrations produced under the beam, and also reflects the spatial distribution of vacancies near a nitrogen. The concentration of W15 gives the number of vacancies created in the nearest neighbour

position of nitrogen, whereas the other concentrations give the number of vacancies at other positions in the immediate vicinity of the nitrogen. If we assume that these centres anneal out when the vacancies move to the nitrogen (to form W15), we would expect that the defects with vacancies closest to the nitrogen anneal out first, followed by others with vacancies further away. Since W46 anneals out first, we expect that its vacancy (after W15) is closest to the nitrogen.

The above considerations led us to propose the model shown in Figure 8.9 for W46.

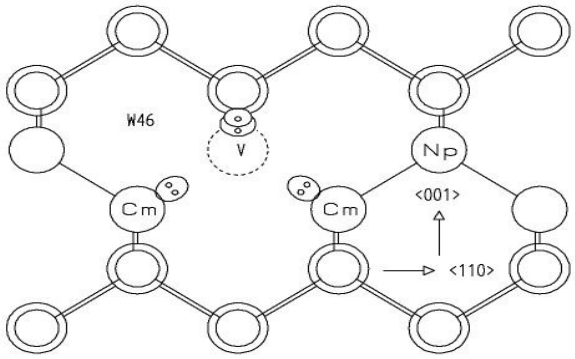

Figure 8.9: A proposed model for W46 EPR centre in diamond. The plane of the paper coincides with the (110)-plane containing the vacancy. The smaller and larger of the concentric circles represent atoms in the {110}-planes below and above this plane, respectively.

Like W15 it is expected that W46, as is the case for all the defects being discussed in this chapter, would be negatively charged. It is for this reason that two of the four dangling bonds (on carbons indicated with Cm) around the vacancy are indicated with a pair of electrons. These electrons are obviously not localized on particular carbons, but will cycle between all the bonds. It is however expected that the extra electron on the carbon closest to the nitrogen would be localized a larger fraction of the time on this carbon due to the interaction (electrostatic) with the nitrogen, labelled Np to indicate that it is positively charged. This would give rise to a defect with rhombic symmetry with symmetry axis close to a <111>-direction (Cm nearest the nitrogen to the vacancy) but tilted slightly towards the <110> direction. This is consistent with the angle θ=32.3º given in Table 8.3.

We propose that the W37 and W47 centres are due to different spin states of the same defect. A system of four unpaired electrons can give rise to states with S=2, 1 and 0. The

W37 could be due to the S=2 state and W47 due to one of the S=1 states. Some support for this comes from the fact that the two spectra anneal out at the same temperature.

The model that we have proposed is shown in Figure 8.10. Since W37 and W47 are marginally more stable the vacancy is one site further from the nitrogen than in W46. Like W46 they have rhombic symmetry which means that the nitrogen must be in the same (110)-plane as the vacancy. The separation between the nitrogen and vacancy must also be larger so that there is less interaction between the vacancy electrons and the nitrogen electrons. We propose that the 'extra' electron is localized on the carbon adjacent to the nitrogen as shown in Figure 8.10 – to have a situation much like we have for the A-centre.

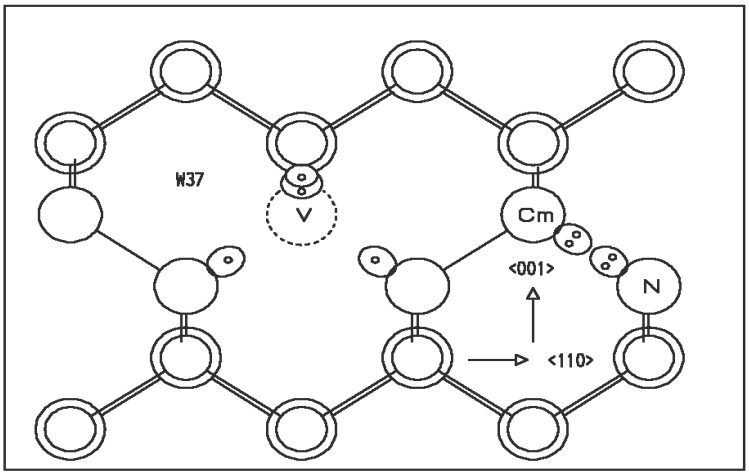

Figure 8.10: Proposed model for the W37 and W47 centres.

Due to the negative charge on Cm the vacancy electron on the carbon closest to Cm may spend more of its time on the other three vacancy carbons. This will again give rise to defect with near <111> symmetry. We could get some feel for this situation by considering the following very simplistic model. If at any instant two of the four vacancy electrons are paired, one carbon then there will be dipolar interaction between the other two unpaired electrons. With time, the pair will move from carbon to carbon and the direction of the dipolar interactions will cycle between the <110>directions defined by the carbon pairs around the vacancy. It will however be found more frequently in the plane opposite the vacancy carbon nearest to Cm. With this approach one can also show that the zero-field splitting for the S=2 state should be much smaller than for the S=1 state.

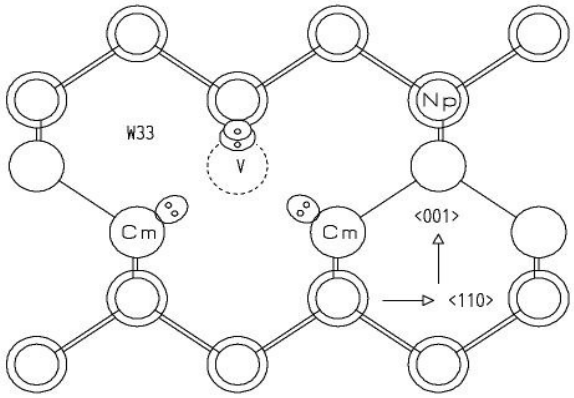

Figure 8.11: Proposed model for W33 centre

The fact that the EPR spectra indicates that W33 has symmetry lower than rhombic suggest that the nitrogen and vacancy may not be in the same (110) plane. At the same time the nitrogen-vacancy separation must not be larger than that for W46, W37/47. A model consistent with this is shown in Figure 8.11. It is not understood why the W33 should be relatively more stable than the other centres.

8.4 Conclusion

The structural models for these centres have been proposed based on the annealing behaviour and the spin Hamiltonian parameters but any firm assignments must wait for much more detailed structural calculations and additional experimental data. The centres W37, W46 and W47 all have rhombic symmetry with the vacancy and the nitrogen both lying in the same (110) plane. The W33 has non-rhombic symmetry suggesting that the nitrogen and the vacancy are not in the same (110)-plane. Supporting experimental evidence is a splitting observed in the EPR spectra of this centre (Figure 8.6). However, it is not clear why the centre is the most stable of all the centres discussed in this chapter.

The annealing data suggests that the W46 anneals out first. The proposed model supports this finding as it shows the vacancy for this centre is relatively closer to the nitrogen than in the case of the structures of the other 3.

The data also suggest that the W37 and W47 centres are due to different spin states of the same defect. The W37 could be due to the S=2 state and W47 due to one of the S=1 states.

CHAPTER NINE

W11, W12, W13 AND W14 EPR CENTRES

9.1 Introduction

EPR centres named W11, W12 W13 and W14 following their first identification at the University of the Witwatersrand, are formed in electron or neutron-irradiated type Ib diamond. We will henceforth refer to them as the W11-W14 centres in this chapter.
Whereas the interstitial related centres R1 and R2 are formed in all diamond types after irradiation and before any heat treatment the W11-W14 centres are observed only in irradiated type Ib diamond before annealing.

The spin Hamiltonian parameters have been obtain previously by van Wyk (1994) and are reproduced in Table 9.1 below.

Table 9.1: Zero-field interaction parameters D and E for the W11-W14 centre (van Wyk, (1994). The angles θ and ψ measure the position of the symmetry axis from a <110>-direction and its tilt out of the {110}-plane, respectively. T_o is the temperature at which the centres anneal out. All the centres have S=3/2

	W11	W12	W13	W14
D(G)	263	258	268	290
E(G)	-7	32	20	-27
$\theta(^\circ)$	45	39	48	37
$\psi(^\circ)$	-3	-2	0	0
$T_0(^\circ C)$	255	375	375	525

The relative intensities of these centres recorded in sample J3 may be seen in Figure 9.1 which shows a second derivative EPR spectrum obtained at room temperature before any annealing when the magnetic field was in the <111>-direction. The interstitial-related

centre R1 is also shown. The W11 centre is the most intense while the W12 centre is the weakest.

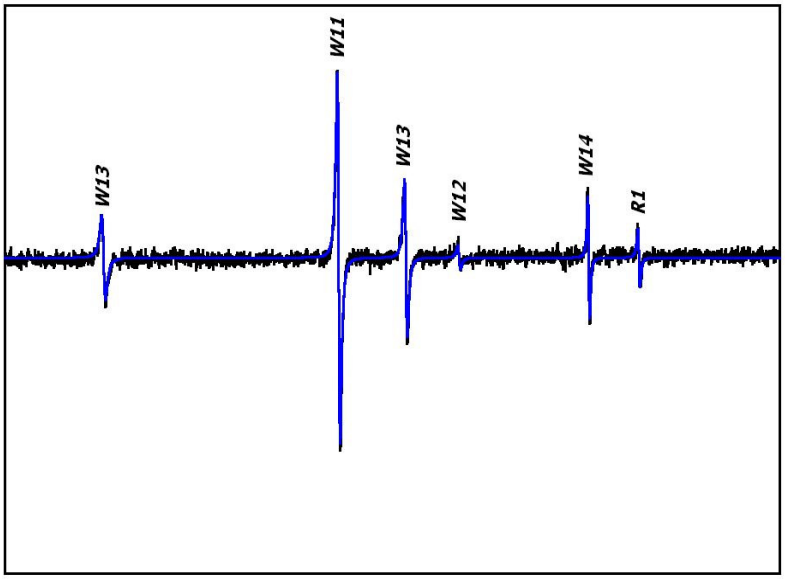

Figure 9.1: 1st derivative spectra of W11-W14 centres in sample J3 taken before any annealing at room temperature with the Zeeman magnetic field in the <111>-direction in g>2 region.

In probably the earliest attempt at the determination of the structures of these centres, van Wyk (1994) used theoretical considerations to propose three models. In the first model, he proposed that an electron was captured by a neutral vacancy to create a negative vacancy. However, the negative vacancy would have to be perturbed possibly by a nearby nitrogen atom in order to lower the T_d symmetry and allow zero-field splitting. However, this model fails to explain the relatively low annealing temperature for these centres if they do not involve interstitials. In addition, the value of the zero-field splitting tensor D based on dipolar coupling is smaller than expected.

In the second model van Wyk (1994) postulated that one or more interstitial atoms could be trapped near a vacancy. However, it was not clear how the arrangement would be stable and why it did not occur in type Ia diamonds. In the third model van Wyk proposed that $C_i^- - (N-C)^+$ pair could be formed involving a charge transfer between an interstitial carbon and an [N-C]^o defect. In such an arrangement the unbounded C_i^- would be

expected to have the correct $2p^3$ valence state and rise to a ^4S state with $S = \frac{3}{2}$. However, the models do not explain the observed symmetries for these centres.

Lowther and van Wyk (1994) subsequently proposed that the large zero-field splitting interaction associated with these centres could be attributed to a distorted-negative vacancy model in which the negative vacancy molecular states were mixed through spin-orbit interaction.

New work on the annealing behaviour of the linewidths and concentrations for the W11-W14 centres is discussed in this chapter. In addition, it is verified that the electron effective spin is 3/2.

Though not studied in any detail, another set of EPR centres observed after irradiation and no annealing in sample J4 were the A1, A2, and A3 centres first observed at the University of New York at Albany. All the three centres have an effective spin S=1 (Kim and Watkins, 1971; Kim *et al.,* 1972).

9.2 Experimental

The specifications of the samples used in this study and the annealing curves for the centres observed have been given in chapter 6. The peak-to-peak linewidths for the first derivative spectra were determined as accurately as possible by ensuring that appropriately low strengths of magnetic field modulation amplitude were used to avoid line broadening. As a rule, it was safe to keep the microwave modulation amplitude at about one-fifth of the linewidth of the EPR signal. However, in other measurements where the accuracy of the linewidth was not of prime concern, it was usually necessary to use higher values than this rule required. This was necessary since we were dealing with very weak lines. In some cases, the modulation amplitude was kept at 1G for most of the measurements that were undertaken. Such measurements included the angular variation of resonance fields needed to determine the spin Hamiltonian parameters.

As explained in chapter 4, relative rather than absolute determinations of concentration were preferred. Doubly-integrated first derivative EPR absorption spectra were compared

with those of a well-calibrated reference sample. The concentrations were in the order of about 1×10^{19} spins per gram.

9.3 Results

9.3.1 Annealing measurements

Figure 9.1 shows first derivative EPR spectra for W11-W14 centres before any annealing in sample J3. It may be seen that the W11 centre was the most abundant whereas the W12 and W14 were the weakest of these centres.

Following annealing up to 750 ^{o}C the curves shown in Figure 9.2, below were obtained. Figure 9.2 (a) gives logarithmic plots of the annealing curves for the centres whereas the linear plots are given in Figure 9.2 (b).

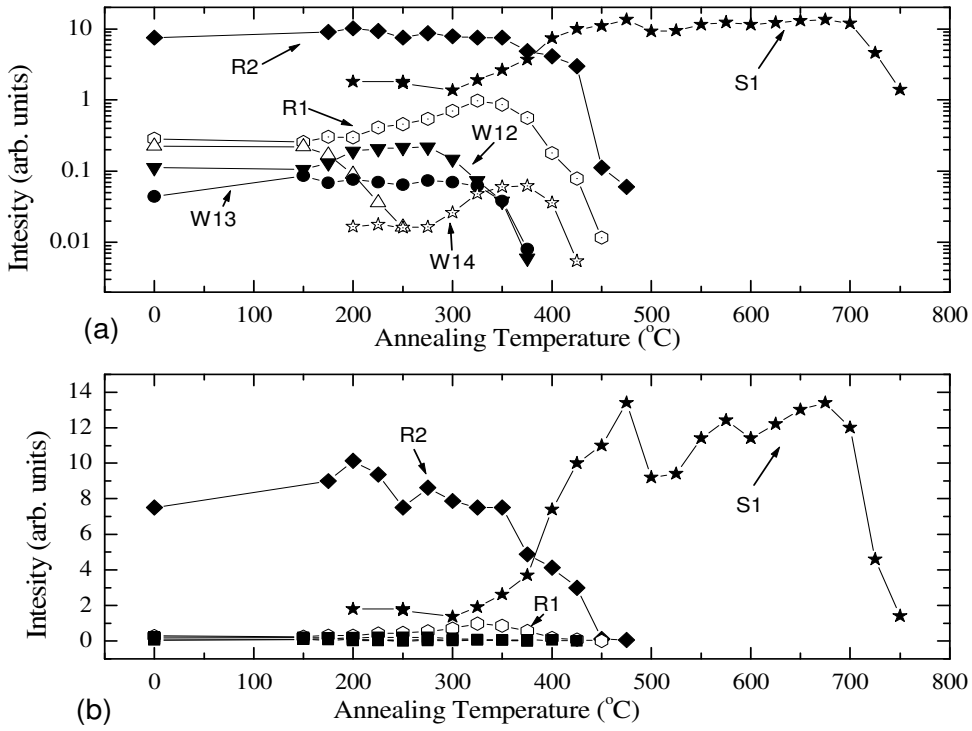

Figure 9.2: Signal intensity versus annealing temperature for the W11-W14 centres. The annealing curves for the S1 as well as the interstitial centres R1 and R2 have also been included. (a) Log graph; (b) linear graph.

9.3.2 Linewidths

The linewidth of the W11 centre from measurements on samples J1, J2 and J3 showed a linear variation with concentration as shown in Figure 9.3(a). There is a clear increase in linewidth in direct proportion to the concentration of the P1 or a-line centres.

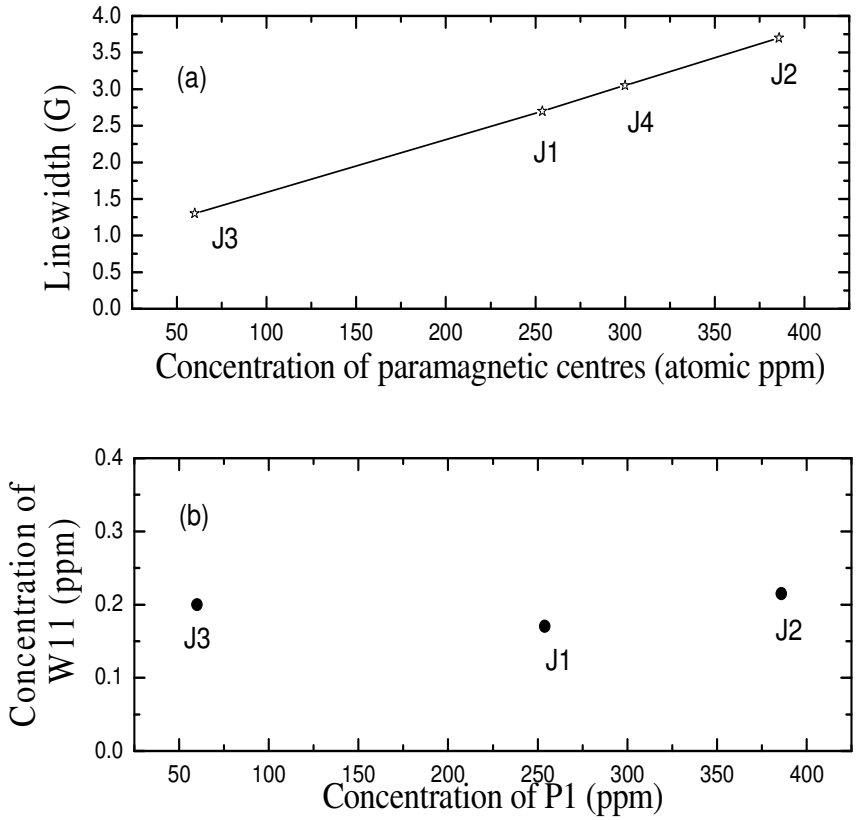

Figure 9.3: (a) Linewidth of W11 versus concentration of paramagnetic centres in all the 4 samples (J1, J2, J3 and J4). (b) The W11 concentration versus P1 concentration for the 3 electron -irradiated samples (J1, J2 andJ3).

9.3.3 Concentration measurements

The concentration measurements for the W11-W14 centres in sample J3 are given in Table 9.2 after irradiation but before any annealing. The measurements were performed on spectra taken with the magnetic field parallel to the <111>-direction. Due to the relatively weak intensities, these measurements were not easy. However, the spectra of Figure 9.1

were used to obtain these concentrations which ranged from 870(130) ppb (W11) to 39(12) ppb (W12) as indicated in Table 9.2.

Owing to the use of a well-calibrated standard to obtain the concentrations, these values are reliable. The procedure for determining concentrations has been given in chapters 4 and 7.

Table 9.2: Concentrations (ppb) and linewidths of W11-W14 centres as measured in sample J3 after irradiation but before any annealing with magnetic field in <111> direction and at room temperature. A value for R1 is also given for comparison.

Centre	W11	W12	W13	W14	R1
Concentration (ppb)	870(130)	39(12)	415(130)	127(28)	16(3)
Linewidth (G)	1.3(2)	1.1(2)	1.2(2)	0.92(2)	0.16(1)

A comparison of the intensities of the centres in samples J1 (255 ppm P1) and J3 (100 ppm with those of the P1 centre, showed that in sample J1 the intensity of the lines was too low for any observation of the W14, R1 or W12 centres. It appears that there is a relationship between these centres and the P1 centres which probably suggests an involvement of the nitrogen in their formation.

9.3.4 Half field ($\Delta m_S = 2$) and third field ($\Delta m_s = 3$) transitions

Another new result of the present investigation is the verification of the effective spin for the W11-W14 centres using the forbidden transitions i.e. half-field ($\Delta m_S = 2$) transitions and third-field ($\Delta m_s = 3$) transitions. Based on the parameters for the best fit to the data, it was possible to identify the centres in the half-field region. In Figures 9.4-9.6 dotted lines show the calculated spectra while the full lines denote experimental spectra.

Tucker (1995), carried out low temperature thermal depopulation studies in order to unambiguously determine the effective spin of W12 and W13 as S=3/2. His results suggested also that the W11 is an excited state. He observed complex behaviour for the W14 centre and suggested that this could be attributed to the presence of excited states. He made measurements of half- and third-field transitions on the W13 and R1 centres whereas the complicated spectra did not permit the resolution of the other centres.

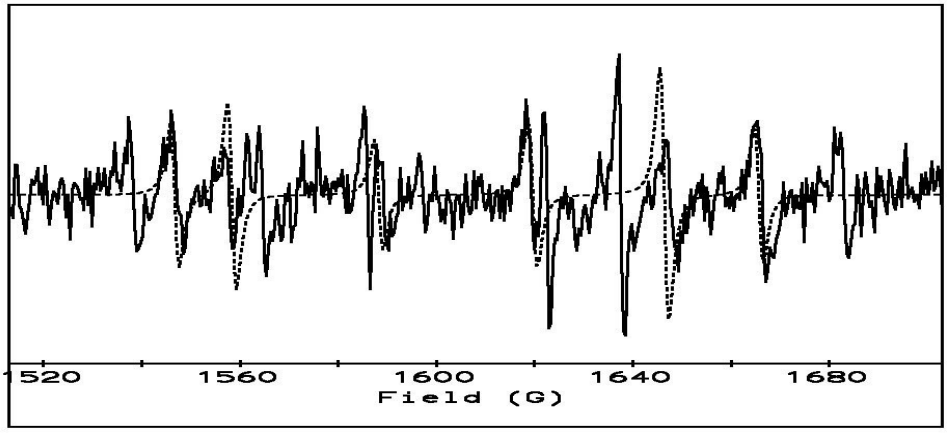

Figure 9.4: 1st derivative $\Delta m_s=2$ EPR spectra with the Zeeman magnetic field parallel to <111>-in sample J4 after annealing at 350 ºC. The dotted line is the calculated spectrum for the W11 centre whereas the full line represents the experimental data.

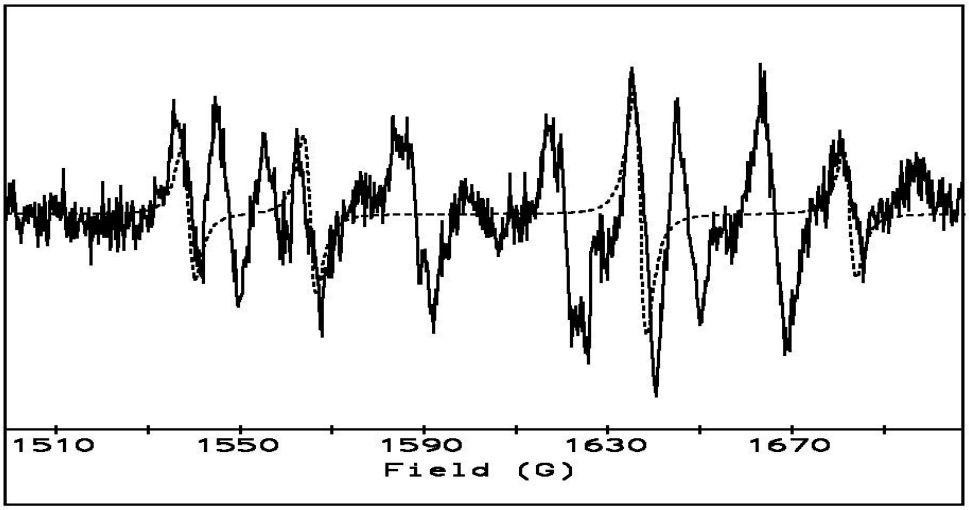

Figure 9.5: 1st derivative $\Delta m_s=2$ EPR spectra with the Zeeman magnetic field parallel to <111>-in sample J4 after annealing at 350 ºC. The dotted line is the calculated spectrum for the W13 centre whereas the full line represents the experimental data.

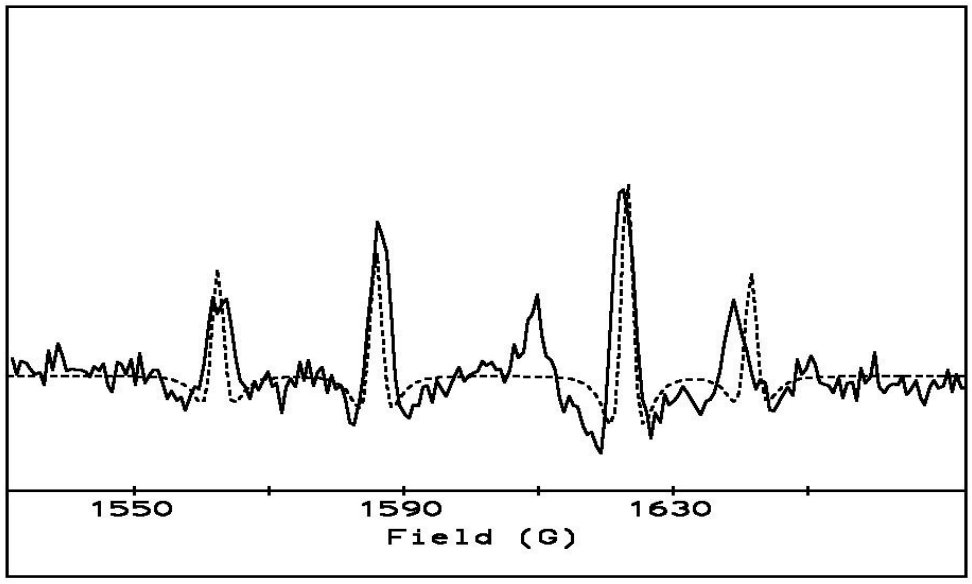

Figure 9.6: 1st derivative $\Delta m_s=2$ EPR spectra with the Zeeman magnetic field parallel to <111>-in sample J4 after annealing at 350 ºC. The dotted line is the calculated spectrum for the W14 centre whereas the full line represents the experimental data.

The parameters based on accurately measured magnetic fields and the corresponding resonance frequencies for EPR peaks were used to simulate the half-field ($\Delta m_S = 2$) transitions for the W11-W14 centres. The spectra for the W11 and the W13 centres are shown in Figures 9.4 and 9.5, respectively. They are seen to be relatively weak in comparison with the W14 centre whose spectrum is shown in Figure 9.6.

The observation of the third field or $\Delta m_s = 3$ transitions is normally very useful in identifying the centres with $\Delta m_s = 3/2$. (In fact, these transitions will be used to conclusively determine the effective spin for the W29 centre in chapter 9). The intensities were too low to allow the observation of the third field spectra for the W11-W14 centres.

9.4 Discussion

9.4.1 Annealing

The annealing curves of Figure 9.2 show that the W11 centre annealed out between 250ºC and 300ºC, the W12 and the W13 annealed out just under 400ºC whereas the W14 annealed

out just above 400ºC. Initially the W11 was the most intense of these centres. As it annealed out, W12 showed some growth. Also as W12 and W13 annealed out, a growth in the intensity of W14 was observed. This probably points towards some correlation between these centres.

Furthermore, the annealing temperature range suggested the involvement of interstitials in the structure of the W11-W14 centres. A review of some interstitial-related centres and their annealing curves has been given in chapter 5.

As to the interstitial, there have been proposals by Kiflawi *et al*. (1996) and Goss *et al.* (2004) that the H1a optical centre involves interstitial nitrogen. We can rule out a relationship between this optical centre and the W11-W14 centres since the H1a centre is observed only after 800 ^{o}C annealing.

The W11-W14 centres anneal out in the temperature range in which the self-interstitial are mobile which is well below the temperature at which the vacancy becomes mobile. It is therefore highly probable that the interstitial is involved in the structure of these defects.

The fact that the concentration of W15 starts to increase substantially *only* following isochronal at annealing temperatures much higher than the annealing temperatures for W11-W14 centres (Figure 9.2) , may be another suggestion that the nitrogen necessary for the formation of the centres is not a nearest neighbour to the negative vacancies.

The interstitial involved is most likely the R2 centre which is most abundant in the temperature range before the W11-W14 centres anneal out. As may be seen in Fig. 9.7 below, the disappearance of the R2 centre correlates with the growth of the negative vacancy (S1). To interpret this we suggest that as R2 anneals out, the W11-W14 centres also anneal out as a result of the perturbation on the negative vacancy being removed. The result is that the negative vacancy grows as shown in Figure 9.7 and agrees with the work of Twitchen *et al.* (2001).

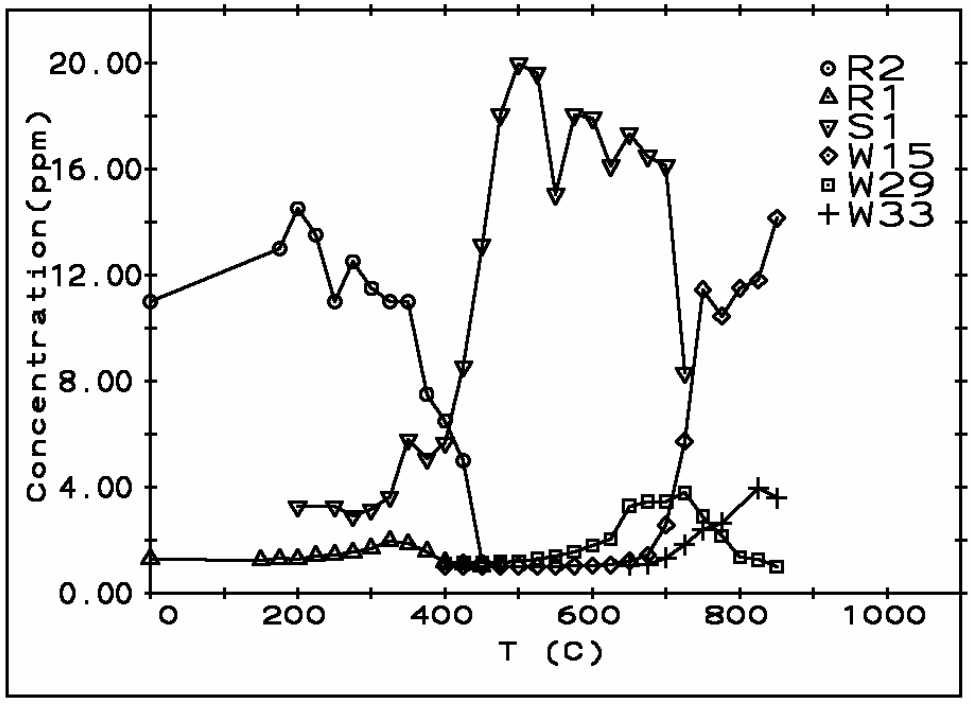

Figure 9.7: Plot of concentration (ppm) versus annealing temperature for a few representative defects observed with a-line (the same figure given earlier as Fig. 7.4).

This also finds agreement with a similar proposal by other workers that the W11-W14 centres are (V^--I^o)-complexes (Iakoubovskii *et al.*, 2005) whose findings suggested that the W11 and W13 centres are vacancy-interstitial complexes. However, it is not easy to see how the V^--R2 complex can be reconciled with the symmetry characteristics of the W11-W14 centres.

9.4.2 Linewidths

The widths of EPR lines in diamond depend on the paramagnetic defects. Kittel and Abrahams (1953) showed that the widths of such lines should be proportional to concentration for highly diluted paramagnetic system. Van Wyk *et al.* (1997) have investigated the dependence of the EPR linewidths of the P1 centre on the concentration of the nitrogen defects in a suite of type Ib diamonds. They found that the peak-to-peak linewidth δ could be expressed in terms of the paramagnetic defect concentration C_e as

$$\delta = \left(1.2\times10^{-4}\, C_e^2 + 0.014\right)^{1/2} \text{G} \qquad (9.1)$$

The linewidths for the W11-W14 centres measured in sample J3 have been shown in Table 9.1 and all lie between 1 and 2 G. This agrees favourably with the dependence of Equation 9.1 according to which a concentration of P1 centres 100 ppm corresponds to linewidth of 1.2 G. The agreement suggests that the widths of the W11-W14 centres are due to the dipolar interaction with the P1 centres.

We conclude that since P1 would determine the linewidth for centres in J3, we expect other centres observed together with the P1 centres to have widths of order of 1 G. The fact that R1 has a linewidth of 0.16 G, means that, unlike the W11-W14 centres, the defect is found in regions with low nitrogen concentration. This is consistent with the well known fact that during HPHT diamond synthesis; different sectors take up different amounts of nitrogen (Watt *et al.*, 2001; Burns *et al.,* 1999; Burns *et al*., 1990; Goss *et al*., 2007).

The very narrow linewidth of R1 is unusual and may be explained as follows. The vacancy of the interstitial-vacancy (or Frenkel pair) formed during irradiation traps the electron from the P1 and gives rise to the W11-W14 centres if the pair is sufficiently close to the P1 centre. However, if the interstitial-vacancy pair is further removed, the R1 centre will be formed instead. In this case the R1 would be farther removed from the P1 and hence experience a weaker dipole-dipole interaction which seems to be the most important broadening mechanism. The same appears to be true for the R2 centre which was not observed in J3. In fact, other workers showed that the intensity of the R2 centre is weakest in type Ib diamond but strongest in IaA diamonds (Iakoubovskii *et al*., 2003).

9.4.3 Concentrations

The concentration of W11 was very similar in samples J1, J2 and J3 with different concentrations of the P1 centres as shown in Figure 9.3(b). This is because the concentration of W11 is determined only by the dose which was the same for all the samples. We therefore suggest that the W11 centre was uniformly distributed in the crystal. By contrast, the R1 centre appeared to be unstable near a P1 centre but formed when the P1

concentration is low. Accordingly, in neutron-irradiated diamond in which P1 could not be observed by EPR, thought to be through ionization (Lawson *et al.*, 1998), we observed a very strong R1 EPR centre. The centres W12, W13 and W14 were similar in their annealing behaviour, symmetries and spin Hamiltonian parameters with the W11 centre; they were probably uniformily distributed as well.

9.4.4 Are some W11-14 centres components of perturbed vacancies?

We have the opinion that following electron or neutron irradiation damage in the diamond lattice, there would be interstitials and vacancies close together yet not near enough to recombine. The vacancy would then trap electrons from nitrogen defects to give rise to vacancy-interstitial complexes in which the vacancy is perturbed by the interstitial. The W11-W14 centres could be examples of these perturbed centres. Two groups of workers have reported findings that appear to support this assertion.

The first group of Collins and Dahwich (2004), observed a release of interstitials by annealing the 2.535 eV centre (thought to be a nitrogen-interstitial complex). Some of the released interstitials annihilated vacancies immediately while others moved on to a split <001> site and enhanced the absorption at 1.859 eV.
The second investigation has been made by Iakoubovskii *et al*. (2005) who reported that negative vacany-neutral interstitial (V^{-}-I^{o}) complexes existed in different configurations and could interconvert upon an annealing at T~230 ^{o}C; they identified two of these as the 2.535 eV and 2.367 eV optical centres and assigned them to the W13 and W11 EPR centres, respectively.

Iakoubovskii *et al*. (2005) also suggested that there was no involvement of the nitrogen in the (V^{-}-I^{o}) pairs owing largely to the lack of hyperfine splitting. This agrees with our view presented above that the nitrogen plays only the secondary role of donating an electron and not involved in the atomic structure of the W11-W14 centres.

9.4.5 Possible models

Even though the nitrogen concentration may be large in type Ia diamonds, none of the centres will be observed unless they contain P1 centres. Now, by definition, type Ib

diamond contains substantial concentrations of P1 centres. Observation of the W11-W14 centres in such diamonds suggests that nitrogen is an important factor in the formation of the W11-W14 centres. We think that each of these centres is a complex defect requiring 3 entities for their formation. These are the interstitial, a nitrogen atom and a vacancy. The nitrogen does not appear to be involved in the structure of these centres other than donating electrons.

We offer two pieces of experimental evidence for this. Firstly, no nitrogen hyperfine structure is observed - in agreement with the findings of (Iakoubovskii, 2005). Secondly, if nitrogen were the interstitial involved in the ($V\text{-}I^{o}$) complexes, the annealing out of the W11-W14 centres would give rise to concentrations that are comparable to W15 centre concentration. The annealing curves of Figure 9.7 (which has been given earlier as Figure 7.4, but reproduced for easy reference) shows that this is not observed. The negative vacancy increases after the W11-W14 anneal out (just before 400 ^{o}C) probably suggesting the release of the negative vacancy from the ($V\text{-}I^{o}$) complexes.

9.5 Conclusion

The fact that W11-W14 centres are observed in type Ib diamond suggests that the centres may involve single substitutional nitrogen. Furthermore, owing to the temperature range in which they are observed, the interstitial appears essential in the formation. From our annealing curves we conclude that nitrogen impurities are not directly involved but donate electrons to the interstitial-vacancy centres. This is supported by the fact that no nitrogen hyperfine interaction is observed in the EPR spectra for these centres.

We suggest that further work should be done using samples with large concentrations of the W11-W14 centres in order to, among other aims, investigate the relationship between these centres and the P1 centre. Relative changes of the intensities for the W11-W14 centres in comparison with the negative vacancy would then be easier to follow in the annealing experiments.

CHAPTER TEN

THE W29 EPR CENTRE IN DIAMOND

10.1 Introduction

Many centres such as the R1 and R2 centres that have been discussed in chapter 5 had completely annealed out following isochronal annealing of sample J4 to about 700 K. Another group of centres started to be observable as the annealing temperatures were increased. One of these centres is the W29 and forms the subject of this chapter.

The W29 centre was the most dominant centre after a-line shown in Figure 10.1; the intense line at the centre of the spectrum is the a-line. The two centres W29 and R4/W6 showed unusual relaxation behaviour and will be discussed in chapter 11.

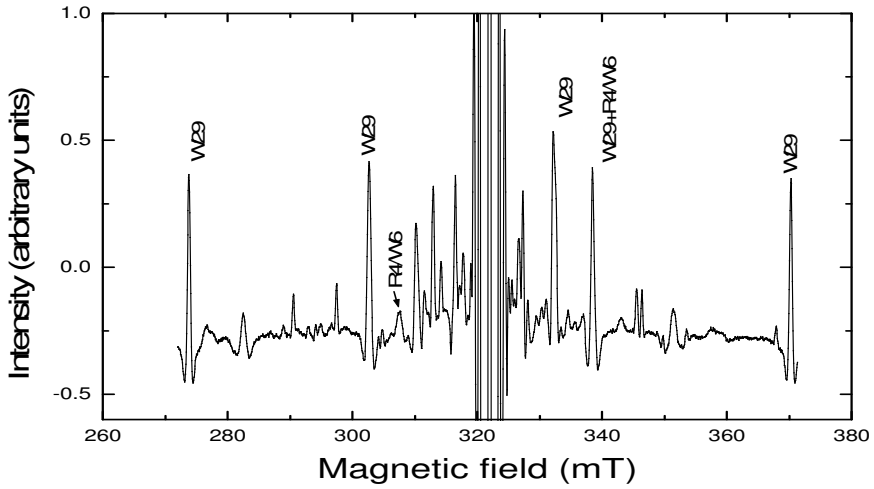

Figure 10.1: 2nd derivative spectra for EPR centres in neutron-irradiated type Ib diamond after isochronal annealing at 700 °C. The spectrum was obtained with the magnetic field parallel to <111> -direction. The intense lines at the centre of the spectrum belong to the a-line.

10.2 Experimental results

10.2.1 Spin Hamiltonian parameters

The angular variation of the fine structure lines for the W29 centre as the sample was rotated around a $\langle 110 \rangle$ axis is shown in Figure 10.2. The rotation is from $\langle 100 \rangle$ to $\langle 110 \rangle$ crystallographic directions in a {110} plane of the diamond lattice.

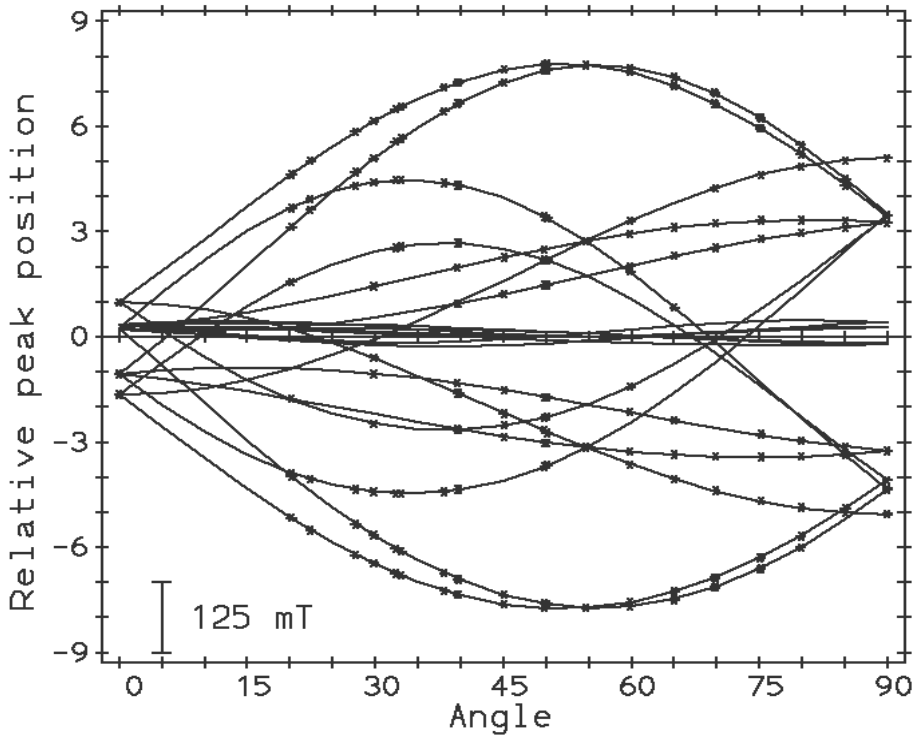

Figure 10.2: Angular variation of the W29 EPR centre with the magnetic field rotated from a <100>-direction to a <110>-direction in a {110}-plane. The stars are the experimental data used for the least squares fitting.

It is evident that the major principal axis of the defect is close to a $\langle 111 \rangle$ direction. The data obtained was fitted to the spin Hamiltonian

$$H = \beta \hat{S}.\underline{g}.\hat{B} + \hat{S}.\underline{D}.\hat{S} \qquad (10.1)$$

It was not easy to decide whether the effective spin S was 1 or $\frac{3}{2}$ for the W29 centre. In the latter case there would be an additional line corresponding to the transition $m_s = +\frac{1}{2}$ to $m_s = -\frac{1}{2}$ occurring in the $g = 2$ region and would be totally hidden by the

intense spectrum, mostly the S1 centre, in that region. There was, however, a more satisfactory fit to the spectrum with S=$\frac{3}{2}$ and this indicated that $S \neq 1$.

Our observation of the $\Delta m_s = 3$ transitions in the $g = 4$ region provided conclusive evidence that S>1 and calculations show that if $S = \frac{3}{2}$, then this transition would be detectable when the magnetic field is applied along a $\langle 111 \rangle$ axis. Simulated spectra for the W29 using the spin Hamiltonian parameters obtained following the best fit with the magnetic field in the $\langle 111 \rangle$ as well as an experimental spectrum recorded at 100 K are shown in Figure 10.3. The experimental spectrum shows $\Delta m_s = 2$ peaks for the W29 and also some associated with other centres. The peak at the extreme left is definitely due to a $\Delta m_s = 3$ transition.

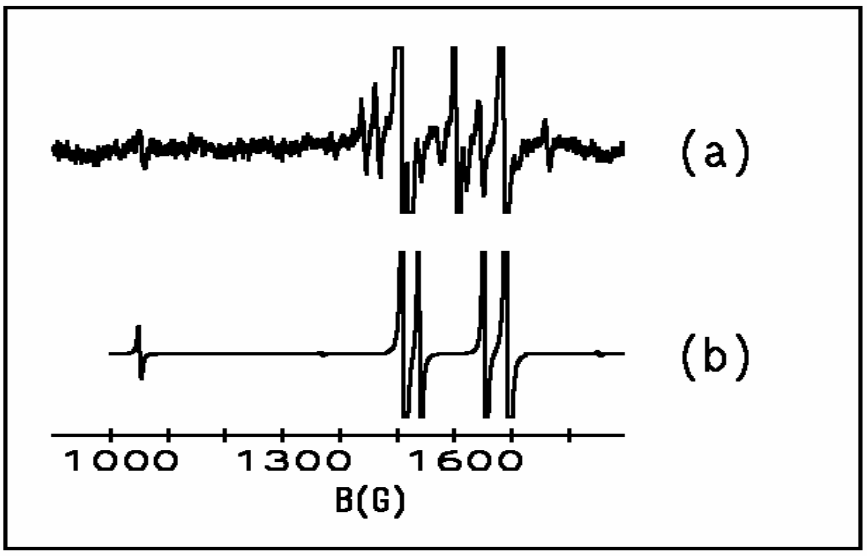

Figure 10.3: (a) The experimental spectrum in sample J4 annealed for 10 minutes at 950 K with the magnetic field also in the $\langle 111 \rangle$-direction.(b) The calculated spectrum of W29 in the half-field and third-field regions with the magnetic field along the $\langle 111 \rangle$ - crystallographic axis.

Table 10.1 given below shows the spin Hamiltonian parameters obtained on least-squares fitting of the data represented by the stars in Figure 10.2; the effective spin $S = \frac{3}{2}$.

Table 10.1: Spin Hamiltonian parameters for W29 centre. The principal *x*-axis is in a $[01\bar{1}]$-direction whereas the principal *z*-axis was close to the [111]- axis in the $\{01\bar{1}\}$-plane.

D_{xx}(MHZ)	$\mp 296.9(6)$
D_{yy}(MHz)	$\mp 156.3(6)$
D_{zz}(MHz)	±453.2(3)
principal *x*-axis	$[01\bar{1}]$
principal *z*-axis	[0.619, 0.556, 0.556]
g (isotropic)	2.0022(2)

10.2.2 Sign of D-tensor for the W29 centre

An attempt was made to determine the sign of D by comparing the intensities of the outermost $\Delta m_S = \pm 1$ transitions of W29 at 7 K, and in a direction close to the *z*-axis of the D-tensor. Suppose that I_{HF} and I_{LF} represent the intensities of the EPR signal in the high field and low field regions respectively. One can readily show that if $D < 0$ then $\frac{I_{HF}}{I_{LF}} < 1$ and $\frac{I_{HF}}{I_{LF}} > 1$ if $D > 0$. Experimentally the magnetic field was applied in a (110)-plane, and in a direction between the <111>-axis and the z-axis. The outermost $\Delta m_S = \pm 1$ lines then consist of an outer single line, corresponding to a W29 centre whose *z*-axis lies in the plane in which the magnetic field is rotated, and a line with twice the intensity due to W29 centres whose *z*-axes lay in two other (110)-planes. For the single line it was found that $\frac{I_{HF}}{I_{LF}} > 1$ and for the double line $\frac{I_{HF}}{I_{LF}} < 1$. The deviation of these values from 1 was also greater than expected.

From the foregoing it appears that the intensities of the W29 lines studied did not depend only on the Boltzmann population of states. Some other unidentified causes must contribute to the intensities of the lines as observed. Hence, the sign of D could not be determined.

10.2.3 Isochronal annealing of W29 centre

Isochronal annealing curves for W29 and other EPR centres is shown in Figure 10.4.

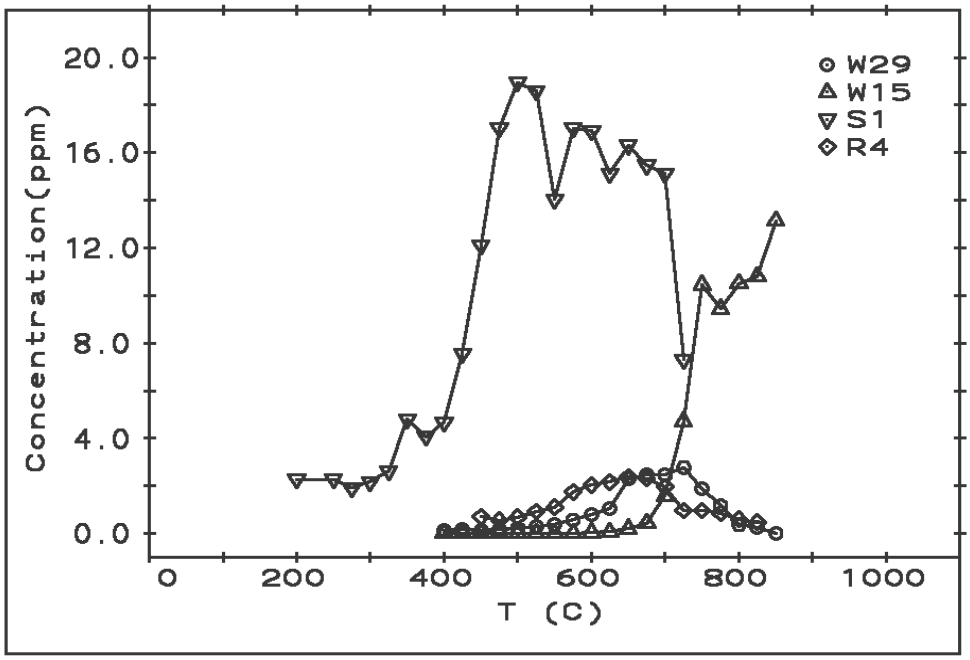

Figure 10.4: Annealing curves for W29 centre. Also shown are the annealing curves for R4/W6, S1 and W15 centres.

The concentration of the W29 centre was about 0.1 ppm after isochronal annealing at 400 ^{o}C, but grew as the annealing temperatures were raised peaking at 725 ^{o}C at a value of about 3 ppm. It then abruptly annealed out such that at 850 ^{o}C its concentration was under 0.01 ppm. The R4/W6 centre behaves in a manner that is almost identical to that of the W29 centre.

10.3 Discussion

10.3.1 Similarities between R4/W6 and W29

The R4/W6 EPR centre in diamond (Lea-Wilson *et al.*, 1995) is a centre with effective spin $S = 1$ and is commonly observed in electron- and neutron-irradiated type Ia and type IIa diamonds that have been annealed to temperatures between 700 K and 1200 K. Its zero-

field tensor *D* has rhombic symmetry with its principal axis parallel to the $\langle 111 \rangle$-crystallographic axis. Correlation studies of R4/W6 EPR centre and the optical TH5 centre by Clark *et al.* (1956) showed that it consists of 2 GR1 or neutral vacancy centres i.e. it is a neutral divacancy centre. Twitchen *et al.* (1999) have confirmed this identification using hyperfine structure of 5% ^{13}C enriched synthetic diamond.

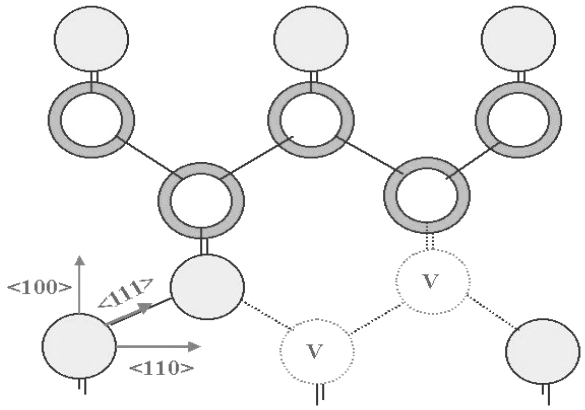

Figure 10.5: The diamond lattice showing the R4/W6 centre. The plane of the paper is (110). The light-shaded atoms are on the (110) plane containing the divacancies; the dark-shaded ones are above this plane while the unshaded ones are below it.

Figure 10.5 shows the neutral divacancy (R4/W6) in the diamond lattice viewed perpendicular to a (110) plane containing light-shaded atoms. The other two $\{110\}$-planes above and below this plane contain unshaded and dark-shaded atoms, respectively. The spin Hamiltonian parameters due to Twitchen *et al.* (1999) are given in Table 10.2.

Table 10.2: The principal components of the g- and D–tensors for the R4/W6 centre.. The angles given in the form [θ,φ] the right of each component refer to spherical coordinates expressed in cubic axis system. The subscripts of the tensor components 1, 2 and 3 correspond to *xx*, *yy* and *zz* respectively, in the notation for the components given in Table 10.1 for the W29 centre. The data has been taken from Twitchen *et al.* (1999)

R4/W6 EPR centre	
g matrix	**D** (MHz)
g_1=2.0022(1) [90°, 315°]	D_1=+103(2) [90°, 315°]
g_2=2.0026(1) [141(2)°, 45°]	D_2=+206(2) [144.2(5)°, 45°]
g_3=2.0013(2) [51(2)°, 45°]	D_3=-310(2) [54.2(5)°, 45°]

From Tables 10.1 and 10.2 for W29 and R4/W6 centres respectively, it may be noted that both centres have large D values and E-terms. The results further suggests that $D = \frac{3}{2} D_{zz}$ and $E = {(D_{xx} - D_{yy})}/{2}$ for the centres are in a ratio very close to 3:2 with their E-terms having opposite signs. The g-tensors are isotropic and very close to the free spin value.

Experimentally, it has been shown that the intensity of P1 (single substitutional nitrogen) centres in type Ib diamonds is reduced during irradiation to a level depending on the irradiation dose (Davies, 1992). Indeed in a diamond that was heavily irradiated with neutrons (J4), the S1 centre was formed under the beam as was detected as a component of the a-line. It appears therefore that the vacancies trap the electrons torn off from the nitrogen atoms and thus giving rise to $P1^+$ which is EPR-inactive. This source of electrons is available in type Ib diamonds in which the electrons appear to be readily captured by defects.

W29 has always been observed in type Ib diamond suggesting that P1 plays an important role. The similarities noted above between R4/W6 and W29 and the fact that R4/W6 is a neutral divacancy also suggests the involvement of the divacancies in the W29 centre.

10.3.2 Isochronal annealing of the W29 centre

Referring to the annealing curves of Figure 10.4, it may be seen that there is a gradual decrease in the concentration of S1 for annealing between 500 ^{o}C and about 650 ^{o}C, while R4/W6 and W29 grow and nearly reach theire peak concentrations in this range. The annealing behaviour for R4/W6 is similar to that determined on type IIa electron irradiated diamond by Lea-Wilson (1988) who showed that the divacancy centre grew and peaked at 700 ^{o}C before annealing out just above 900 ^{o}C.

It is a fact that the mobility of the vacancies during annealing at or below 400 ^{o}C is expected to be small. The low concentration of the W15 centre that is observed in Figure 10.4 is due to the statistical probability that a vacancy is produced next to the nitrogen during the irradiation. It was only after the vacancy become mobile i.e. following the annealing at 650 ^{o}C that the growth of W15 became appreciable.

The concentration of P1 in J4 before irradiation and annealing was about 120 ppm (Table 6.1). During irradiation the vacancies that are created, and probably other defects, trap the donor electrons of the P1 centres. From the annealing curves of Figure 10.4, it may be seen that only about 20 ppm of negative vacancies and about 10 ppm for the vacancy related centres such as the W29, R4/W6 and are recorded. This would leave out close to 90 ppm or 75 % of donated electrons not accounted for unless these are trapped at defects giving rise to the a-line.

For now, the growth processes for the W29 and R4/W6 centres remain unclear.

10.4 Conclusion

Our observations show that the W29 forms in the temperature range where the vacancies are mobile and that it anneals out at roughly the same temperature range with the R4/W6 - the neutral divacancy in diamond. It is also formed in diamonds where the donor electrons are available. The linewidth variations with temperature (to be discussed in the next chapter) are very similar though larger for the W29 centre. Further, the W29 centre has a similar symmetry to that of the R4/W6 i.e. its principal axis is very close to $\langle 111 \rangle$-direction.

Based on these considerations, we have proposed that the W29 centre is a negative divacancy (Kirui *et al*., 1999) as depicted in Figure 10.6. The two vacancies and the two carbon atoms, to the left and the right of it, are in the plane of the paper. The concentric circles represent carbon atoms above and below this plane.

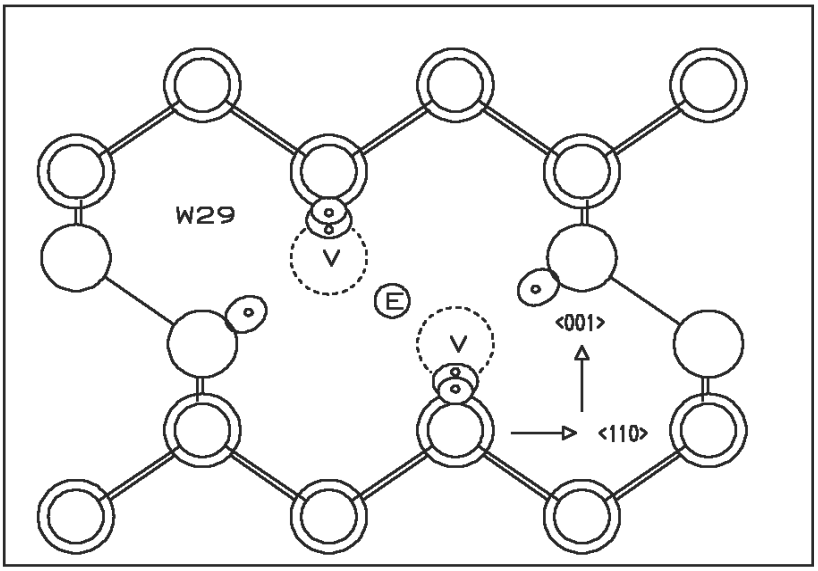

Figure 10.6: A model for W29 centres in diamond. The plane of the paper is (110) and contains the two vacancies of the centre. The concentric circles represent atoms on two other (110) planes- the large circles depict the atoms on the plane above and the smaller circles denote the atoms on the plane below. The small circle with the E represents the electron that has been trapped by the divacancy.

CHAPTER ELEVEN

RELAXATION TIMES FOR W29 AND R4/W6 CENTRES

11.1 Introduction

Van Wyk *et al.* (1997) have showed that the EPR linewidth for P1 centres in diamond varied linearly with concentrations above 10 atomic parts per million (ppm). At concentrations less than this, the linewidth remained constant being due to inhomogeneous broadening caused by the ^{13}C hyperfine interactions. Reynhardt *et al.* (1998) have also shown that temperature variations of the linewidths are not drastic for defects in diamond in the absence of nuclear or paramagnetic electron motions or both.

The linewidths of most centres recorded in this work were very broad; the widths could not be explained by the model of van Wyk *et al*. (1997). Even so, there was hardly any significant variation over large temperature ranges say from 300 K to 80 K. By contrast, centres R4/W6 and W29 exhibited very striking linewidth variations with temperature following annealing of sample J4 to about 500 ^{o}C. As a consequence the R4/W6 centre could not be observed at all at room temperature. These linewidth variations were also accompanied by changes in the saturation behaviour of the spectra, which in turn indicated changes in relaxation times.

Ideally the relaxation times T_1 and T_2, which are, respectively, the spin-lattice and spin-spin relaxation times, should be determined using pulsed EPR saturation techniques. In this work, however, the short relaxation times for W29 could not permit the application of the technique and therefore the steady state or continuous wave (CW) experiments were carried out instead. Generally, this technique only enables the determination of the product T_1T_2 where T_2 , the spin-spin relaxation time is associated with the width of the spin packets. The saturation behaviour of a spin system is useful in the determination of its T_1 .

Saturation curves for most EPR centres in diamond indicate that the lines are inhomogeneously broadened. In this case, however, the widths of the spin packets become comparable to the widths of the spin packet envelope. Consequently, the equations as derived by Castner (1959) do not apply and must be slightly modified. The modifications for the saturation behaviour and linewidth variations are presented in sections 11.2 and 11.3, respectively.

In this chapter, the linewidth changes arising from the relaxation time variations will be investigated.

11.2 Modified saturation equations

The absorption magnetic susceptibility (Caster, 1959) is given by

$$\chi''(\omega) = \frac{1}{2}\chi_0 \int_0^\infty \frac{\pi\omega' g(\omega-\omega') h(\omega-\omega_0)\, d\omega'}{1+\pi\gamma^2 H_1^2 T_1 g(\omega-\omega')}. \tag{11.1}$$

where $g(\omega-\omega')$ and $h(\omega-\omega')$ are the shape function and distribution function of the spin packet, respectively.

For W29 the width of the spin packets is no longer determined solely by T_2 and the following expression is used for the shape function of the spin packet:

$$g(\omega-\omega') = \frac{1}{\pi\Delta_L} \frac{1}{1+(\omega-\omega')^2/\Delta_L^2}. \tag{11.2}$$

where Δ_L is the width at half height of the Lorentzian spin packet. The expression used for the distribution function of the spin packets is

$$h(\omega'-\omega_0) = \sqrt{\frac{1}{\pi}} \frac{1}{\Delta_G} \exp\left[-\left(\frac{\omega'-\omega_0}{\Delta_G}\right)^2\right]. \tag{11.3}$$

Substituting Equations (11.2) and (11.3) into Equation (11.1) yield

$$\chi''(\omega) = \frac{1}{2}\chi_0 \sqrt{\frac{1}{\pi}} \frac{1}{\Delta_G\Delta_L} \int_0^\infty \frac{\omega' \exp\left[-\left(\frac{\omega'-\omega_0}{\Delta_G}\right)^2\right] d\omega'}{1+\Delta_L^{-2}(\omega-\omega')^2 + \gamma^2 H_1^2 T_1 \Delta_L^{-1}}$$

or

$$\chi''(\omega) \propto \int_0^\infty \frac{\omega' \exp\left[-\left(\frac{\omega'-\omega_0}{\Delta_G}\right)^2\right] d\omega'}{1+\Delta_L^{-2}(\omega-\omega')^2 + \gamma^2 H_1^2 T_1 \Delta_L^{-1}} \tag{11.4}$$

If we let

$$x = \frac{\omega' - \omega_0}{\Delta_G}, \quad y = \frac{\omega - \omega_0}{\Delta_G} \quad \text{and} \quad \Delta_R = \frac{\Delta_G}{\Delta_L} \tag{11.5}$$

then

$$\chi''(y) \propto \int_{-\infty}^{\infty} \frac{(x\Delta_G + \omega_0)\exp\left[-(x)^2\right]dx}{1 + \left\{(y-x)/\Delta_R\right\}^2 + \gamma^2 H_1^2 T_1 \Delta_L^{-1}}$$

or

$$\chi''(y) \propto \int_{-\infty}^{\infty} \frac{\exp\left[-(x)^2\right]dx}{1 + \left\{(y-x)/\Delta_R\right\}^2 + \gamma^2 H_1^2 T_1 \Delta_L^{-1}} \tag{11.6}$$

since $\omega_0 \approx x\Delta_G$.

Finally, if $\frac{1}{\Delta_L} = \frac{1}{T_1} + \frac{1}{T_2}$ then

$$\chi''(y) \propto \int_{-\infty}^{\infty} \frac{\exp\left[-(x)^2\right]dx}{1 + \left\{(y-x)/\Delta_R\right\}^2 + \gamma^2 H_1^2 \frac{T_1^2 T_2}{T_1 + T_2}} \tag{11.7}$$

No attempt was made to simplify this equation further as it can be integrated readily using numerical methods.

11.3 Modified linewidth functions

If we have a Gaussian distribution of Lorentzian spin-packets then the envelope will be given by

$$\begin{aligned} G(\omega - \omega_0) &= \int_0^{\infty} h(\omega' - \omega_0) g(\omega - \omega')\, d\omega' \\ &= \int_0^{\infty} \sqrt{\frac{1}{\pi}} \frac{1}{\Delta_G} \exp\left[-\left(\frac{\omega' - \omega_0}{\Delta_G}\right)^2\right] \frac{1}{\pi\Delta_L} \frac{1}{1 + (\omega - \omega')^2 / \Delta_L^2} d\omega' \end{aligned} \tag{11.8}$$

Again using 11.2, 11.3 and 11.5 gives

$$G(y) \propto \int_{-\infty}^{\infty} \exp\left(-x^2\right) \frac{1}{1 + (y-x)^2 / \Delta_R^2} dx \tag{11.9}$$

This equation was most frequently required to calculate the peak-to peak width of the first derivative of the envelope. For this we need the first or second derivative of Equation (11.9). Note that

$$\begin{aligned} \frac{d^n\left[G(y)\right]}{dy^n} &\propto \frac{d^n}{dy^n}\left[\int_{-\infty}^{\infty} \exp\left(-x^2\right) \frac{1}{1 + (y-x)^2 / \Delta_R^2} dx\right] \\ &\propto \int_{-\infty}^{\infty} \exp\left(-x^2\right) \frac{d^n}{dy^n}\left[\frac{1}{1 + (y-x)^2 / \Delta_R^2}\right] dx \end{aligned} \tag{11.10}$$

Again no attempt was made to simplify this equation and linewidths were calculated using numerical methods.

11.4 Relaxation processes

Spin-phonon interaction plays an important role in the electron spin relaxation. The relaxation mechanisms that are likely to be important for defects in diamond include the direct, the Raman and the Orbach relaxation processes. The cross-relaxation mechanism is expected to be significant only for EPR systems in diamond that are highly overlapping such as those with P1 and N3 (three substitutional nitrogen atoms on a {111} plane bonded to a common vacancy) centres (Reynhardt *et al*., 1998). In such systems there are many energy level crossings (Larson and Jeffries, 1966). Accordingly, the cross relaxation process is not expected to be efficient in relaxing the systems in type Ib diamond that are reported in this work.

The direct process involves one phonon interacting with the electron spin whereas the Raman and Orbach processes take place via the creation of one phonon and the annihilation of another (Finn *et al*. 1961; Orbach, 1961). An expression for the relaxation rate for the direct process is given by (Pake, 1962; Reynhardt *et al.* 1998)

$$\frac{1}{T_1} = \frac{54\pi\nu^2}{\hbar^2 \rho \upsilon_0^5}\left(\frac{\beta^2}{r_0^3}\right)^2 kT \qquad (11.11)$$

where ρ represents the density of the lattice material, ν the oscillator frequency, υ_0 the speed of sound in the crystal, r_0 the lattice separation and β the Bohr magneton. The expression may be written as

$$\frac{1}{T_1} = CH_0^2 kT \qquad (11.12)$$

where C is a constant and H_0 is the magnitude of the external magnetic field. In diamond the speed of sound $\upsilon_0 = 1.3\times10^3$ ms-1 and because of the υ^5 dependence, the relaxation rate due to the direct process gives a value $T_1 \approx 10^2$ s at 300 K and $T_1 \approx 10^5$ s at 6 K.

The Raman process, on the other hand, is a higher order process that becomes effective at elevated temperatures where many high energy phonons have been excited. The relation for non- Kramers salts is (Orbach, 1961; Pake, 1962; Reynhardt *et al.* 1998)

$$\frac{1}{T_1} = \frac{163\pi^2 6!}{\rho 2 v_0^{10}} \left(\frac{\beta^2}{r_0^3} \right)^2 \left(\frac{kT}{h} \right)^7 \tag{11.13}$$

In the case of Kramers salts a relation for the relaxation rate is (Orbach, 1961)

$$\frac{1}{T_1} = C \left(\frac{kT}{h} \right)^9 \tag{11.14}$$

where C is a constant.

An Orbach process is expected if there is a real excited state of the EPR system situated Δ above the ground state and such that it is less than the Debye energy for the lattice, (Geshwind *et al.* 1965; Reynhardt *et al*., 1998; Pake, 1962). The relaxation rate is given by

$$\frac{1}{T_1} \approx \frac{3G^2}{h\rho v_0^5} \left(\frac{\Delta}{\hbar} \right)^3 \exp\left(-\frac{\Delta}{kT} \right) \tag{11.15}$$

where $G \approx 1.2 \times 10^{-21}\,\mathrm{J}$ is a constant

11.5 Experimental

Details of experimental procedures have been given in chapter 4. Saturation behaviour was determined by measuring the signal amplitudes of the centre for microwave powers incident on the cavity ranging from 200 μW to 200 mW.

The linewidths for the W29 and R4/W6 centres were measured using Oxford Instruments continuous flow cryostat in the range 6 to 77K.

11.6 Results

11.6.1 Linewidth variation of W29 centre

Linewidth measurements for the W29 centre were made in the range 6 to 300 K as shown in Figure 11.1 below. A minimum of about 2 G was recorded at slightly below 50 K. The

width then increased with temperature and reached a maximum of about 7 G at room temperature.

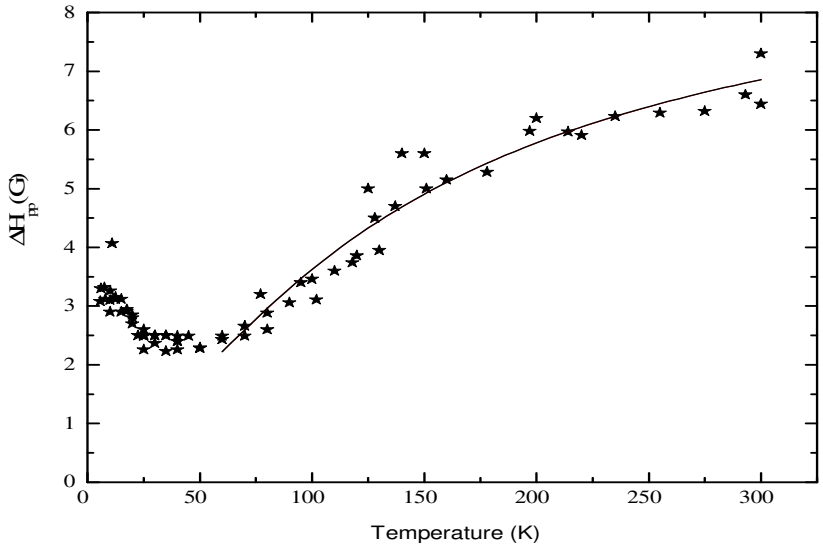

Figure 11.1: Linewidth ΔH_{pp} (G) versus T(K) for the W29 in neuron-irradiated and annealed type Ib diamond. The stars represent experimental data whereas the solid line represents calculated linewidths for W29 centre using Equation 11.6.

A nonlinear fit is also shown in Figure 11.1; the fitting has been done using *Origin 6.0* to the data in the range 70 – 300K. It was assumed that the variation of the linewidth ΔH_{pp} with temperature above 70 K obeyed the expression

$$\Delta H_{pp} = \Delta H_0 + B \exp\left(-\frac{E_a}{k_B T}\right) \tag{11.16}$$

where the constant ΔH_0 is the "natural" or residual width, k_B the Boltzmann constant and E_a a constant with units of energy. The fit yielded the following values: ΔH_0=1.56 ± 0.64 (G) ; B=8.66 ± 0.39 (G); E_a=10.8 ± 2.3 meV.

The linewidth ΔH_{pp} data in the low temperature range from about 70 to 5.7 K could be fitted to an inverse relation as shown in Figure 11.2 also using *Origin 6.0*. The fitting function was given by

$$\Delta H_{pp} = \Delta H_{0L} + \frac{B}{T} \tag{11.17}$$

where ΔH_{0L} represents a natural linewidth and B a constant. The fitting yielded values: ΔH_{0L} =(2.28 ± 0.07) ×10^{-4} (T); B=(7.70 ± 1.05) ×10^{-4} (T. K).

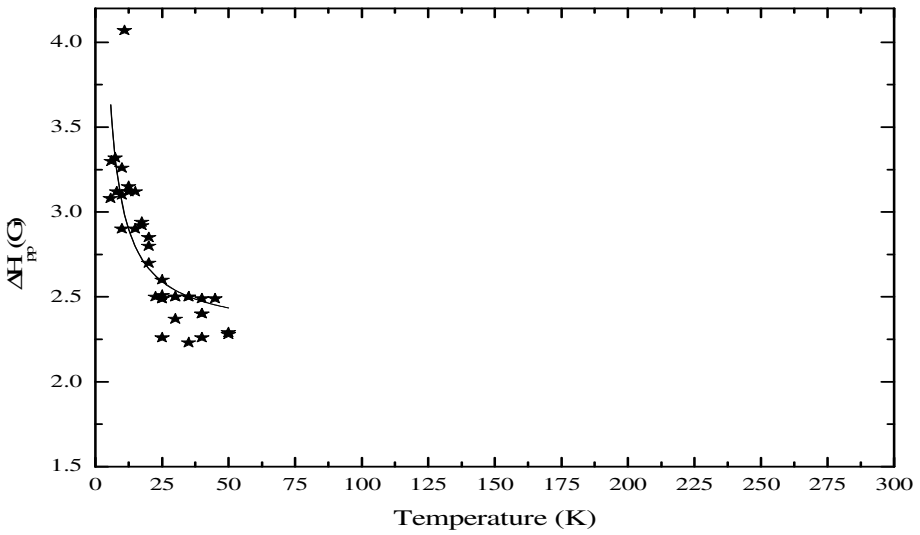

Figure 11.2: Linewidth ΔH_{pp} (G) versus T(K) for W29 in the temperature range 6 K to 50 K for sample J4. The stars represent experimental data whereas the solid line represents a fit to the data using Equation 11.17.

11.6.2 Saturation and spin-lattice relaxation time for the W29 centre

If a signal does not saturate then the intensity of the signal should be proportional H_1, the microwave magnetic field at the sample, or $\sqrt{P}$, where P represents the microwave power incident on the cavity. To establish the degree of saturation of the signal it is convenient to plot $\frac{V_P}{V_{PR}}$ against $\frac{\sqrt{P}}{\sqrt{PR}}$, where V is the intensity of the signal at power P and V_{PR} is the intensity of the signal at power level PR, the lowest power level at which a measurable signal is produced. If the signal does not saturate, a straight line with slope 1 should be produced.

A qualitative comparison of the power saturation of the W29, a-line and W15 centres at room temperatures may be seen in Figure 11.3. Of these 3 centres, the W15 centre is the most saturating with spin-lattice relaxation time T_1 of the order of milliseconds.

The a-line and W29 centres represent examples of centres that saturate at micro and nano-second rates, respectively.

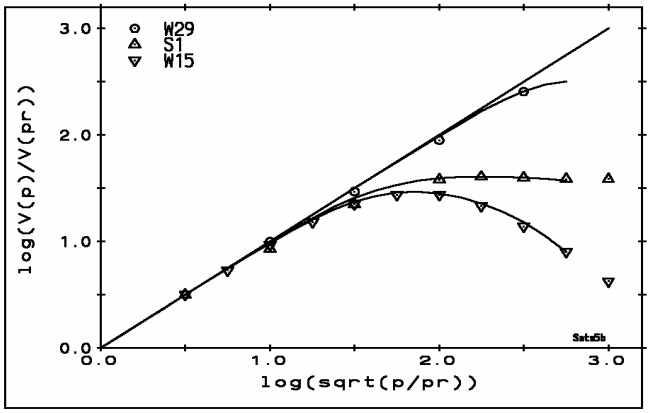

Figure 11.3: Saturation curves for S1, W29 and W15 (nitrogen-vacancy) centres measured at 300 K on type Ib diamond. The curves suggest that W15 is the most saturating while W29 is the least saturating of the 3 centres**.**

Saturation curves for W29 at various temperatures in the range 6 to 300 K are shown in Figure 11.4.

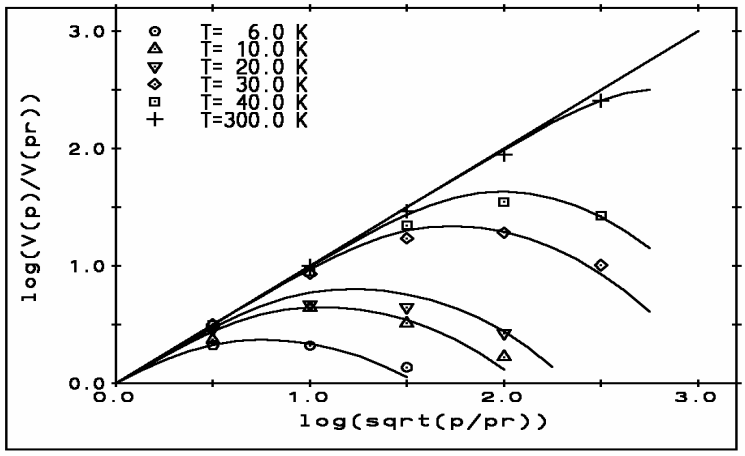

Figure 11.4: Saturation curves for W29 centre at various temperatures in sample J4 previously isochronally annealed to 750 ^{o}C. The solid lines were fitted in the manner described below.

The saturation behaviour is controlled by $\gamma^2 H_1^2 \frac{T_1^2 T_2}{T_1 + T_2}$ and Δ_R in Equation (11.7). It is almost impossible to extract absolute quantitative information from the saturation curves because of the number of variables involved. To extract values of T_1 , a knowledge of the proportionality constant (C_F) between P and H_1 (which depends on the cavity characteristics), T_2 (and its temperature dependence) and the width (Δ_G) of the spin packet distribution, are required. It is, however, expected that C_F, T_2 and Δ_G should be more or less constant. Owing to the use of the flow-through system, only the temperature at the sample was expected to change, so that C_F remained constant as the temperature of the cavity remained constant. For most centres in diamond T_2 is determined by the concentration of defects and is very slightly dependent on temperature.

To get estimates of T_1 a set of 'reasonable' values C_F, T_2 and Δ_G were determined, which gave most acceptable fits to the saturation curves over the whole temperature range; these were subsequently kept constant for the final determinations of T_1. It should be noted that different sets of these values may give equally acceptable fits, which will scale all T_1 values by nearly the same factor. This scale factor does not influence the analysis below.

Values for T_1 could also be obtained using Equation 11.9 if reasonable values for Δ_G (which can be obtained from the minimum in the linewidth versus temperature graphs) and T_2 are available. This method proved to be useful at the higher temperatures where the saturation effects were smaller.

A plot of $\frac{1}{T_1}$ versus $\frac{1}{T}\left(\mathrm{K}^{-1}\right)$ is given in Figure 11.5. The line in the figure represents a nonlinear fitting using *Origin 6.0* to the data with a function given by

$$\frac{1}{T_1} = A \exp\left(-\frac{E_a}{k_B T}\right) \tag{11.18}$$

where A is a constant and E_a, an activation energy. The fit is obviously very good and yielded the following values: $A = 1.71 \times 10^8 \pm 8.26 \times 10^6$ Hz ; E_a = 15.5 ± 0.7 meV. This function is similar to Equation 11.15 and therefore strongly suggests that the Orbach

relaxation process was the dominant relaxation mechanism for the W29 centre in the temperature range 50–300 K.

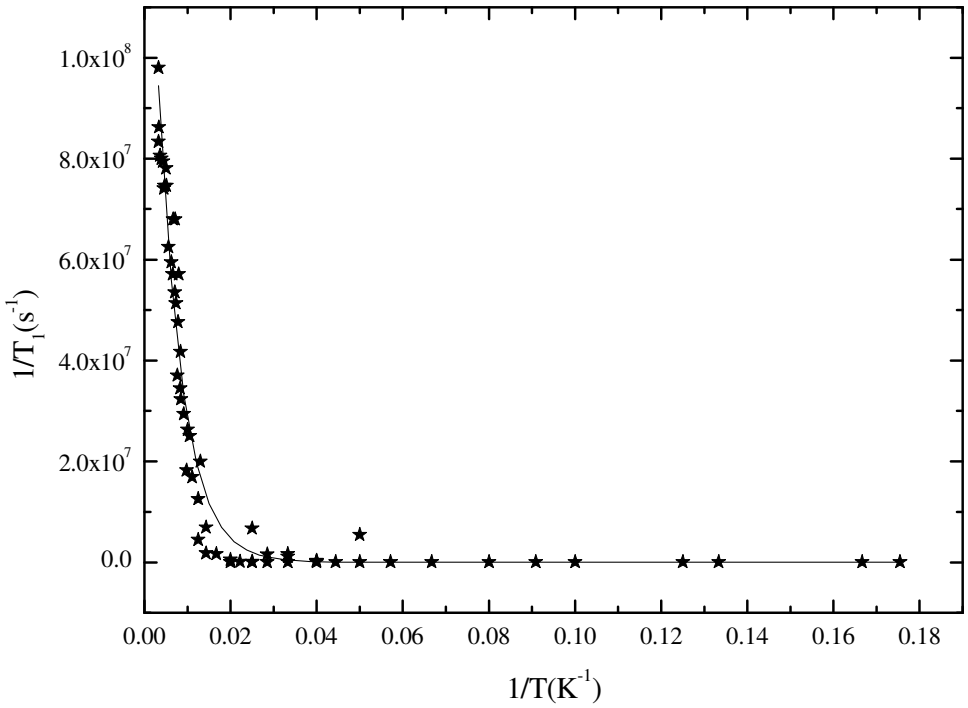

Figure 11.5: A plot of $\frac{1}{T_1}$ versus $\frac{1}{T}$ (K) for W29 centre. The stars (*) represent the experimental data whereas the line represents a least squares fit to Equation 11.8. There is a strong suggestion of the Orbach process at the higher temperatures and a direct process at lower temperatures.

The values of the activation energies as determined from Figures 11.1 and 11.5 are summarized in Table 11.1. It may be seen that the values agree favourably.

Table 11.1: Activation energies for W29 centre.

E_a(meV) from saturation data	E_a(meV) from linewidth data
15.5 ± 0.7	10.8 ± 2.3

As already mentioned, many factors affect the absolute value of T_1 causing it to change by a factor but the activation energy is not affected.

11.6.3 Intensity variations with temperature for the W29 centre

The intensity of a selected peak in the W29 spectrum, relative to the intensity of the same peak ($V(T_0)$) at room temperature (T_0), in the temperature range 90 K to 300 K, are plotted as a function of the relative temperature (T/T_0) in Figure 11.6. The graph shows that the quadruplet in which the EPR lines are observed is the ground state of the W29 defect. It is not expected that the excited state at 15.5 meV from the quadruplet, found for the Orbach process from the T_1 measurements, would have any effect on the populations of the ground state levels. This is borne out by the results of Figure 11.6.

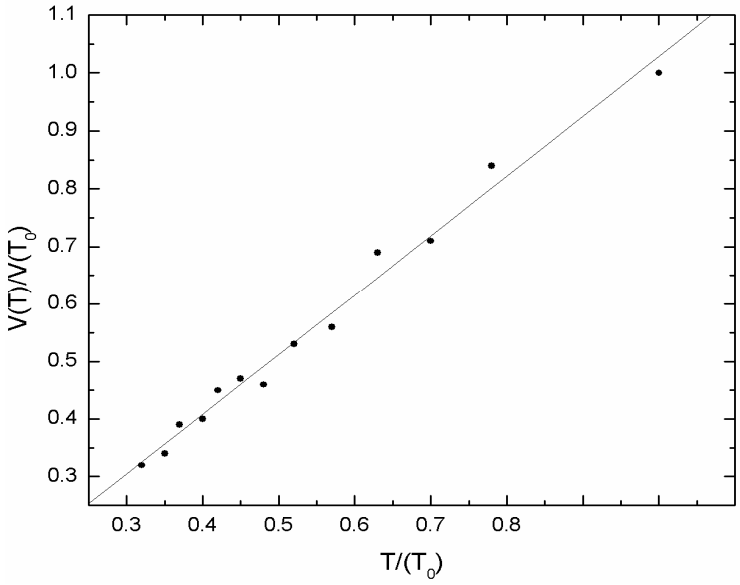

Figure 11.6: A plot of $V(T)/V(T_0)$ for one of the peaks of the W29 centre. The spectra for W29 centre arise from transitions on the ground state.

11.6.4 Linewidths and spin-lattice relaxation time for the R4/W6 centre.

The linewidth for the R4/W6 centre varied from a high of 14 G at room temperature to just under 2 G at about 50 K as shown in Figure 11.7. In the figure, the solid curve represents a nonlinear fit using *Origin 6.0* to the data using Equation 11.16. The fitting yielded values: ΔH_{0L} =1.38 ± 0.61 (G); B=41.63 ± 5.50 (G); E_a =27.3 ± 3.5 meV.

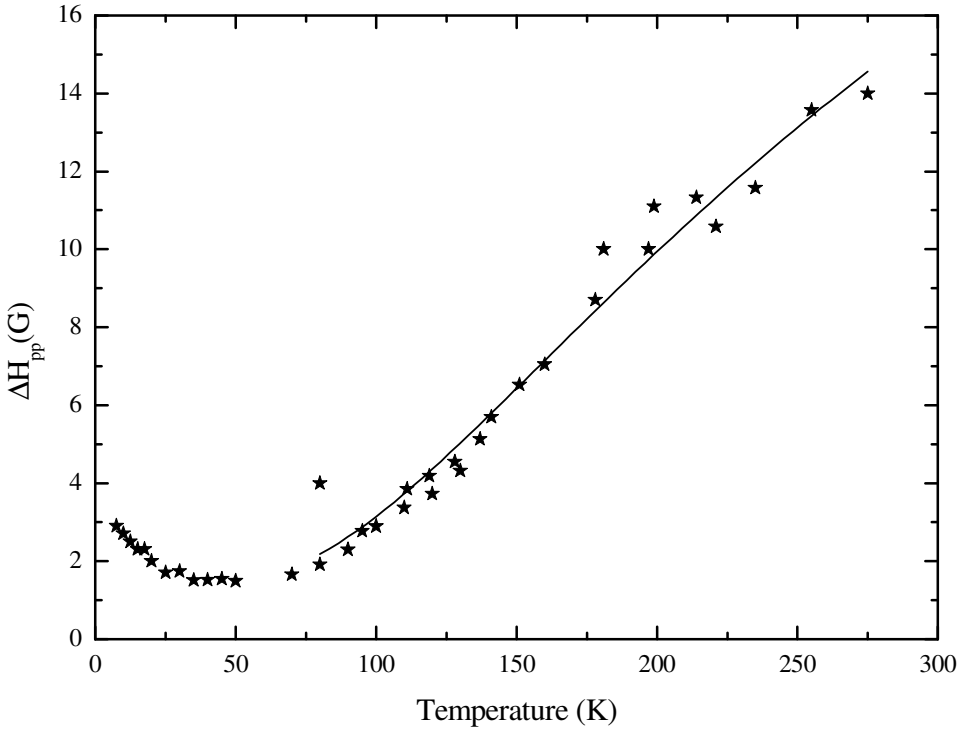

Figure 11.7: Linewidth ΔH_{pp}(G) versus T(K) for R4/W6. The dots represent the experimental data whereas the solid curve represents a fit to experimental linewidths for R4/W6 using Equation 11.16

The experimental data presented in Figure 11.8 in the low temperature region was fitted using *Origin 6.0* to an inverse relation as given in Equation 11.17. The values for fitting parameters were: ΔH_{0L}=(1.29 ± 0.07) ×10^{-4} (T); B=(7.70 ± 1.05) ×10^{-4} (T. K).

The natural or "residual" linewidth was found to be 1.29±0.07 G. This compares favourably with 1.38 ± 0.6 G which is a corresponding value for the higher temperature data as obtained from Figure 11.7.

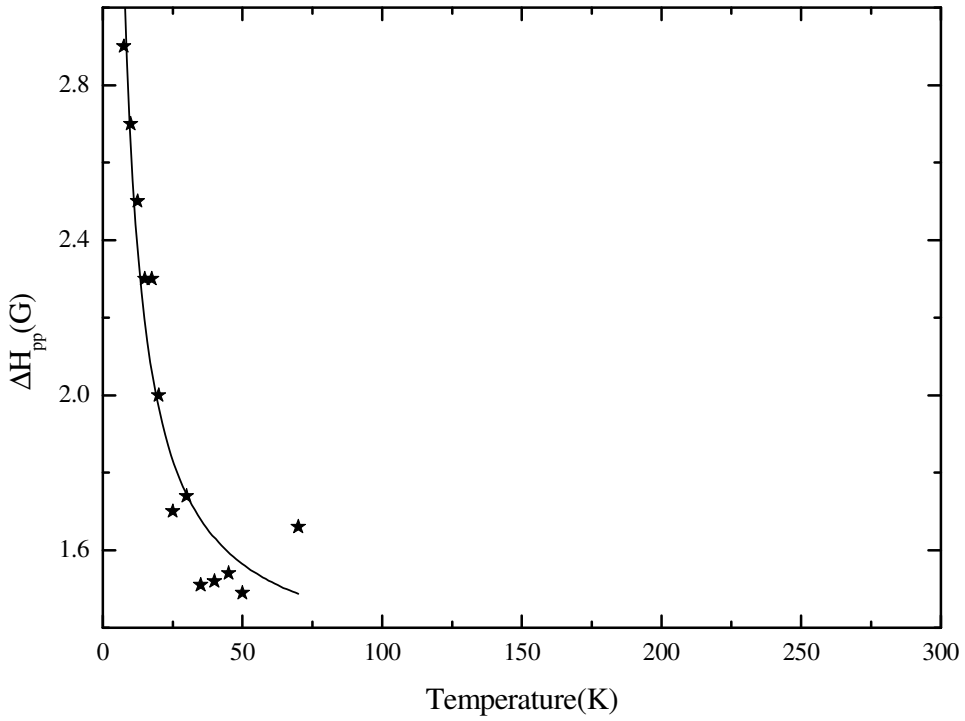

Figure 11.8: Linewidth ΔH_{pp} (G) versus T(K) for R4/W6 in the low temperature region. The dots represent the experimental data whereas the solid curve represents a fit to the experimental linewidths for R4/W6 using Equation 11.17.

11.6.5 Spin relaxation times T_1 versus temperature for R4/W6

Values for T_1 in the temperature range 6 to 300 K were obtained using the methods described for W29 already discussed. A plot of $\frac{1}{T_1}$ the relaxation rate against $\frac{1}{T}$ for the R4/W6 centre for the temperature range is shown in Figure 11.9.

The function of Equation 11.18 that is, $\frac{1}{T_1} = A\exp\left(-\frac{E_a}{k_B T}\right)$, gave a good fit using *Origin 6.0* to the T_1 data in the temperature range 50 -300K. The fit is also very good and yielded the following values: $A = 6.21\times10^{8} \pm 7.02\times10^{7}$ Hz ; E_a=25.8 ± 1.9 meV. This strongly suggests that the dominant relaxation mechanism for the R4/W6 is the Orbach process.

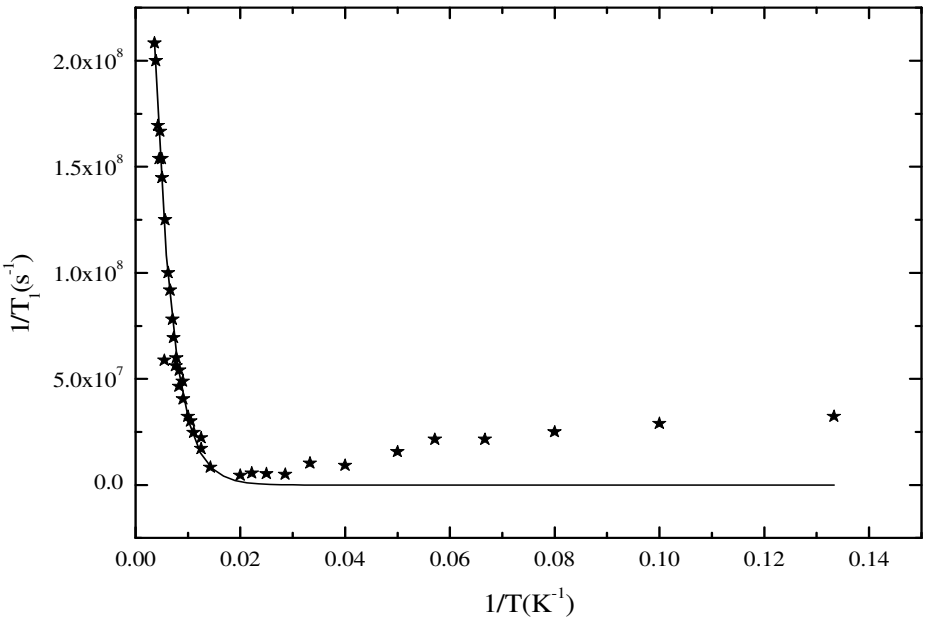

Figure 11.9: A plot of $\frac{1}{T_1}$ versus $\frac{1}{T}$ (K^{-1}) for R4/W6 centre. The stars represent the experimental data while the solid line represents a least- squares fitting to the data. Above 70 K, the Orbach process is dominant.

The activation energy of 25.8±1.9 meV was in excellent agreement with the corresponding value determined from fitting the linewidth data for the same temperature range as given in Figure 11.7. The two energy values are tabulated in Table 11.2.

Table 11.2: Activation energies in (meV) for R4/W6 centre.

E_a (meV)from saturation data	E_a (meV) from linewidth data
25.8±1.9	27.3±3.5

11.7 Discussion

11.7.1 Linewidths

The observation of large linewidth changes for R4/W6 and W29 centres clearly suggests changes in the spin-lattice relaxation times T_1. This large variation is indicative of different

relaxation processes that are dominant over the temperature range involved and which give rise to varying spin-lattice relaxation times T_1.

The fit to Equation 11.18, shows that the temperature dependence of the linewidths in the temperatures higher than the minima in Figures 11.1 and 11.7 suggests a process whose activation energy can be determined. The residual or "natural" width ΔH_0 of the line was thus a shift to the expression. Clearly a reasonably good fit to the data was obtained and suggested the variation obeyed a form of Arrhenius law so that E_a is the activation energy.

In the higher temperature regions used, the linewidths have suggested that the relaxation mechanism for both the W29 and R4/W6 centres was most probably an Orbach relaxation process. The experimental linewidth data as well as the non-linear fitting curves have been given in Figures 11.1 and 11.7 for W29 and R4/W6 respectively. This probably suggests that the linewidths are largely due to lifetime effects so that T_1's are inversely proportional to linewidths. Hence it appears that other line broadening mechanisms such as hyperfine interaction are less significant.

At low temperatures, very few phonons are available for relaxation. The net effect is the observed broadening of the lines at low temperatures and is consistent with direct relaxation process as suggested by the fits to experimental data given in Figures 11.2 and 11.8 or W29 and R4/W6 centres, respectively.

The minima in linewiths near 50 K and 70 K for R4/W6 and W29 respectively, appear to be determined by two competing relaxation processes, one being dominant below and the other above these temperatures. Our results have suggested that the direct process is dominant below the temperature of minimum linewidth whereas the Orbach process becomes more efficient above this temperature for both R4/W6 and the W29 centres.

11.7.2 Spin lattice relaxation times

The direct process as represented by Equation 11.11 leads to a very low relaxation rate and hence the process is not efficient for the R4/W6 and W29 EPR centres.

Similarly, in diamond the relatively high speed of sound leads to very low relaxation rates and the substitution of the various constants in Equations 11.13 and 11.14 (describing the Raman process) give $T_1 \approx 100\,\mathrm{s}$ at 300 K. Our results could be fitted with an exponential rather than a power law and hence we concluded the Raman process was not an efficient relaxation process for the EPR systems in the temperature interval of the investigation.

The temperature variation of the relaxation rate $1/T_1$ for W29 is given in Figure 11.5. This rate agrees very well with the model for the Orbach process as given by Equation 11.15. It is thus suggested that, above 50 K the Orbach process is the dominant relaxation process for the W29 centre with an excited state involved being Δ=15.5 meV above the ground state. The value is given in Table 11.1

The graph of Figure 11.7 also shows a clear evidence of the Orbach process for the R4/W6 centre at temperatures above 70 K. An activation energy corresponding to Δ of 25.8 meV was deduced and is given in Table 11.2. From Figure 11.7, it is seen that cooling from 70 K, the relaxation rate went through a minimum before increasing gradually right down to the lowest temperatures used i.e. 7.5 K.

The result for the R4/W6 is in agreement with the work of Twitchen *et al*. (1999) who suggested the Orbach process as the dominant relaxation process above 50 K and in which an excited state Δ=20 meV was involved.

11.8 Conclusion

Our results have shown that the Orbach process is the dominant relaxation mechanism in the temperature range 70-300 K for the W29 centre and 50-300 K for the R4/W6 centre.

In the low temperature regions i.e. below 50K and 70 K for W29 and R4/W6 respectively, the relaxation mechanism is the direct process.

Spin resonance relaxation times have provided information on the unpaired electron dynamics in the W29 and R4/W6 centres suggesting excited states situated at 15.5 meV and 25.8 meV, respectively, above the ground state.

The activation energy obtained from both the linewidth and saturation measurements were in very good agreement. This shows that the use of saturation data for T_1 measurements is reliable.

CHAPTER TWELVE

CONCLUSIONS

12.1 Summary of results

The major aim of the present work was the determination of the structure of radiation damage centres in type Ib diamond. Towards that goal, EPR has been used to study the centres caused by either electron- or neutron irradiations. Isochronal annealing measurements have been obtained for a number of the EPR centres up to 850 ^{o}C

The centres W15, W29, R4/W6, W33, W37, W46 and W47 are observed following annealing at temperatures starting after about 400 ^{o}C. Of these centres only W33 and W15 are still growing in intensity after annealing at 850 ^{o}C the temperature at which all the others are annealing out. The central region or g=2 region of our spectra consists mainly of the a-line. This is a centre whose complex nature has been understood a bit better based on the annealing curves obtained in this work.

The effective spin of S=3/2 for the W11, W12, W13 and W14 EPR centres have been verified conclusively in this work by employing EPR $\Delta m_s = 2$ transitions. These centres are found only in type Ib diamond and therefore the nitrogen impurity is suggested. However, their annealing curves suggest that the nitrogen may not be directly involved but donates electrons necessary for the formation of the centres. An increase in the S1 or negative vacancy as these centres anneal out suggest an involvement of the vacancy in their formation. The centres are therefore likely to be perturbed vacancies as first suggested by Lowther and van Wyk (1994). This has been supported by the findings of Iakoubvoskii *et al.* (2005) that suggested that the W11 and W13 centres are vacancy-interstitial complexes. However, it is not clear how such V^{-}-I (vacancy-interstitial) models could give rise to the observed symmetries.

A major result of this work has been a study of EPR centres W33, W37, W46 and W47.

The fact that all these centres first became observable after 400 ^{o}C annealing also suggests that they were formed under the beam. They also exhibited similar growth rates. The centres W33, W46 and W47 all have effective spins S=1 while the W37 have S=2. Furthermore, the fact that W37 and W47 anneal out at exactly the same temperature suggests that they are really one and the same entity. The rearrangement of the 4 unpaired electrons in the dangling bonds can lead to S=2 for the W37 and S=1 for the W47.

These centres were first observed together with the W15 centre, the N-V centre. From annealing behaviour and spin Hamiltonian parameters it became clear that they must also involve nitrogen and vacancy just like the W15. The W46 anneals out before the other three centres suggesting that its vacancy was relatively closer to the nitrogen compared to the others as shown in the proposed model of Figure 8.9. All these centres except the W33 have rhombic symmetry which means that both the nitrogen and the vacancy lie in the same (110)-plane.

The W33 has symmetry lower than rhombic and suggests that the nitrogen and vacancy may not be in the same (110) plane. The first derivative EPR spectra for W33 are shown in Figure 8. 6; the spectra suggest a splitting and thus a possible tilting of the principal axis of the centre out of a {110}-plane.

The W29 EPR centre was found to have many similarities with R4/W6, the neutral divacancy centre in diamond. Their symmetries are both close to <111>; they have large D-values and E-terms. In addition their g-tensors are isotropic and very close to free spin value. We have concluded that W29 is a negative divacancy.

The fact that the neutral divacancy centre R4/W6 is observed before 650 ^{o}C when the vacancy becomes mobile is an indication that two vacancies are created next to each other during the irradiation. We first observed the centre after 400 ^{o}C annealing because of the difficulty to do so prior to the annealing out of the R1 and R2 centre as well of the W11-W14 centres. In fact Lea-Wilson (1988) showed that the R4/W6 is observed before annealing in electron irradiated in Ia diamonds. The same explanation is expected to hold for the W29 centre.

The unusually large linewidths of the centres W29 and R4/W6 suggested spin lattice relaxation as the major cause. The spin lattice relaxation times T_1 measurements have been obtained using CW saturation methods. For both centres the dominant relaxation mechanism is direct process at low temperatures (below 50 K for R4/W6 and below 70 for W29 centre). The Orbach process takes over for both centres at elevated temperatures (50-300K for R4/W6 and 70-300K) for W29). The results suggest excited states 15.5 meV and 25.8 meV for W29 and R4/W6, respectively.

The linewidth data were fitted using non-linear curve fitting to Equations 11.6 and 11.7 in the upper and lower temperature regimes respectively. The minima in the experimental linewidths correspond to the intersection of the curves.

The fact that both the linewidth data and the T_1 data based on CW saturation yieldd similar results suggests that the saturation methods provide reliable T_1 measurements.

12.2 Suggested further work

- To do further study of W11-W14 centres using ^{13}C-enriched diamond. This is a strategy that other workers have used to obtain structures for R1 and R2 (Twitchen *et al.* 1999; Hunt *et al.* 2002a, b).

- To use samples in which the W11-W14 centres have comparable concentrations with the S1. In our annealing curves changes on the intensity of the S1 line was observed as the W11-W14 centres as well as the R1 and R2 centres annealed out. It may be feasible to correlate the growth of S1 and the decay of the W11-W14 centres if their concentrations are comparable.

- The a-line annealing behaviour has been studied in this work. Obviously further studies are required to understand this complex centre. This could be done using a number of diamonds with different concentrations of P1. As the damage giving rise to the a-line may be a localized and oriented in the lattice, irradiations in specific crystallographic directions should be useful.

12.3 Publications that have accrued from the present work

We have been able to publish the following while carrying out the research reported in this thesis:

1. ESR studies of the negative divacancy in irradiated type Ib diamonds
   Kirui, J.K., van Wyk, J.A. and Hoch, M.J.R. (1999) *Diamond and Related Materials*, **8**, 1569.

2. EPR data on the self-interstitial complex *O*3 in diamond
   Hunt, D.C., Twitchen, D.J., Newton, M.E., Baker, J.M, Kirui, J.K., van Wyk, J.A., Anthony, T.R., and, Banholzer, W.F (2000b) *Phys. Rev. B*, **62** (10), 6587

3. Vacancy-associated EPR centres in irradiated type Ib diamond
   Kirui, J.K., van Wyk, JA and Hoch, M.J.R
   (accepted for publication in the first issue of the African Physical Review)

REFERENCES

Abragam, A. and Pryce, H.M.L. (1951) *Proc. R. Soc*. (London), **A205**, 135.

Abragam A. and Bleaney, B. (1970) *Electron Paramagnetic Resonance of Transition Ions*, Dover Publications, Inc. New York.

Ammerlaan, C.A.J (1988) University of Amsterdam. (*Landbolt-Börnstein Numerical Data and Functional Relationships in Science and Technology*, **22**

Baldwin, J. A. (1963) *Phys. Rev. Lett.* **10**, 220.

Berman R. 1965, Editor, *The Physical Principles of Diamond*, Oxford University Press.

Bernholc, J. Antonelli, A., Del Sole, T. M., Bar-Yam, Y. and Pantelides, S.T. (1988) *Phys. Rev.Lett.,* **61***,* 2689

Bibby, B.R.and Duncan, I. (1975) *Diamond Conference*, Cambridge, Paper #10.

Biersack, J.P. and Haggmark, L.G. (1980) *Nucl. Instr. and Meth*. **174,** 257.

Bourgoin, J.C. and Massarani, B. (1976) *Phys. Rev. B,* **14**, 3690.

Bourgoin, J.C. and Lannoo, M. (1983) *Point Defects in Semiconductors II, Springer Series Solid State*.

Breuer, S. J. and Briddon, P. R. (1995) *Phys. Rev. B*, **51**, 6984.

Budylin, B.V. and Vorobev, A.A., (1964) *Effect of Radiation on Ionic Structures*, Publishers: Israeli Program for Scientific Translation.

Burns, R.C., Hansen, J.O., Spits, R.A., Sibanda, M., Welbourn, C.M. and Wech, D.L. (1999) *Diamond and Relat. Mater*. **8**, 1433.

Burns, R.C. and Davies, G.J. (1992), in: *The properties of natural and synthetic diamond*, (Ed. J. E. Field), Academic Press.

Burns, R.C., Cvetkovic, V., Dodge, C.N., Evans, D.J.F., Rooney, M-L.T., Spear, P.M. and Welbourn, C.M. (1990) *Journal of Crystal Growth,* **104**, 257.

Campbell, B., Choudhury, W., Mainwood, A., Newton, M. E., Davies, G. (2002) *Nucl. Instr. and Meth* , **A 476**, 680.

Castner Jr, T.G. (1959) *Phys. Rev.*, 115, 1506.

Clark, C.D., Ditchburn, R.W and Dyer, H.B. 1955, Proc. R. Soc. (London) Series A, 234, 363.

Clark, C.D, Ditchburn, R.W. and Dyer, H.B. (1956) *Proc. R. Soc. London*, Ser. A, **237**, 75.

Clark, C.D., Kemmey, P.D.and Mitchell, E.W. (1961) *Discuss. Faraday Soc.,* **31**, 96.

Clark, C.D., Duncan, I., Lomer, J.N. and Whippey, P.W. (1964) *Brit. Ceramic Soc*., **1**, 85.

Collins, A.T. and. Dahwich, A. (2004) *Diamond and Relat. Mater*. **13**, 1959.

Custers, J.H.F. (1955) *Nature*, **176**, 173.

Davies, G. (1974) *Proc. R. Soc*. (London), **A336**, 507.

Davies, G. and Hamer, M.F. (1976) *Proc. R. Soc. (London*), **A348**, 285.

Davies, G., Nazare, M. H and. Hamer, M.F. (1976) *Proc.R. Soc. (London)*, **A351**, 245

Davies,G. (1977) *Nature,* **269**, 498.

Davies, G. (1981) *J. Phys.C*, **14**, L391.

Davies, G., Lawson, S.C., Collins, A.T., Mainwood, A. and Sharp, S.J. (1992) *Phys. Rev. B,* **46**, 13157.

Davies G. (1994) (Ed) *Properties and Growth of Diamond*, INSPEC: Institute of Electrical Engineers, London

Davies, G., Cambell, B., Mainwood, A., Newton, M.E., Watkis, M, Kanda, H., and Anthony, T.R. (2001), *Phys. stat. sol.(a)*, **186**, 187.

Denning, R.M. and Poindtexter, E.H. (1964) *The American Mineralogist*, **49**, 277.

Dienes, G.J. and Vineyard, G.H. (1957) *Radiation effects in solids*, Interscience Publishers, New York, London.

du Preez, L. (1965) *Ph.D. Thesis*, University of Witwatersrand, Johannesburg.

Dyer HB and du Preez L (1965) *J. Chem. Phys*. 42, 1898.

Farrer. R.G, (1969) *Solid State Comm*. **7**, 685

Faulkner, E.A. and Lomer, J.N. (1962) *Phil. Mag. B*, **7**, 1995.

Field, J.E. 1994, *Properties and Growth of Diamond* (Ed. by G. Davies), INSPEC.

Finn, C.B.P., Orbach, R. and Wolfe , W.P. (1961) *Proc. Phys. Soc. (London), 77*, 261.

Fisher, S.B. and Banbury, P.C. (1970) *Proc. Int. Conf. Atomic Collision Phenomena in Solids*. Brighton, 1969, 232.

Fletcher, R.C.and Brown, W.L. (1953) *Phys. Rev*., **92**, 584.

Geshwind, S., Devlin, G.E., Cohen, R.L. and Chinn, S.R. (1965) *Phys. Rev*., **137**, A1087.

Glendenin, L.E. 1948, *Nucleonics*, **2**, 12.

Gordy, W. (1980) *The Theory and Applications of Electron Spin Resonance*, John Wiley and Sons, New York.

Goss, J. P., Jones, R., Briddon, P. R., Davies, G., Collins, A. T., Mainwood, A., van Wyk, J. A., Baker, J.M., Newton, M. E., Stoneham, A. M. and Lawson, S. C. (1997) *Phys. Rev. B*, **56**, 16031

Goss, J. P., Briddon, P. R., Papagiannidis, S., and Jones, R.(2004) *Phys. Rev*. *B* **70**, 235208.

Goss, J. P., Rayson, M.J., Briddon, P. R. and Baker, J.M.(2007) *Phys. Rev. B* , **76**, 45208.

Hanson, R., Mendoza, F.M., Epstein, R.J. and Awschalom, D.D (2006) *Phys Rev. Lett*., 97, 087601.

He, X-F., Manson, N.B., Fisk, T.H. (1993) *Phys. Rev. B*, **47**, 8809.

Humble, P. (1982) *Proc. R. Soc. A*, **381**, 65

Hunt, D. C., Twitchen, D.J., Newton, M.E., Baker, J.M., Anthony, T.R., Banholzer, W.F.and Vagarali, S.S. (2000a) *Phys. Rev. B*, **61**, 3863.

Hunt, D.C., Twitchen, D.J., Newton, M.E., Baker, J.M, Kirui, J.K., van Wyk, J.A., Anthony, T.R., and, Banholzer, W.F (2000b) *Phys. Rev. B*, **62** (10), 6587

I.A.E.A. (1966), *Directory of Nuclear Reactors VI: Research, Test and Experimental Reactors.*, Vienna.

Iakoubovskii, K., Kiflawi, I., Johnston, K., Collins, A., Davies, G., and Stessmans, A. (2003) *Physica B*, **340-342**, 67.

Iakoubovskii, K., Dannefaer, S. and Stessmans, A. (2005) *Phys. Rev. B*, **71**, 233201.

Isoya, J., Kanda, H., Uchida, Y., Lawson, S.C., Yamasaki, S., Itoh, H. and Morita, Y. (1992) *Phys. Rev. B*, **45**, 1436.

Iwata, T. and Nihira,T. (1971) *J. Phys. Soc. Japan*, **31**, 761.

Kanda, H., Ohsawa, T., Fukunaga, O. and Sunagawa, I. (1989) *J. Cryst. Growth*, **94**, 115.

Keating, D.T. 1963, *Bull. Am. Phys. Soc*. **5**, 146.

Kelly, B.T. 1966, *Irradiation Damage to Solids*, Pergamon Press.

Kiflawi, I., Mayer, A.E., Spear, P.M., van Wyk, J.A. and Woods, G.S. (1994) *Phil. Mag. B*, **69**, 1141.

Kiflawi, I., Mainwood, A., Kanda, H. and Fisher, D. (1996) *Phys. Rev. B.*, **54**, 16719.

Kim, Y.M. and Watkins, G.D. (1971) *J. Appl. Phys*., **42**, 722.

Kim,Y.M., Lee, Y.H., Brosius, P. and Corbett, J.W. (1972) *ESR studies in neutron-irradiated diamond. Inst. Phys. Conf. Ser.* **16**, 202.

Kinchin, G.W. and Pease, R.S. (1955) *Repts. Prog. Phys*. **18**, 1

Kirui, J.K., van Wyk, J.A. and Hoch, M.J.R. (1999) *Diamond and Related Materials*, **8**, 1569.

Kittel, C. and Abrahams, E. (1953) *Rev. Mod. Phys*. **25**, 233

Larson, G. H. and Jeffries, C. D. (1966) *Phys. Rev*. **141**, 461

Lawson, S.C., Fisher, D, Hunt, D.C. and Newton, M.E. (1998) *J. Phys.: Condens. Matter*, **10**, 6171.

Lea-Wilson, M.A. (1988), *Ph.D. Thesis*, University of Reading, chap5.

Lea-Wilson, M.A., Lomer, J.N. and van Wyk, J.A. (1995) *Phil. Mag. B*, **72**, 81.

Loubser, J.H.N. and van Wyk, J.A. (1977) *Diamond Research,* p11.

Loubser, J.H.N. and. van Wyk, J.A (1978*) Rept. Prog. Phys*. **41**, 1201.

Loubser, J.H.N.and van Wyk, J.A. (1981) *Diamond Conference*, Reading.

Lowther, J.E. and van Wyk, J.A. (1994) *Phys. Rev. B,* **49** (16), 11010.

Mainwood, A., Lowther, J.E and van Wyk, J.A. (1993) *J. Phys.: Conden. Matter*, **5**, 7929.

Manson, N.B., Harrison, J.P. and Sellars, M.J. (2006), *Phys Rev B*, **74**, 104303.

McKinley, W.A., Jr. and Feshbach**,** H. (1948), *Phys. Rev.* **74**, 1759

Meyerhof, W. E., 1967, *Elements of Nuclear Physics*, McGraw-Hill Book Company, p. 74.

Mita , Y. (1996) *Phys. Rev. B,* **53**, 11360.

Morton, J.R. (1964), *Chem. Rev.*, **64**, 453

Mott, N.F. and Gurney, R.W. 1940, *Electronic Processes in Ionic Crystals*, Oxford University Press, London.

Motte F. and Debrue, J. 1963, In "*The Interactions of Radiation with Solids*",: Eds:

Strumane R, Nihoul J, Gevers R, and Amelinckx S)

Newton, M.E., Campbell, B.A., Twitchen, D.J., Baker, J.M., and Anthony, T.R. (2002) *Diamond and Rel. Mat*., **11**, 618.

Orbach R., (1961) *Proc. R. Soc. London, Ser. A*, **264**, 458.

Orton, J.W. (1968) *Electron Paramagnetic Resonance: An Introduction to Transition Group Ions in Crystals*, London Illife Books Ltd.

Pake G.E. (1962) *Paramagnetic Resonace, An Introductory Monogram*, Benjamin, New York

Pake G.E. and Estle, T.L. (1973) *The Physical Principles of Electron Paramagnetic Resonance*, 2nd Ed. W.A. Benjamin, Inc.(Chap.4, 5).

Poole, C.P. (1983) *Electron Spin Resonance: A comprehensive Treatise on Experimental Techniques*, John Wiley and Sons. Chapters 3-7.

Prins, J.F., Derry, T.E.and Sellschop, J.P.F. (1986), *Phys. Rev. B,* **34**, 8870.

Pryce, H.M.L. (1950) *Proc. Phys. Soc.,* (London) **A63**, 25.

Reddy, N.R.S, Manson, N.B, and Krausz, E.R, (1987) *J. Lum*., **28**, 46.

Redman, D.A, Brown, S., Sands, R.H. and Rand, S.C. (1991) *Phys. Rev. Lett.*, **67**, 3420.

Reynhardt, E.C., High, G.L. and van Wyk, J.A (1998) *J. Chem. Phys.*, 109, 8471.

Seitz, F. and Koehler, J. S. 1956, *Solid State Physics ed. Seitz and Turnbull*, vol. **2**, 307.

Smith, W.V., Sorokin, P.P., Gelles, I. L.and Lasher G.J. (1959) *Phys. Rev*., **115**, 1546.

SNS Website 2004, http://www.SNS.gov.

Stevens, K.W.H. (1963) In *Magnetism* (Ed. G. Radoh and H. Suhl) Vol.I. Academic Press, New York.

Stoneham, A.M. (1975) *The Theory of Defects in Solids*, Clarendon Press, Oxford.

Townsend, P.D. and Kelly, J.C. (1973) *Colour Centres and Imperfections in Insulators and Semiconductors*, Sussex University Press, Brighton.

Tucker, O.D. (1995) *Ph. D. Thesis, University of Oxford*, page 43.

Twitchen, D.J., Newton, M.E.,Baker, J.M., Tucker, O.D, Anthony, T.R. and Banholzer, W.F. (1996) *Phys. Rev. B*, , **54**, 6988.

Twitchen, D.J. (1997) *Ph.D. Thesis, Oxford University*, p. 182.

Twitchen, D. J., Newton, M.E., Baker, J.M., Anthony, T.R. and Banholzer, W.F. (1999) *Phys. Rev. B*, **59**, 12900.

Twitchen, D. J., Newton, M.E., Baker, J.M., Anthony, T.R. and Banholzer, W.F. (2001) *J. Phys. : Condens. Matter*, **13**, 2045.

van Oort, E., Manson, N. B and Glasbeek, M. (1988) *J. Phys. C* , **21**, 4385.

van Oort, E., Stroomer, P. and Glasbeek, M. (1990) *Phys. Rev. B,* **42**, 8605.

van Wyk, J.A. (1994) *J. Phys : Condens. Matter*, **6**, 801

van Wyk, J. A. and Woods, G. S. (1995) *J. Phys.: Condens. Matter* **7**, 5901.

van Wyk, J.A., Tucker, O.D., Newton, M.E., Baker, J.M., Woods, G.S. and Spear, P. (1995) *Phys. Rev. B,* **52**, 12657.

van Wyk, J.A., Reynhardt, E.C, High, G.L and Kiflawi, I (1997) *J. Phys. D: Appl. Phys.*, **30**, 1790.

van Wyk, J. A. (1999) Private communication.

Walker, J. (1977) *J. Phys. C.*, **10**, 3867.

Walt, M. and Barschall, H.H. (1954), *Phys. Rev.*, **93**, 1062.

Watkins, G.D. (1975), *Point Defects in Solids* Vol. **2**, (Ed. J H Crawford and L M Slifkin, p. 333 (New York: Plenum)

Watt, G.A., Newton, M.E. and Baker, J.M. (2001) *Diamond and Relat. Mater.* **10**, 1681

Watterson, J.I.W. (1975). *Ph. D. Thesis*, University of the Witwatersrand, pp. 42

Wentorf, R.H. (1965), *J. Phys. Chem.*, **69**, 3063.

Weltner, W. (1983). *Magnetic Atoms and Molecules*, Dover Publications, Inc., New York.

Wert, C. (1950), *Phys. Rev.*, 7**9**, 601.

Weil, J.A., Bolton, J.R. and Wertz, J.E (1994) *Electron Spin Resonance: Elementary Theory and Practical Applications,* John Wiley and Sons.

Woods, G. S., van Wyk, J. A., and Collins, A. T. (1990): *Phil. Mag. B*, **62**, 589

Wu, W. and Fahy, S. (1994) *Phys. Rev. B,* **49**, 3030.